#### **SANDIA REPORT**

SAND2016-9117 Unlimited Release Printed September 2016

# Fundamental Study of Disposition and Release of Methane in a Shale Gas Reservoir

Yifeng Wang, Yongliang Xiong, Louise J. Criscenti, Tuan Ahn Ho, Philippe F. Weck, Anastasia G. Ilgen, Edward Matteo, Jessica N. Kruichak, Melissa M. Mills, Thomas Dewers, Margaret E. Gordon and Yucel Akkutlu

repared by Sandia National Laboratories Albuquerque, New Mexico 87185 and Livermore, California 94550

Sandia National Laboratories is a multi-mission laboratory managed and operated by Sandia Corporation, a wholly owned subsidiary of Lockheed Martin Corporation, for the U.S. Department of Energy's National Nuclear Security Administration under contract DE-AC04-94AL85000.

Approved for public release; further dissemination unlimited.



Issued by Sandia National Laboratories, operated for the United States Department of Energy by Sandia Corporation.

**NOTICE:** This report was prepared as an account of work sponsored by an agency of the United States Government. Neither the United States Government, nor any agency thereof, nor any of their employees, nor any of their contractors, subcontractors, or their employees, make any warranty, express or implied, or assume any legal liability or responsibility for the accuracy, completeness, or usefulness of any information, apparatus, product, or process disclosed, or represent that its use would not infringe privately owned rights. Reference herein to any specific commercial product, process, or service by trade name, trademark, manufacturer, or otherwise, does not necessarily constitute or imply its endorsement, recommendation, or favoring by the United States Government, any agency thereof, or any of their contractors or subcontractors. The views and opinions expressed herein do not necessarily state or reflect those of the United States Government, any agency thereof, or any of their contractors.

Printed in the United States of America. This report has been reproduced directly from the best available copy.

Available to DOE and DOE contractors from

U.S. Department of Energy Office of Scientific and Technical Information P.O. Box 62 Oak Ridge, TN 37831

Telephone: (865) 576-8401 Facsimile: (865) 576-5728 E-Mail: reports@osti.gov

Online ordering: <a href="http://www.osti.gov/scitech">http://www.osti.gov/scitech</a>

#### Available to the public from

U.S. Department of Commerce National Technical Information Service 5301 Shawnee Rd Alexandria, VA 22312

Telephone: (800) 553-6847 Facsimile: (703) 605-6900 E-Mail: orders@ntis.gov

Online order: http://www.ntis.gov/search



#### SAND2016-9117 Unlimited Release Printed September 2016

## Fundamental Study of Disposition and Release of Methane in a Shale Gas Reservoir

Yifeng Wang Department of Nuclear Waste Disposal Research and Analysis

P. O. Box 5800, MS 0779

Yongliang Xiong

Department of Repository Performance

P. O. Box 5800, MS 1395

Louise J. Criscenti, Tuan Ahn Ho

Department of Geochemistry

P. O. Box 5800, MS 0754

Philippe F. Weck

Storage and Transportation Technology

P. O. Box 5800, MS 0747

Anastasia G. Ilgen

Department of Geochemistry

P. O. Box 5800, MS 0754

Edward Matteo, Jessica N. Kruichak, Melissa M. Mills Department of Nuclear Waste Disposal Research and Analysis

P. O. Box 5800, MS 0779

Thomas Dewers

Department of Geomechanics

P. O. Box 5800, MS 0751

Margaret E. Gordon

Department of Materials, Devices and Energy Technologies

P. O. Box 5800, MS 0734

Sandia National Laboratories

Yucel Akkutlu Department of Petroleum Engineering Texas A&M University

#### Abstract

The recent boom in shale gas production through hydrofracturing has reshaped the energy production landscape in the United States. Wellbore production rates vary greatly among the wells within a single field and decline rapidly with time, thus bring up a serious concern with the sustainability of shale gas

production. Shale gas production starts with creating a fracture network by injecting a pressurized fluid in a wellbore. The induced fractures are then held open by proppant particles. During production, gas releases from the mudstone matrix, migrates to nearby fractures, and ultimately reaches a production wellbore. Given the relatively high permeability of the induced fractures, gas release and migration in low-permeability shale matrix is likely to be a limiting step for long-term wellbore production. Therefore, a clear understanding of the underlying mechanisms of methane disposition and release in shale matrix is crucial for the development of new technologies to maximize gas production and recovery. Shale is a natural nanocomposite material with distinct characteristics of nanometer-scale pore sizes, extremely low permeability, high clay contents, significant amounts of organic carbon, and large spatial heterogeneities. Our work has shown that nanopore confinement plays an important role in methane disposition and release in shale matrix. Using molecular simulations, we show that methane release in nanoporous kerogen matrix is characterized by fast release of pressurized free gas (accounting for ~ 30 - 47% recovery) followed by slow release of adsorbed gas as the gas pressure decreases. The first stage is driven by the gas pressure gradient while the second stage is controlled by gas desorption and diffusion. The long-term production decline appears controlled by the second stage of gas release. We further show that diffusion of all methane in nanoporous kerogen behaves differently from the bulk phase, with much smaller diffusion coefficients. The MD simulations also indicate that a significant fraction (3 - 35%) of methane deposited in kerogen can potentially become trapped in isolated nanopores and thus not recoverable. We have successfully established experimental capabilities for measuring gas sorption and desorption on shale and model materials under a wide range of physical and chemical conditions. Both low and high pressure measurements show significant sorption of CH<sub>4</sub> and CO<sub>2</sub> onto clays, implying that methane adsorbed on clay minerals could contribute a significant portion of gas-in-place in an unconventional reservoir. We have also studied the potential impact of the interaction of shale with hydrofracking fluid on gas sorption. We have found that the CH<sub>4</sub>-CO<sub>2</sub> sorption capacity for the reacted sample is systematically lower (by a factor of  $\sim$ 2) than that for the unreacted (raw) sample. This difference in sorption capacity may result from a mineralogical or surface chemistry change of the shale sample induced by fluid-rock interaction. Our results shed a new light on mechanistic understanding gas release and production decline in unconventional reservoirs.

#### **CONTENTS**

| Abstra       | act  | 3          |
|--------------|--|------------|
| Conte        | ents   | 5          |
| Figure       | es   | 6          |
| Table        | S  | 10         |
| Nome         | enclature  | 11         |
| 1 1          | INTRODUCTION   | 43         |
|              |  |            |
| 1.1.<br>1.2. |  |            |
|              |  |            |
| 2.           | GEOCHEMISTRY OF NANOPORES  | 15         |
| 2.1.         | · · · · · · · · · · · · · · · · · · ·                            |            |
| 2.2.         | 1  |            |
| 2.3.         | J 1  |            |
| 2.4.         | · · · · · · · · · · · · · · · · · · ·                            |            |
| 2.5.         | 1 1  |            |
| 2.6.         | r  |            |
| 2.4.         | . References   | 31         |
| 3.           | NANOSTRUCTURAL CONTROL OF METHANE RELEASE IN KEROGEN             | 36         |
| 3.1.         | . Introduction   | 36         |
| 3.2.         |  |            |
| 3.3.         | . Results  | 38         |
| 3.4.         | . Discussion   | 45         |
| 3.5.         | . References   | 45         |
| 4. ]         | EFFECTS OF SURFACE HETEROGENEITIES ON NATURAL GAS STORAGE        | 49         |
| 4.1.         |  |            |
| 4.2.         |  |            |
| 4.3          |  |            |
| 4.4.         |  |            |
| 4.5.         |  |            |
| <i>~</i> 1   |  |            |
|              | EXPERIMENTAL DETERMINATION OF P-V-T-X PROPERTIES AND ADSORPTION  | <b>C</b> 4 |
|              | CTICS IN THE CO2-CH4 SYSTEM UNDER SHALE GAS RESERVOIR CONDITIONS |            |
| 5.1.         |  |            |
| 5.2          |  |            |
| 5.3<br>5.4.  | = <del></del>  |            |
| 5.4.<br>5.4. |  |            |
| 3.4.         | , References   | /0         |
| 6            | SUMMARY  | 71         |

#### **FIGURES**

| Figure 1-1. Wellbore production decline curves for Northern DeWitt County (Eagle Ford)                      |
|---|
| (Robertson, 2013)   |
| Figure 1-2. Integrated experimental and modeling approach to addressing gas disposition and                 |
| release in shale. SANS: small angle neutron scattering; BET: Brunauer-Emmett-Teller;                        |
| TEM: transmission electron microscope; SEM: scanning electron microscope; XRD: X-ray                        |
| diffraction; XRF: X-ray fluorescence  |
| Figure 2-1. Shift of critical temperature of fluid as a function of pore size. The solid line is            |
| calculated from Equation (4). $T_c$ is the critical temperature of the bulk fluid; $T_{cp}$ is the          |
| critical temperature of the fluid in a pore with a radius $r_p$ ; and $\sigma$ is the size parameter of the |
| Lennard-Jones potential. Modified from Zarragoicoechea and Kuz (2004)16                                     |
| Figure 2-2. Average coordination number of Na <sup>+</sup> ions confined in a grapheme slit as a function   |
| of silt width and surface charge density. Data are from Kalluri et al. (2011). Dielectric                   |
| constant of water decreases with reducing slit width and increasing surface charge density.                 |
| 17  |
| Figure 2-3. Effects of nanopore confinement on pore surface chemistry and surface sorption of               |
| alumina materials. Kd is the sorption coefficient normalized to surface area. Nanopore                      |
| confinement makes the pore surface either more negatively or more positively charged,                       |
| leading to the enhancement of surface sorption for both cations and anions. The surface                     |
| areas of the materials were measured with a N2 BET method using a Micrometritics Gemini                     |
| 2360 surface analyzer. Upper panel: dash lines - nonporous alumina, solid lines -                           |
| nanoporous alumina. Modified from Wang et al. (2003b, 2011)19   |
| Figure 2-4. Surface acidity distributions of TiO <sub>2</sub> nanotubes and nanorods (upper panel) and      |
| preferential precipitation of Mo clusters inside nanotubes (lower panel). $pK_a$ is a surface               |
| acidity constant calculated from the single-pK model (Contescu et al., 1993). $f(pK_a)$ is the              |
| distribution of acidity constant. Modified from Wang et al. (2008, 2011)20                                  |
| Figure 2-5. Volume fractions of unfrozen water in clay, silt and sand in permafrost regions. Data           |
| from Osterkamp and Bum (2002).  |

| Figure 2-6. Correction factor for Darcy flow of methane as a function of Knudsen number. $q$ is            |
|--|
| the flux. $q_{Darcy}$ is the flux predicted by Darcy's law. Data from Ziarani and Aguilera (2012).         |
|  |
| Figure 2-7. Relative permeability of cation, anion and neutral species in a 3 μm long and 50 nm            |
| high slit as a function of background electrolyte (KCl) concentration. Relative permeability               |
| is the measured permeability normalized to the value determined at [KCl] = 1.0 M. Data are                 |
| from Plecis et al. (2005)  |
| Figure 2-8. Pore size distribution, methane solubility, and possible methane flow behavior in              |
| shale. $f(r)$ is the pore size distribution in terms of the number of pores. q is the flux. $q_{Darcy}$ is |
| the flux predicted by Darcy's law. P is the gas pressure. Data from Clarkson et al. (2013),                |
| Diaz-Campos et al. (2009), and Fathi et al. (2012)   |
| Figure 3-1. Post-mature kerogen molecule used in our simulations (A). Red, blue, yellow, grey,             |
| and white spheres represent oxygen, nitrogen, sulfur, carbon, and hydrogen atoms,                          |
| respectively. A representative condensed kerogen sample at ambient conditions obtained by                  |
| conducting a series of MD simulations as described in the Methods section (B). Pore size                   |
| distributions of two extreme kerogen samples collected in MD simulations: 1 (red) and 2                    |
| (back) (C)   |
| Figure 3-2. Total uptake (circles) and excess adsorption (triangles) of methane on kerogen                 |
| samples 1 (black) and 2 (white) at 338K as a function of pressure (A). Comparison of the                   |
| excess adsorption for sample 1 (black circles) and 2 (white circles) with experimental results             |
| for activated carbon (purple circles), Haynesville shale (green circles), Barnett shale (red               |
| circles by Gasparik et al. (2014), and orange circles by Zhang et al. (2012), and Green                    |
| Griver kerogen (blue circles) (B). Green River kerogen is type I low thermal maturity                      |
| kerogen. The excess adsorption data for the Barnett and Haynesville shales are measured for                |
| the whole shale (i.e., including organic and inorganic matter) and normalized by the total                 |
| organic carbon. The comparison suggests that excess adsorption calculated for isolated                     |
| kerogen can provide approximate values for methane adsorption in organic-rich shales40                     |
| Figure 3-3. Snapshot demonstrates the method used to extract methane molecules (green                      |
| spheres) from kerogen sample 1 (A). When methane molecule moves into a defined region                      |
| (purple sphere) we extract it from the system by deleting that molecule. Extraction rate                   |
| (black circles-left y axis) and pressure (red circles-right y axis) are plotted as a function of           |
|  |

| time during the extraction for sample 1 (B). Extraction rate calculated for 9 kerogen samples                  |
|--|
| (C). Averaged extraction rate calculated from those obtained for 9 samples (black circles-                     |
| left y axis) and fitted curve calculated using decline curve analysis (black triangles-left y                  |
| axis) with b=0.7022 (D). Constant b obtained when fitting equation (3-1) with simulation                       |
| data at different times (red squares-right y axis) (D)   |
| Figure 3-4. Self-diffusion coefficient D of bulk methane as a function of pressure (A). Self-                  |
| diffusion coefficient of bulk methane was studied by conducting MD simulations for 300                         |
| methane molecules using NPT ensemble at the temperature of 300K (black circles) and                            |
| 338K (white circles). The pressure ranges from 2 to 300 atm. The results at 300K are                           |
| compared with experimental data (red and green circles). Self-diffusion coefficient of all                     |
| methane (i.e., including free gas and adsorbed gas) inside kerogen sample 1 as a function of                   |
| pressure during the extraction (B). This result was obtained by running MD simulations                         |
| using NVT ensemble (338K) starting from the configurations at different pressures obtained                     |
| during the extraction process as described in Figure 3A. All simulations were conducted for                    |
| 40 ns. The last 30 ns trajectory was divided into 3 blocks of 10 ns each to calculate diffusion                |
| coefficient and error. Comparing with that of bulk methane, diffusion coefficient of all                       |
| methane inside kerogen is much smaller (up to 3 orders of magnitude smaller), and                              |
| furthermore it does not change significantly as a function of pressure   |
| Figure 3-5. Profile of number of methane as a function of distance from kerogen atoms at                       |
| different pressure (A). Number of methane associated with specific kerogen atom at 160 atm                     |
| (black) and 2.1 atm (grey) (B). These data were calculated for sample 144                                      |
| Figure 4-1. Organic surface models including pristine graphene and the graphene with                           |
| heterogeneities. (a) pristine graphene, (b) Stone-Wales defect as two pentagons and two                        |
| heptagons), (c) di-vacancy and (d) N-doping. These models are used in quantum mechanical                       |
| simulations to calculate fluid-wall interaction parameters $\epsilon$ and $\sigma$ , which are needed later on |
| as input parameters during the Monte Carlo calculations in predicting the methane storage in                   |
| model pores. Atom colors: carbon (brown), hydrogen (yellow), and nitrogen (blue)50                             |
| Figure 4-2. Isothermal density profile of methane sandwiched in between two graphite walls with                |
| a separation distance of 4nm at 580 psi. The estimated density is based on GCMC                                |
| calculations. The first column is the adsorbed layer, the light gray columns are the excess                    |

| amount of methane due to wall interactions and the last column on the right is the bulk fluid                    |
|--|
| that represents the free gas. Red line is the methane bulk density predicted using NIST52                        |
| Figure 4-3. Chemical potential dependence of methane with varying fluid pressure5.                               |
| The effect of nanopore confinement on the adsorption   |
| Figure 4-4. Langmuir adsorption isotherms for methane in a slit-shape pore with sizes 2, 4 and                   |
| 5nm. The pore walls are made of pristine graphene, i.e., no surface heterogeneities5                             |
| Figure 4-5. Excess amount of methane in slit-shape nanopores with varying sizes5.                                |
| Figure 4-6. Density profile of methane across a 4nm slit pore with pristine walls at 353K. Th                    |
| pore pressure is varied at 580 psi, 2,000psi, 4000 psi, 6000 psi, 8000 psi, and 12,000 psi                       |
| The density of methane is not constant in the pore and has a distinct profile. Its value is                      |
| higher near the wall (first layer) and drops to the free fluid density at the center of the pore                 |
| The red line is the bulk fluid density value as obtained from NIST (2011). Clearly, the                          |
| calculated density in the middle of the pore matches the free gas values50                                       |
| Figure 4-7. Lenard-Jones potential energy for the interaction between methane and varying wal                    |
| properties graphene, N-doped, di-vacancy and Stone-Wales   |
| Figure 4-8. Adsorption isotherms for methane in 4nm graphene pore with heterogeneities on the                    |
| surface5   |
| Figure 4-9. Excess adsorption of methane in slit-pore with surface heterogeneities. The excess                   |
| amount calculations exclude the first layer of adsorption by the walls.  |
| Figure 4-10. Calculated adsorption energies for methane-graphene wall interactions with                          |
| changing number of nitrogen atoms on the surface.  |
| Figure 5-1. High-temperature-high pressure system for measuring gas sorption-desorption under                    |
| reservoir-relevant conditions. 62  |
| Figure 5-2. Calibration of the digital transducers for the measurement of sorption capacities and                |
| kinetics under high-temperature and high pressure conditions. (A) Reference cell; (B                             |
| sample cell6   |
| Figure 5-1. Kerogen isolated from Mancos shale   |
| Figure 5-2. Small angle neutron scattering analysis of Mancos shale  |
| Figure 5-3. FTIR spectra of kerogens isolated from Mancos, Woodford and Marcellus shales60                       |
| Figure 5-4. TGA measurement of CH <sub>4</sub> -CO <sub>2</sub> sorption on activated carbon at 25°C temperature |
| and 1 bar.   |

| Figure 5-4. Determination of sorption kinetics with CH <sub>4</sub> -CO <sub>2</sub> for montmorillonite at 25°C  |
|---|
| temperature and 1 bar67   |
| Figure 5-6. Sorption measurements of CH <sub>4</sub> -CO <sub>2</sub> on illite at 50°C temperature and 300 psi68 |
| Figure 5-7. CH4-CO2 sorption on Mancos shale samples unreacted or reacted with a synthetic                        |
| fracking fluid.   |
| TABLES  |
| Table 4-1. Lenard-Jones parameters of methane-organic wall interactions in the presence of the                    |
| heterogeneities. The epsilon parameter slightly varies with the heterogeneities on the                            |
| surface57   |
| Table 5-1. Experimental measurements of sorption capacities and sorption rates for the model                      |
| substances at 1 bar total pressure67  |
| Table 5-2. Experimental measurements of sorption capacities and sorption rates for a model                        |
| material at elevated temperatures and pressures   |
| Table 5-3. BET surface area measurements of shale samples   |

#### **NOMENCLATURE**

BET Brunauer-Emmett-Teller

CNTs carbon nanotubes

DNA deoxyribose nucleic acid DOE Department of Energy DOPA dihydroxyphenylalanine

DSC differential scanning calorimeter DTA Differential temperature analyzer

EDL electrical double layer EOS equation of state

EUR Estimated Ultimate Recoveries

FTIR Fourier Transform Infrared Spectroscopy GCMC grand-canonical Monte Carlo simulations

GIP gas in place

LDH layered double hydroxide

LDRD Laboratory Directed Research & Development

MC Monte Carlo

MD molecular dynamics

NMR nuclear magnetic resonance

PAMAM polyamidoamine PNA peptide nucleic acid PZC point of zero charge RNA ribose nucleic acid

SANS small angle neutron scattering
SEM scanning electron microscope
SNL Sandia National Laboratories
TEM transmission electron microscope
TGA thermal gravimetric analyzer

XRD X-ray diffraction XRF X-ray fluorescence

#### 1. INTRODUCTION

#### 1.1. Problem Statement and objective

The recent boom in shale gas production through hydrofracturing has reshaped the energy production landscape in the United States. The key issue related to shale gas production is illustrated in Figure 1-1. Wellbore production rates vary greatly among the wells within a single field and decline rapidly with time, thus bring up a serious concern with the sustainability of shale gas production (Hughes, 2013). Shale gas production starts with creating a fracture network by injecting a pressurized fluid in a wellbore. The induced fractures are then held open by proppant particles. During production, gas releases from the mudstone matrices, migrates to nearby fractures, and ultimately reaches a production wellbore. Given the relatively high permeability of the induced fractures, gas release and migration in low-permeability shale matrices is likely to be a limiting step for long-term wellbore production. Therefore, a clear understanding of the underlying mechanisms is crucial for the development of new technologies to maximize gas production and recovery.

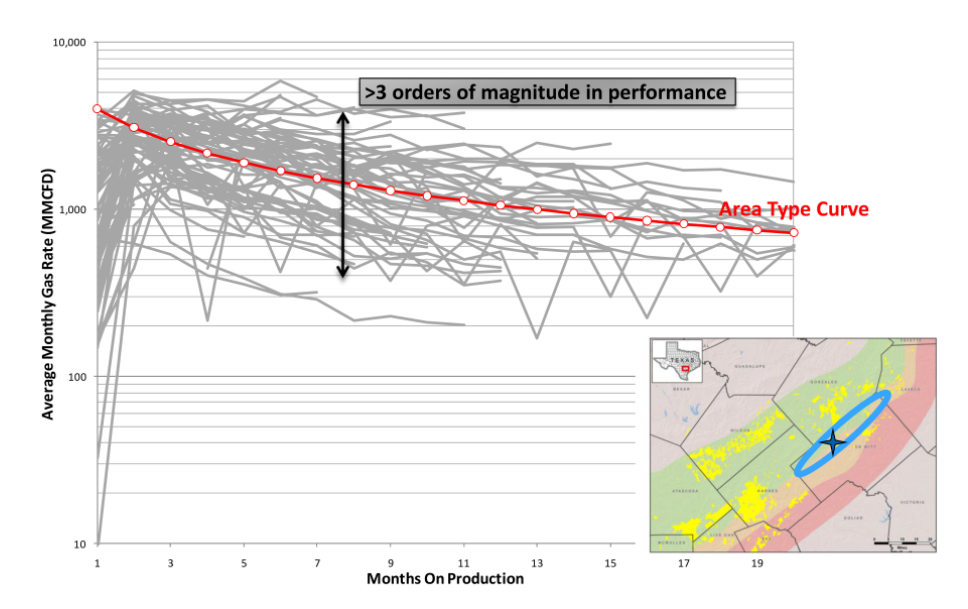


**Figure 1-1.** Wellbore production decline curves for Northern DeWitt County (Eagle Ford) (Robertson, 2013)

Shale gas formations have their own distinct characteristics: nanometer-scale pore sizes, extremely low permeability, high clay contents, significant amounts of organic carbon, and large spatial heterogeneities (Clarkson et al., 2012; Chalmers & Bustin, 2008). Methane in shale exists either as a compressed gas phase or as an adsorbed phase in nanopores, with the latter accounting for 20-85% of total gas in place (GIP) (Curtis, 2002; Mongtgomery et al., 2005). Methane could adsorb to both kerogen and clay minerals, though the relative importance is still controversial (Chalmers & Bustin, 2008; Ji et al., 2012; Gasparik et al., 2012). While the thermal maturation of kerogen may enhance methane sorption in shale probably due to an increase in nano-porosity, the presence of moisture seems to reduce methane sorption (Ross & Bustin, 2008, 2009). The predominant nanopores in shale have two important implications. Nanopores can substantially modify the physical and chemical properties of a chemical species (Wang et al., 2003, 2011). Molecular dynamics (MD) simulations indicate that the density and viscosity of methane in a confined environment could deviate significantly from those in the bulk phase (Diaz-Campos et al.,

2009; Ambrose et al. 2012; Didar and Akkutlu, 2013), potentially affecting the GIP estimation and overall gas recovery (Ambrose et al., 2012; Didar and Akkutlu, 2013). Nanopore can also modify gas flow behaviors in shale. The traditional assumption of no-slip boundary conditions in the Navier-Stokes equation breaks down at the nanometer scale, and so does the commonly used Darcian flow model (Javadpour et al., 2007). Instead, gas flows in shale should be formulated using the Klinkenberg slip or Knudson diffusion theory (Amann-Hildenbrand et al., 2012). Gas permeability can increase dramatically in pores with a diameter < 50nm due to nanopore confinement (Fathi et al., 2012).

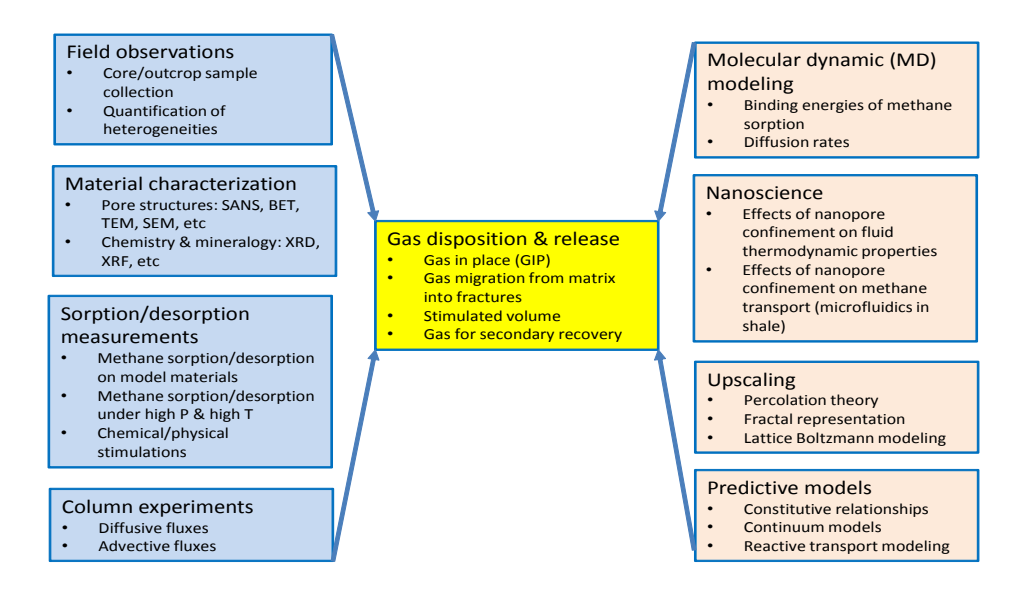


**Figure 1-2.** Integrated experimental and modeling approach to addressing gas disposition and release in shale. SANS: small angle neutron scattering; BET: Brunauer-Emmett-Teller; TEM: transmission electron microscope; SEM: scanning electron microscope; XRD: X-ray diffraction; XRF: X-ray fluorescence

The existing knowledge drawn from conventional reservoirs is not applicable to shale gas reservoirs (Javadpour et al., 2007). Effort has been made to understand un-conventional shale gas reservoirs, but the progress is limited. Existing methane sorption measurements are limited to relatively low temperatures and low pressures as well as to crushed samples; they don't necessarily reflect actual reservoir conditions; and data interpretation remains empirical. Large technical gaps still exist in our mechanistic understanding of gas disposition and release in shale matrices, especially regarding (1) how methane partitions into kerogen and clay minerals, (2) how this partitioning is controlled by nanopore structures of shale, (3) how methane releases from shale matrices to fractures, and (4) if this release can be enhanced by chemical additives or physical stimulation.

This report summarizes the results obtained from a Laboratory Directed Research & Development (LDRD) project entitled "Fundamental Study of Disposition and Release of Methane in a Shale Gas Reservoir". The objective of this project to use an integrated experimental and modeling study to fundamentally understand two important processes that directly control GIP in a reservoir and wellbore production: methane partitioning in the nanopores of mudstone matrices and methane transport from low-permeability matrices to fractures (Figure 1-2). The work has shown that nanopore confinement plays an important role in methane disposition and release in unconventional reservoirs.

#### 1.2. References

- Amann-Hildenbrand, A., Ghanizadeh, A., Krooss, B. M., 2012, Transport properties of unconventional gas systems. Mar. Petrol. Geol., 31, 90-99.
- Ambrose, R. J., Hartman, R. C., Diaz-Campos, M., Akkutlu, I. Y., Sondergeld C H., 2012, Shale gas-in-place calcualtions part 1: New pore-scale considerations. Soc. Petrol. Eng., 131772, 219-229.
- Chalmers, G. R. L., Bustin, R. P., 2008, Lower Cretaceous gas shales in northern British Columbia, part I: Geological controls on methane sorption capacity. Bull. Can. Petrol. Geol., 56, 1-21.
- Clarkson, C. R., Solano, N., Bustin, R. M., Bustin, A. M. M., Chalmers, G. R. L., He, L., Melnichenko, Y. B., Radlinski, A. P., Blach, T. P., 2013, Pore structure characterization of North American shale gas reservoirs using USANS/SANS, gas adsorption, mercury intrusion, Fuel, 103, 606-616.
- Curtis, J. B., 2002, Fractured shale-gas systems. Am. Assoc. Petrol. Geol. Bull., 86, 1921-1938.
- Diaz-Campos, M., Akkutlu, I. Y., Sigal R. F., 2009, A molecular dynamics study on natural gas solubility enhancement in water confined to small pore. Soc. Petrol. Eng. 124491, 1-10.
- Didar, B. R., Akkutlu, I. Y., 2013, Can molecules in nanopores inflence oil and gas recovery? SPE Workshop, Feb. 27 March 1, 2013, Santa Fe, New Mexico, USA.
- Fathi, B., Tinni, A., Akkutlu, I. Y., 2012, Correction to Klinkenberg slip theory for gas flow in nano-capillaries. Inter. J. Coal Geol., 103, 51-59.
- Gasparik, M., Ghanizadeh, A., Bertier, P., Gensterblum, Y., Bouw, S., Krooss, B. M., 2012, High-pressure methane sorption isotherms of black shales from the Netherlands. Energy & Fuel, 26, 4995-5004.
- Hughes, J. D., 2013, A reality check on the shale revolution. Nature, 494, 307-308.
- Javadpour F. Fisher D., Unsworth M., 2007, Nanoscale gas flow in shale gas sediments. JCPT, 46(10), 55-61.
- Ji, L., Zhang, T., Milliken, K. L., Qu, J., Zhang, X., 2012, Experimental investigation of main controls to methane adsorption in clay-rich rocks. Appl. Geochem., 27, 2533-2545.
- Montgomery, S. L., Jarvie D. M., Bowker K. A., Pallastro R. M., 2005, Mississippian Barnet Shale, Fort Worth basin, north-central Texas: shale gas play with multi-trillion cubic foot potential. Am. Assoc. Petrol. Geol., 89, 155-175.
- Robertson, L., 2013, Production decline in oil and gas shale reservoirs: What can we do to improve the performance? SPE Workshop, Feb. 27 March 1, 2013, Santa Fe, New Mexico, USA.
- Ross, D. J. K., Bustin, R. M., 2008, Characterizing the shale gas resource potential of Devonian–Mississippian strata in the Western Canada sedimentary basin: application of an integrated formation evaluation. Am. Assoc. Petrol. Geol. Bull. 92, 87–125.
- Ross, D. J. K., Bustin, R. M., 2009, The importance of shale composition and pore structure upon gas storage potential of shale gas reservoirs. Mar. Petrol. Geol. 26, 916–927.
- Wang, Y., Bryan, C., Xu, H., Gao, H., 2003, Nanogeochemistry: Geochemical reactions and mass transfers in nanopores. Geology, 31, 387-390.
- Wang, Y., Gao H., Xu, H., 2011, Nanogeochemistry: Nanostructures and their reactivity in natural systems. In: A. Parker and H. Russell, eds., Frontiers in Geochemistry, Wiley-Blackwell, p. 200-220.

#### 2. GEOCHEMISTRY OF NANOPORES

#### 2.1. Occurrence of Nanopores

Nanopores are ubiquitous in geologic media and constitute an integral part of the total porosity of geologic materials (Wang, 2014). For example, TEM observations reveal that diatomaceous materials exhibit both micrometer and nanometer-scale pores. The nanopores are regularly distributed with a pore size of ~ 3 nm. It has been proposed that these nanopores are formed in the template of biomolecules (probably proteins) (Ollver et al., 1995; Lobel et al., 1996), similar to a process used by material scientists to synthesize nanoporous materials (e.g., Kresge et al. 1992). Nanosized channels are often seen along a grain boundary or a reaction front. These channels are believed to provide necessary transport passages for mass transfer during mineral reactions, such as polysomatic reactions (Veblen, 1991). Nanopores are also commonly associated with iron oxyhydroxides in soils (Wang et al., 2003), though the mechanism for this association is not clear. Along with those nanopores in a rigid mineral framework, there are also "softly confined" nanopores (or nano-channels) within biologic cells, which may play an important role in regulating cell functions (e.g., Movahed and Li, 2012). Similar nanopores also occur in natural organic macromolecules such as humic substances. Those pores may directly control the fate of trace metals or organic contaminants in natural systems (Pignatello, 1998).

The contribution of nanopores to the total surface area of geologic materials can be very significant. In Bhorizon soils, the pores with diameters smaller than 100 nm account for 10 - 40% of total porosity of the soils (Görres et al., 2000). Aringhieri (2004) has determined that, in a range of pores measured (1.5 to 100 nm), pores of ~2.0 nm effective radius account for more than other pore size for the total microporosity of both soils and clays. Those small pores are closely related to clay components in soils. Similar pore size distributions have also been observed in silica and alumina gel – basic components of natural clay materials. The porosity of Georgia kaolinite is dominated by pores smaller than 10 nm (Tardy and Nahon, 1985). Suetsugu et al. (2004) have measured the pore size distributions of alluvial soils and volcanic soils from the B-horizon. They have found that nanopores with diameters < 50 nm account for up to 20% of the total pore volumes. Since the specific surface area is inversely proportional to the pore diameter, the contribution of nanopores to the total surface area in those materials is expected to be very high, most likely > 90%.

Nanopores can be formed by the precipitation and subsequent aggregation of nanosized secondary mineral particles during rock alteration. Simonyan et al. (2012) have studied the diffusive transport of water in porous fresh and altered mid-ocean ridge basalts, using H<sub>2</sub>O and D<sub>2</sub>O exchange experiments. They have found that rock alteration leads to the precipitation of tiny secondary minerals such as chlorite and the formation of such mineral assemblages in the pore volume creates numerous nanoscale pores. The most important factor influencing the diffusivity of solute species in the porous basalts is the pore size, and the nanosized (<100 nm) pores directly control solute transport in hydrothermal systems where igneous rocks are altered and secondary minerals formed.

#### 2.2. Fluids and lons in Nanopores

The thermodynamic properties of confined fluids have emerged as an important area for geochemical research (Dysthe and Wogelius, 2006). A fluid confined in a nanopore can behave differently from its bulk phase. A Van der Waals equation of state has been derived for a fluid confined in a simple-geometry nanopore using a perturbation method (Zarragoicoechea and Kuz, 2002; Meyra et al., 2004; Keshavarzi et al., 2006). For a Lennard-Jones fluid in a neutral pore, the shift in critical temperature can be described by (Zarragoicoechea and Kuz, 2004):

$$\frac{T_c - T_{cp}}{T_c} = 0.9409 \frac{\sigma}{r_p} - 0.2415 \left(\frac{\sigma}{r_p}\right)^2$$
 (2-1)

where  $T_c$  is the critical temperature of the bulk fluid;  $T_{cp}$  is the critical temperature of the fluid in a pore with a radius  $r_p$ ; and  $\sigma$  is the size parameter of the Lennard-Jones potential. The shift in critical pressure can be described by a similar expression. Figure 2-1 shows the prediction of critical temperature shift for some common gases as a function of pore size, as compared with experimental measurements. The critical temperature increases with decreasing pore size. Interestingly, the density of a gaseous phase usually increases in nano-confinement. For example, using nuclear magnetic resonance (NMR) spectroscopy, Hiejima et al. (2005) determined that the mean density of SF6 confined in porous Vycor glass is appreciably higher than bulk density in the gas phase and approaches bulk density in the liquid phase. The implication of this effect to the evaluation of gas in place in a shale gas reservoir is discussed in Section 2.6.

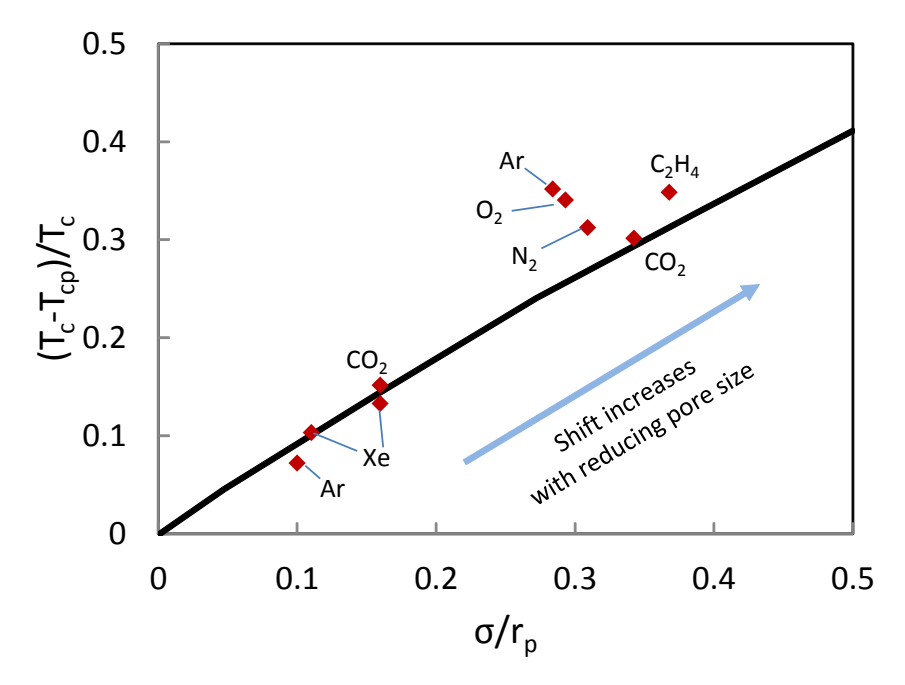


**Figure 2-1.** Shift of critical temperature of fluid as a function of pore size. The solid line is calculated from Equation (4).  $T_c$  is the critical temperature of the bulk fluid;  $T_{cp}$  is the critical temperature of the fluid in a pore with a radius  $r_p$ ; and  $\sigma$  is the size parameter of the Lennard-Jones potential. Modified from Zarragoicoechea and Kuz (2004).

The properties of water confined in a nanopore can deviate significantly from those of bulk water (Levinger, 2002). Takei et al. (2000) have studied the density and surface tension of water in nanopores of silica. They have shown that both the density and the surface tension in the nanopores (<5 nm) are smaller than those of the bulk phase and decrease with decreasing pore size. The density of water in pores decreases with an increase in the concentration of surface hydroxyl. The effect of surface on adsorbed water can extend up to 4 nm from the solid surface. This anomalous behavior of water in nanometer silica pores is determined by hydrogen bond formation in the pore. In a hydrophobic pore, water tends to form

clusters, leading to significant stabilization of water in the hydrophobic pore environment (Ohba et al., 2004). Water confined into a carbon nanotube forms collectively a molecular wire held together by strong hydrogen bonds (Köfinger et al., 2008). This molecular wire can extend up to 0.1 mm.

One important change in water properties due to nano-confinement is the reduction of dielectric constant, which can greatly affect ion behaviors in nanopores. Using molecular dynamics (MD) simulations, Senapati and Chandra (2001) have calculated the dielectric constant of liquid water confined in a spherical nanocavity. Their simulations suggest that the dielectric constant of water in the cavity is significantly smaller than that of bulk water. A nearly 50% decrease of the dielectric constant is estimated for water confined in a cavity with a diameter of 1.2 nm. Note that, in their simulations, the cavity surface is assumed to be neutral and thus there is no electrostatic interaction between the water molecules and the cavity surface. The calculated reduction of the dielectric constant thus originates purely from spatial confinement. This reduction is expected to be even larger if water molecules interact with a charged cavity surface. The reduction of water dielectric constant ( $\epsilon$ ) inevitably leads to the decrease in the solvation energy of a metal cation ( $\Delta G_{s,M^{n+}}$ ), according to Born solvation equation:

$$\Delta G_{sM^{n+}} = \omega_{M^{n+}} (1/\varepsilon - 1) \tag{2-2}$$

where  $\omega_{M^{n+}}$  is the Born solvation coefficient of cation  $M^{n+}$ . A low dielectric constant reduces the affinity for metal hydration in aqueous solution, thus promoting the inner-sphere complexation for metal sorption (Wang et al., 2003b).

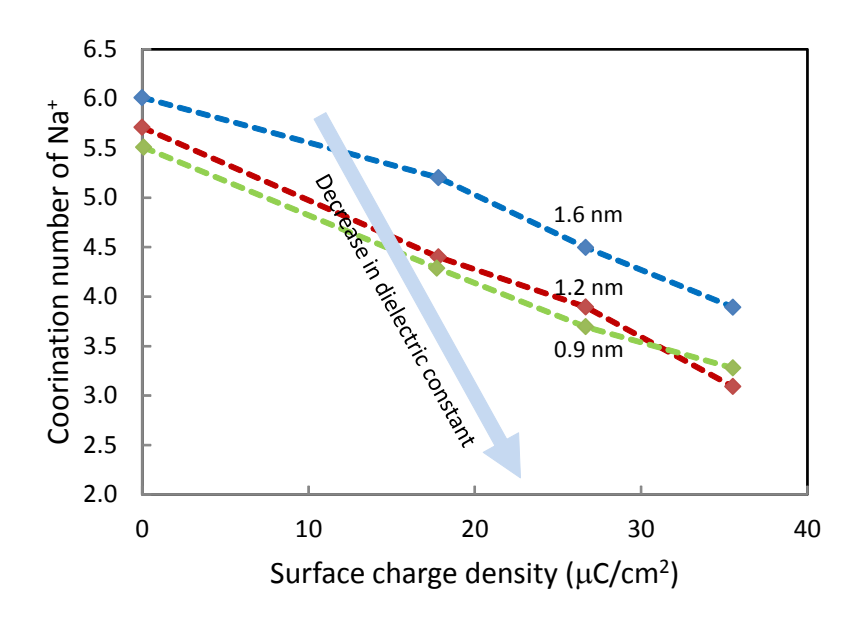


**Figure 2-2.** Average coordination number of Na<sup>+</sup> ions confined in a grapheme slit as a function of silt width and surface charge density. Data are from Kalluri et al. (2011). Dielectric constant of water decreases with reducing slit width and increasing surface charge density.

The hydration of Li<sup>+</sup>, Na<sup>+</sup>, K<sup>+</sup>, F<sup>-</sup>, and Cl<sup>-</sup> inside carbon nanotubes at temperatures ranging from 298 to 683 K has been studied using MD simulations (Shao et al., 2008). Simulation results show that the first coordination shells of the five ions still exist in the nano-confinement and the first coordination shells of cations are considerably less ordered in the nanotube than in the bulk solution. Similarly, MD simulations were also performed to study the structural properties of aqueous electrolyte NaCl confined within graphene pores for varying pore size and surface charge density (Kalluri et al., 2011). It has been found that, when the graphene sheets are neutral, most electrolytes remain outside of the pores. As the graphene surface charge density increases, more Na<sup>+</sup> and Cl<sup>-</sup> enter the pores. At the maximum graphene surface charge density considered (40  $\mu$ C/cm<sup>2</sup>), the ionic concentration within the pores can be ~10 times as high as that outside of the pores, with the maximum partition coefficient obtained when the pore width is 1.2 nm. The first dense peak of either Na<sup>+</sup> or Cl<sup>-</sup> ions occurs near the oppositely charged surfaces, thus preventing ions from complete hydration. Figure 2-2 shows the average coordination number of Na<sup>+</sup> ions as a function of the pore width and the graphene surface charge density. The coordination number of an ion decreases with increasing pore surface charge density and decreasing pore size, consistent with the prediction from Equation (2-2).

Nano-confinement may enhance ion selectivity. MD simulations have been performed to study alkali halide behavior in a charged nano-slit (Wander and Shuford, 2011). It has been found that the behavior of halides can change significantly due to nanopore confinement. In bulk solution, halides are distinguished from each other only by subtle variations induced by ion size. Upon confinement, the properties of alkali halides can deviate from the expected molecular trends. Besides reducing solubility and altering permittivity, confinement effects can amplify the differences between different ions that would be largely indistinguishable in bulk. Yang and Garde (2007) modeled the partitioning of cations into negatively charged nanopores from an aqueous solution. They have demonstrated that, over a range of intermediate negative charge densities, nanopores display both thermodynamic and kinetic selectivity toward partitioning of the larger  $K^+$  and  $K^+$  ions into their interior over the smaller  $K^+$  ions. Specifically, the driving force is in the order  $K^+ > Cs^+ > Na^+$ , and  $K^+$  and  $K^+$  and  $K^+$  ions enter the pore much more rapidly than  $K^+$  ions. At higher charge densities, the driving force for partitioning increases for all cations - it is highest for  $K^+$  ions - and becomes similar for  $K^+$  and  $K^+$  ions. Understanding of ion sorption selectivity in nanopores is of great importance for predicting chemical partitioning between rock matrix and pore fluid.

The interlayer of clay provides an idea system for studying fluids confined within a two-dimensional environment. The interlayer of clay can be viewed as an end member of nanopore confinement. Using MD simulations, Wang et al. (2004) investigated liquid water in a nanoslite formed by two parallel, electrically neutral but hydrophilic brucite surfaces. The simulation results show that the hydrophilic substrate significantly influences the near-surface water structure, with both the H-bond donation to the surface oxygen atoms and the H-bond acceptance from the surface hydrogen atoms in the first surface layer of H<sub>2</sub>O molecules. The profiles of oxygen and hydrogen atomic density and H<sub>2</sub>O dipole orientation show significant deviation from the corresponding structural properties of bulk water to distances as large as 1.5 nm. Furthermore, based on both MD modeling and neutron scattering measurements, Skipper et al. (2006) studied the structure and dynamics of interlayer fluid species in expansive clays. They have found that for monovalent ions the contribution to the first coordination shell of a counterion from the clay surfaces increases with counterion radius, giving rise to inner-sphere complexes for K<sup>+</sup> and Cs<sup>+</sup>, while divalent cations, such as Ca<sup>2+</sup>, tend to form outer-sphere complexes. The divalent cation complexes are able to hold adjacent clay layers together, thereby preventing clay swelling. Confined water molecules form hydrogen bonds to each other and to the clays' surfaces, and their local environment relaxes to close to the bulk water structure within two molecular layers of the clay surface.

The structure and hydration affinity of interlayer water play an important role in cation exchange of clay materials. Van Loon and Glaus (2008) measured Cs<sup>+</sup> sorption on compacted sodium bentonite. They have

shown that material compaction enhances Cs<sup>+</sup> uptake in the interlayer. This enhancement is due to a reduction of the interlayer space, leading to a lower ability of the interlayer water for hydration. Cations with lower hydration energies, such as Cs<sup>+</sup>, would tend to enrich in the interlayer, while cations with higher hydration energies such as Na<sup>+</sup> would tend to accumulate in the bulk water where water is easily available for hydration. The result implies that a direct transfer of thermodynamic data from a diluted to a compacted system must be cautious. Miller and Wang (2012) provide a comprehensive review of radionuclide interaction with clays in both dilute and heavily compacted systems, pointing out a close connection between radionuclide uptake and material structures and textures.

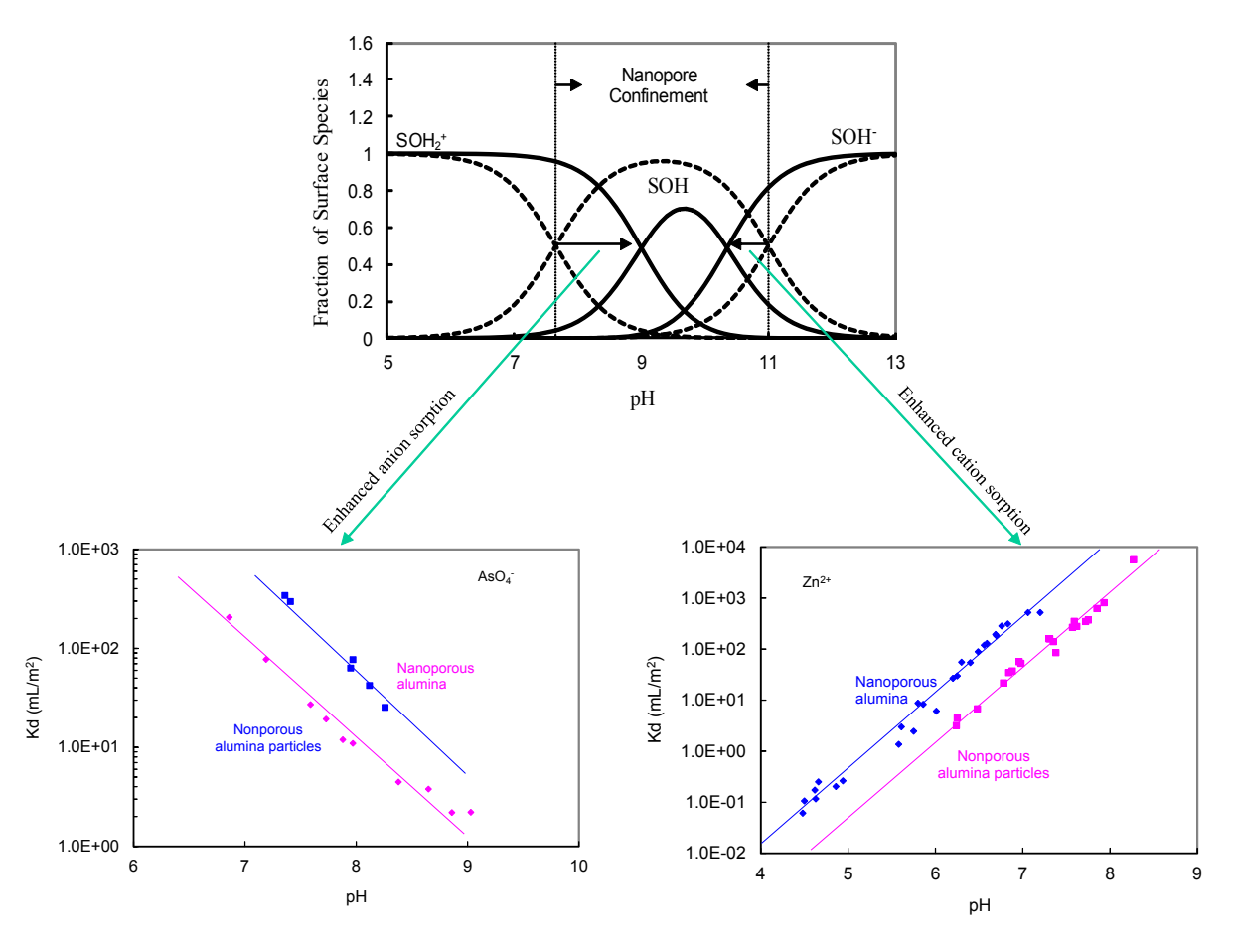


**Figure 2-3.** Effects of nanopore confinement on pore surface chemistry and surface sorption of alumina materials. Kd is the sorption coefficient normalized to surface area. Nanopore confinement makes the pore surface either more negatively or more positively charged, leading to the enhancement of surface sorption for both cations and anions. The surface areas of the materials were measured with a  $N_2$  BET method using a Micrometritics Gemini 2360 surface analyzer. Upper panel: dash lines – nonporous alumina, solid lines – nanoporous alumina. Modified from Wang et al. (2003b, 2011).

#### 2.3. Surface Chemistry of Nanopores

Nano-confinement can significantly modify mineral-water interface chemistry. Wang et al. (2002) performed acid-base titrations on two alumina materials of similar phase and crystallinity: nanoporous materials and nonporous alumina particles. From the titration data, the point of zero charge (PZC) is calculated to be 9.1 for nanoporous alumina and 8.7 for alumina particle, both within the range reported for aluminum oxides. Thus, the nanopore confinement seems to have little effect on the PZC of the pore surface, similar to the finding for nanoparticles (Madden et al., 2006). However, the titration results indicate a significant difference in surface charge density between the two materials. The surface charge density on the nanoporous alumina is much higher than that on the alumina particles under same chemical conditions. Furthermore, the surface charge on a confined surface is less sensitive to ionic strength changes than that on an unconfined surface. The surface acidity constants for the two materials are estimated to be:  $pK_1 = 9.0$ ,  $pK_2 = 10.3$  for nanoporous alumina, and  $pK_1 = 7.7$ ,  $pK_2 = 11.0$  for alumina particles (Wang et al., 2003b). Therefore, because of nanopore confinement, the separation between the two acidity constants is significantly reduced. Consequently, within the nanopores, the neutral surface species is suppressed, thus making the nanopore surface either more positively or more negatively charged (Figure 2-3, upper panel).

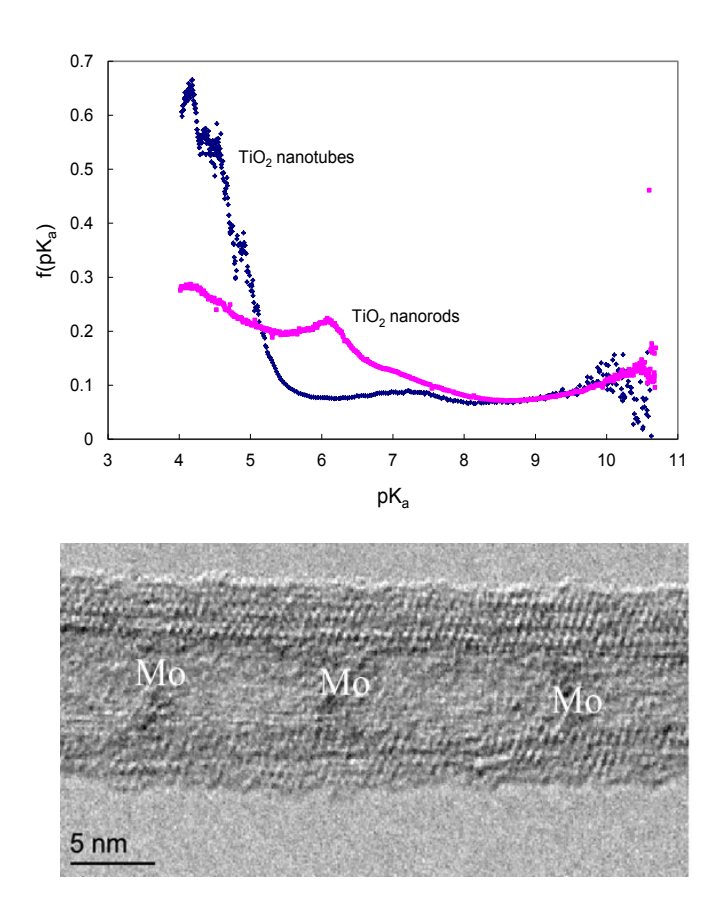


**Figure 2-4.** Surface acidity distributions of  $TiO_2$  nanotubes and nanorods (upper panel) and preferential precipitation of Mo clusters inside nanotubes (lower panel).  $pK_a$  is a surface acidity constant calculated from the single-pK model (Contescu et al., 1993).  $f(pK_a)$  is the distribution of acidity constant. Modified from Wang et al. (2008, 2011).

The difference in surface acidity between confined and unconfined surfaces is further confirmed for a  $TiO_2$  oxide system (Wang et al., 2008). A similar titration study was conducted on  $TiO_2$  nanotubes and nanorods. The two materials were synthesized under comparable hydrothermal conditions.  $TiO_2$  nanotubes possess both confined (internal) and unconfined (external) surfaces whereas the nanorods only have the external surface. The surface acidity distributions, f(pK), on the materials are calculated using a so-called single-pK model, which assumes that proton uptake on a single of population binding sites follows a Langmuir isotherm (Contescu et al. 1993). As shown in Figure 2-4, two materials display distinct surface acidity distributions.

Associated with the shift in mineral surface acidity, the sorption capability of nanopore surface is also enhanced. Wang et al. (2003b) measured the sorption coefficients (Kd) of  $Zn^{2+}$  and  $AsO_4^{3-}$  on both nanoporous alumina and nonporous alumina particles. It has been found that the sorption coefficient normalized to the surface area for nanoporous alumina is systematically ~10 times higher than that for alumina particles for both the cation and the anion (Figure 2-3, lower panels). Two factors may contribute to this enhancement. First, as discussed above, because of nano-confinement, nanopore surfaces become either more positively or more negatively charged, thus increasing the sorption affinity for both cations and anions. Secondly, water inside nanopores is more restrained, thus reducing the tendency for ion hydration and consequently increasing the possibility for stronger, inner-sphere surface complexation of adsorbates.

It is unclear what exactly causes the observed difference in surface acidity between a confined and an unconfined surface. It could be caused by a change in the solid phase, in the fluid phase, or in both. Since in the systems considered water is a main confined phase, the difference in surface acidity is probably due to water property changes, which seems supported by first principle MD simulations (Liu et al., 2011). The MD simulations suggest that the acidity of water confined in a smectite interlayer is significantly different from that of the bulk water. The layer charge of clay seems directly responsible for the water acidity enhancement in smectite, since the neutral pore has no effect on water dissociation while the charged one does. The acidity of free water in the interlayer can be as low as 11.3. The first shell water coordinated with Mg<sup>2+</sup> can be even low (10.1 to 10.4).

The above discussions again suggest that ion sorption measurements on disaggregated geologic materials may not necessarily represent chemical/physical conditions in actual systems, because the disaggregation may inevitably destroy part of nanopore structures in the original material (Wang et al., 2003b, 2011). Conca and Wright (1992) measured the apparent sorption coefficient of radionuclides in bentonite as a function of compaction density. They observed that the sorption capability of the material first decreased with physical compaction and then increased at a high compaction density. This phenomenon can be easily explained by the nanopore confinement effect discussed above. The initial decrease in sorption may be attributed to the reduction of sorption site accessibility as the material is compacted. Then, further compaction likely creates more nanopores at expense of large pores, thus enhancing radionuclide sorption (Wang et al., 2003b).

#### 2.4. Phase Transition and Chemical Reactions in Nanopores

Numerous studies have been conducted on water phase transition in nanopore confinement. Teixeira et al. (1997) have suggested that the behavior of confined water is similar to that of supercooled water at low (~30 °K) temperatures. Based on extensive MD simulations, Takaiwa et al. (2008) have documented the existence of at least nine ice phases for water in single-walled carbon nanotubes at atmospheric pressure, each having a structure that maximizes the number of hydrogen bonds under the cylindrical confinement. Furthermore, Cámara and Bresme (2004) have studied a Lennard-Jones liquid confined in a wedge shaped nanopore and shown that small deviations from the parallel slit geometry result in non-uniform

pressures and density profiles along the pore. Under conditions of high confinement and thermodynamic states close to the triple point, wedge shaped pores can induce the formation of solid phases in specific alternating regions within the pore. This alternating liquid-solid induced by the pore geometry have an important implication to transport dynamics in the pore. It is found that the diffusion inside narrow pores can be surprisingly fast (10-9 m/s), the same order of magnitude as that in the bulk phase (Bresme and Cámara, 2006). Furthermore, Beckstein and Sansom (2003) have found that water in a short (0.8 nm) hydrophobic nanotube with radii of 0.35 to 1 nm experiences frequent oscillations between a liquid-like and a vapor-like phase with fluctuation frequency in the nanosecond scale. This behavior can be explained as capillary evaporation alternating with capillary condensation, driven by pressure fluctuations in the water outside the pore.

Interestingly, nano-confinement can even induce a phase separation of a fluid between small and large pores if both are connected. Using a density functional method, Belonoshko (1989) have studied the properties of a binary mixture of water-CO<sub>2</sub> confined in an infinitely long cylindrical pore of 0.8 to 2.5 nm in diameter, over a wide range of pressure and composition relevant to metamorphic processes. The results show that the confined fluid differs significantly in composition from the bulk phase with which it is equilibrated. The difference diminishes with increasing pore size and become negligible at a pore diameter of 2.5 nm. The results provide a reasonable explanation for the formation of CO<sub>2</sub>-dominant fluid inclusions from a bulk aqueous phase.

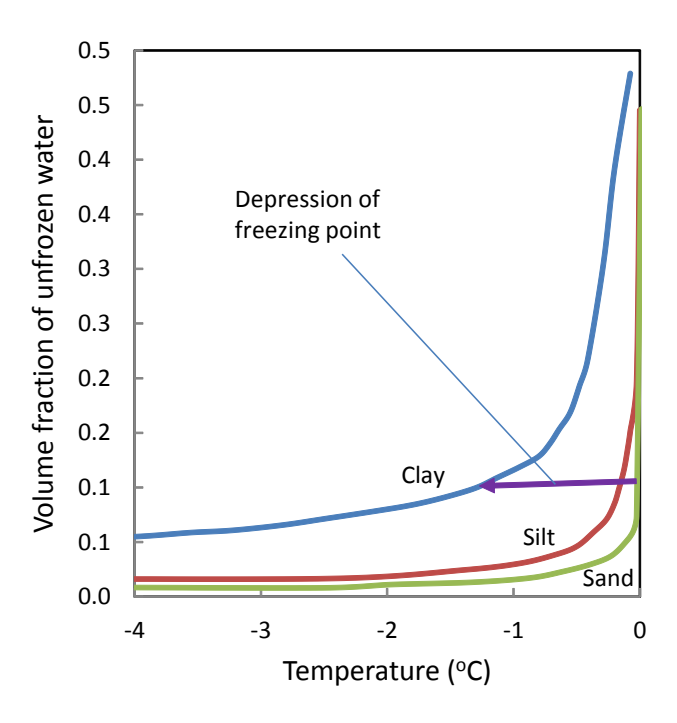


**Figure 2-5.** Volume fractions of unfrozen water in clay, silt and sand in permafrost regions. Data from Osterkamp and Bum (2002).

The freezing point of water can be significantly reduced in nano-confinement. The depression of freezing point ( $\Delta T$ ) can be estimated from Gibbs-Thomson equation (Bréchignac et al., 2006; Alcoutlabi and McKenna, 2005):

$$\Delta T = \frac{4(\gamma_{WS} - \gamma_{Wl})}{\rho_T \Delta H_m} T_b \tag{2-3}$$

where  $\gamma_{ws}$  and  $\gamma_{wl}$  are the wall-solid and wall-liquid interface tensions, respectively;  $\rho$  is the density of liquid; r is the radius of nanopores;  $\Delta H_m$  is the bulk enthalpy of melting; and  $T_b$  is the freezing point of the bulk liquid phase. As indicated in Equation (2-3), the depression is inversely proportional to the pore size. The predicted depression of freezing point is consistent with the measurements of electric conductivity of shale zones, which show much more conductive than the adjacent sandstone in a permafrost area (Diaz-Campos et al., 2009). The shale zones are dominated by nanosized pores (see Section 2.6). It is also interesting to note that unfrozen water contents in soils at a given temperature in a permafrost region depend on soil types, with high values usually associated with clay formations (Figure 2-5) (Osterkamp and Burn, 2002). This implies that, even in a permafrost zone, a certain portion of water may remain unfrozen, which is expected to play an important role in facilitating chemical reactions and mass transfers in permafrost regions.

Nano-confinement can modify other chemical reactions within the pores as well. Interesting work has recently been conducted on the structural stability of three different nucleic acids within the interlayer of Mg-Al layered double hydroxide (LDH) (Swadling et al., 2012). Mg-Al-LDH is used to mimic the confinement condition imposed by green rust, which is also a layered double hydroxide and has been postulated to be present in the early reducing ocean environment. MD calculations show that deoxyribose nucleic acid (DNA) has enhanced Watson–Crick hydrogen-bonding when intercalated within the LDH clay interlayers, as compared with intercalated ribose nucleic acid (RNA) and peptide nucleic acid (PNA). The results suggest that a mineral-based origin of life may have favored DNA as the information-storage biomolecule over potentially competing RNA and PNA, thus providing a possible route to modern biology from the RNA world. In the RNA world hypothesis, self-replicating RNA molecules are assumed to be the precursors to modern life, which are based on DNA, RNA and proteins (Powner et al., 2009).

Nano-confinement can even lead to chemical reactions that may not be anticipated from a bulk system. For instance, Miller et al. (2013) studied iodide uptake by a suite of clay minerals with varying degrees of isomorphic substitution, chemical composition, and mineral structure over a wide range of swamping electrolyte identities (NaCl, NaBr, KCl) and concentrations. They have found that iodide uptake behaviors form distinct trends with cation exchange capacity and mineral structure. These trends change substantially with electrolyte composition and concentration, but do not appear to be affected by solution pH. The experimental results thus suggest that iodide may directly interact with clay interlayers, which contradicts the traditional thinking that negatively charged clay plates would prevent anions from entering a clay interlayer. A hypothesis is then developed that iodide enters a clay interlayer through the formation of ion-pairs (e.g., NaI<sub>(aq)</sub>) promoted by the reduction in dielectric constant of water confined in the interlayer.

Most geochemical reactions take place at mineral grain contacts or within pores in porous geologic media. Mineral crystallization in nano-confinement is an important process that needs to be considered in geochemical studies. If mineral precipitation is viewed as a dehydration process, the reduction of water dielectric constant by nano-confinement is expected to promote preferential mineral precipitation inside nanopores, a process similar to the non-electrical exclusion of ions in thin water films (Zilberbrand 1997). To test the idea, Wang et al. (2003a) conducted a MoO<sub>4</sub><sup>2-</sup> sorption experiment on TiO<sub>2</sub> nanotubes. Nanotubes provide an ideal system for such testing because both the inner surface (the confined surface) and the outer surface (the unconfined surface) of a tube have almost identical chemical compositions and

crystal structures. They first suspended TiO<sub>2</sub> nanotubes in an aqueous solution spiked with MoO<sub>4</sub><sup>2-</sup> and then imaged the nanotubes, both chemically and structurally, using a HRTEM. The HRTEM images reveal clean outer surfaces and pillar-like Mo clusters precipitated inside the nanotubes (Figure 2-4, lower panel), clearly indicating the preferential enrichment of trace metal in a confined space. This observation is consistent with the study of natural samples, in which uranium(VI) is reduced by annite – a Fe(II)-contained mica (Ilton et al., 2004). X-ray adsorption spectroscopy (XAS) data indicate that U(VI) is partially reduced in the interlayer space of annite. A TEM examination shows nanometer uranium-rich zones in the interlayer regions for the experiments with relatively high uranium sorption. A similar mechanism may be responsible for the enrichment of trace metals in ore deposits, for example, for the formation of "invisible" gold nanoparticles, especially those along mineral grain boundaries, in Carlintype of gold deposits (Palenik et al., 2004).

The same mechanism may bear an important implication to dolomite formation. Dolomite is common in ancient platform carbonates but rare in Holocene sediments; there has been not much success in precipitating this mineral in the laboratory at Earth surface temperatures (e.g., Warren 2000). It has been proposed that dolomite formation is inhibited by strong Mg<sup>2+</sup> hydration (as compared to Ca<sup>2+</sup>) (de Leeuw and Parker 2001). Nano-confinement may help reduce Mg<sup>2+</sup> hydration and therefore the kinetic barrier for dolomite precipitation at low temperature (Wang et al., 2003b).

Nanopore confinement also affects the kinetics of metal redox reaction and release. Jung et al. (2012) studied the potential effect of nanopores on U(VI) reduction. Batch sorption/desorption experiments showed that 80–90% of U(VI) sorbed to nanoporous alumina could be retained from 2-week extraction with 50 mM NaHCO<sub>3</sub>, whereas the percentages for nonporous α alumina were much lower (~10%). XAS data confirmed that U(VI) sorbed to non-porous alumina was rapidly and completely reduced to nanoparticulate uraninite by quinone, while the reduction of U(VI) sorbed to nanoporous alumina was slow and incomplete (<5% reduction after 1 week). The observed kinetic effect of nanopore confinement on U redox reaction has important implications to the development of efficient remediation techniques for subsurface uranium contamination because the efficiency of in situ bioremediation depends on how effectively and rapidly U(VI) bound to sediment or soil can be converted to an immobile phase or vice versa (Jung et al., 2012).

The preferential enrichment and enhanced retention of a heavy metal in nanopores as discussed above has a profound implication to the evaluation of the fate and bioavailability of a metalloid contaminant in a natural environment. A microbial cell, with a typical size of micrometers, is 10-1000 times larger than nanopores. This size disparity precludes any possibility for microorganisms to directly access a heavy metal inside nanopores, thus effectively reducing the bioavailability of the metal.

A similar argument can be made for organic compounds as well. Zimmerman et al. (2004) tested dihydroxyphenylalanine (DOPA) adsorption and enzymatic degradation on nanoporous alumina and silica and their nonporous counterparts. They found that the surface area-normalized adsorption capacity was greater for the nanoporous minerals than that for the nonporous counterparts, consistent with the preferential enhancement of metals in nanopores as discussed above. Interestingly, they also found that, for DOPA sorbed onto nanoporous alumina and silica, the enzyme activity was 3-40 times lower than that for the substrate sorbed to nonporous minerals. This observation indicates that nanopore sorption can not only preclude the direct access of an adsorbed organic compound by microbial cells but also limit extracellular enzymatic degradation of the compound. Furthermore, nanopore sorption can also inhibit abiotic degradation of organic contaminants by protecting them in confined spaces with little reactive water, slowing down hydrolysis and other water-mediated transformations (Cheng et al., 2012). If the pore surface is hydrophobic, an adsorbed organic compound would have difficulties diffusing out and therefore would have reduced bioavailability (Alexander, 2000). All these effects combined may significantly slow organic contaminant degradation in soils and sediments (Curry et al., 2007). These

processes are considered to be responsible, at least in part, for the aging effect and the preservation of organic matter in natural systems, thus ultimately affecting global carbon cycles (Zimmerman et al.,2004).

Minerals precipitated in nanopores are nanoparticles, and their size is ultimately controlled by the size of the confining pores. The phase stability and transition of such particles is highly sensitive to particle size and interfacial chemistry (especially the interfacial chemistry between the precipitates and the confining mineral phases). Some polymorphs that cannot be stable in a bulk phase may become stable when they are confined in nanopores (Rengarajan et al., 2011; Hamilton et al., 2012). The effect of nanoconfinement on crystal polymorphs has been studied for tailored release of polymorphic drugs and optimization of polymorphic materials for optical and electronic applications; however, its potential implications to mineral precipitation and dissolution in geochemical systems have not been fully explored.

Mineral growth under confinement may create a crystallization force on pore walls. Such a force has been considered as a main mechanism for salt weathering of construction materials and rocks (Espinosa-Marzal and Scherer, 2010). For crystal growth in small pores (<100 nm), the influence of crystal curvature on crystallization can become significant. For illustration of this concept, assume a material with a bimodal pore size distribution, which is common in geologic media, since pores in rocks usually consist of pore bodies and smaller pore necks. The difference in crystallization force ( $\Delta P_c$ ) between a small pore (with a curvature of  $\kappa_1$ ) and a large pore (with a curvature of  $\kappa_2$ ) can be calculated by (Espinosa-Marzal and Scherer, 2010):

$$\Delta P_c = \gamma_{cl} (\kappa_1 - \kappa_2) \tag{2-4}$$

When the radii of small pores are less than 100 nm, the material is expected to be sensitive to damage by salt crystallization. This effect may contribute to the so-called honeycomb weathering of rocks or construction materials (Rodriguez-Navarro et al., 1999).

#### 2.5. Fluid Flow and Transport in Nanopores

Fluid flows and ion transport in nanosized channels have been an active research area known as nanofluidics. Since a fluid in a nanometer channel contains a great many fewer molecules than that in a macroscopic system, the discrete nature of molecules becomes important in nanofluidic transport. The applicability of conventional continuum theory is often checked by a dimensionless parameter, called Knudsen number (Kn) (Sparreboom et al., 2010):

$$Kn = l/L (2-5)$$

where L is the characteristic length of a fluid flow system and l is the mean free path of a molecule for a gas or the interaction length of a molecule with its neighbors (usually  $\sim 10$  molecular length) for a liquid. A Kn number of 1 corresponds to the transition between continuum and discrete flows. For a gaseous flow, the continuum Navier-Stokes equation is valid only for Kn < 0.1. The non-slip boundary condition is applicable for a stricter limit of Kn < 0.001. For a liquid flow, the fluidic phenomena in flow channels of 100 nm - 100 m can still be described by the continuum theory (Hu and Li, 2007). However, in flow channels smaller than 100 nm, a liquid can no longer be considered as a continuum but as an ensemble of individual molecules. The surface-to-volume ratio of the fluid becomes so high that the properties of the fluid can deviate significantly from those of the corresponding bulk phase. As a result, the non-slip condition does not hold fully (Hu and Li, 2007).

Knudsen number can also be used to classify flow regimes (Ziarani and Aguilera, 2012). For Kn < 0.01, a viscous flow dominates and Darcy's law applies. For 0.01 < Kn < 0.1, a slip flow regime occurs and gas molecules experience slipping at the solid surface. In this case, Darcy's equation with Klinkenberg or Knudsen's correction may apply. For 0.1 < Kn < 10, a transition flow regime occurs, which can involve both slip and diffusion flows. The traditional flow dynamic equation starts to fail, and the flow regime becomes non-Darcian flow. In the non-Darcian flow regime, the fluid flux is no longer linearly proportional to the pressure gradient applied (Liu and Birkholzer, 2012). Darcy's equation with Knudsen's correction could be used, but its validity is questionable, especially for Kn approaches to 10.

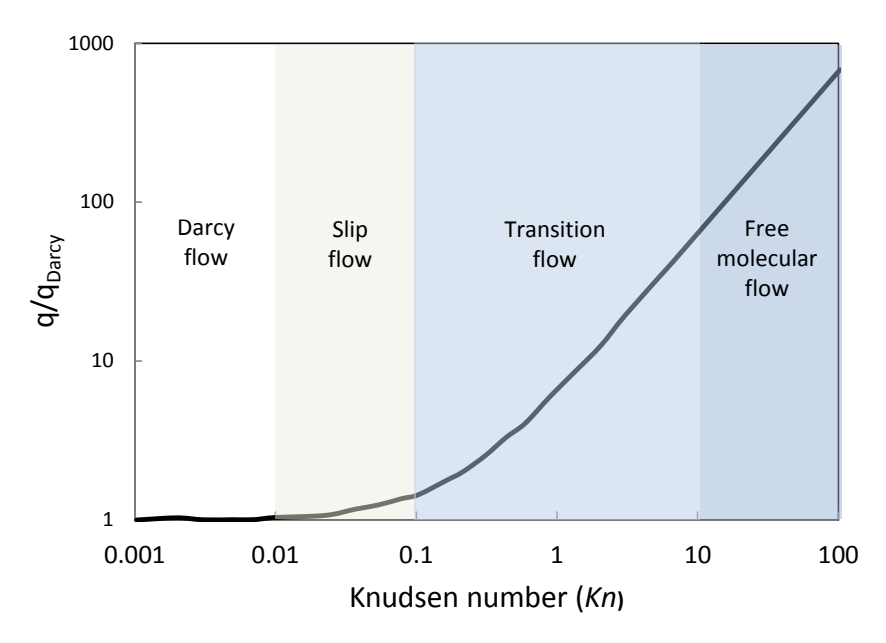


**Figure 2-6.** Correction factor for Darcy flow of methane as a function of Knudsen number. q is the flux.  $q_{Darcy}$  is the flux predicted by Darcy's law. Data from Ziarani and Aguilera (2012).

Knudsen's correction factor ( $f_c$ ) to Darcy's equation is given by (Ziarani and Aguilera, 2012):

$$f_c = \frac{q}{q_{Darcy}} = \left[1 + \alpha(Kn)Kn\right] \left[1 + \frac{4Kn}{1 - bKn}\right]$$
 (2-6)

where q is the fluid flux;  $q_{Darcy}$  is the flow flux calculated from Darcy's equation;  $\alpha$  is the rarefaction coefficient, which is a function of Kn; b is a constant equal to -1 for slip flow. For illustration, the correction factor for methane as a function of pore throat radius under various pressure and temperature conditions is plotted in Figure 2-6. Note that the traditional Darcy's equation under-predicts the flux by 10 to 100 times for high Kn cases, for example, in shale gas reservoirs. For Kn > 10, the flow regime becomes a free molecular flow. Continuum fluid flow equations completely break down, and Knudsen's diffusion equations or other alternative methods must be used. This flow regime occurs in shale gas or coalbed methane formations. Knudsen's diffusion equation is expressed by (Javadpour et al., 2007):

$$\frac{q\rho M}{\phi A} = D_k \frac{\Delta P}{RTL} \tag{2-7}$$

where  $\rho$  is the density of gas; M is the molar mass; P is the pressure of gas;  $\phi$  is the porosity of shale; A is the surface area; and L is the diffusion distance.

As the pore size decreases, the surface-to-volume ratio of a fluid flow system increases, and the interfacial effect become more and more important. The behavior of a fluid flow in a nanochannel is determined, to a large extent, by the interaction of fluid molecules with the channel wall. Experimental studies show higher than expected water flow rates through carbon nanotubes (CNTs) as compared to the values calculated using classical continuum fluid mechanics models (Mattia and Calabrò, 2012 and references therein). This effect is due to the specific interactions between the nanotube wall and the fluid. When a polar liquid such as water is in contact with a hydrophobic surface, the attraction among fluid molecules is stronger than that between the fluid molecules and the solid surface. Consequently, the fluid molecules try to minimize the interaction with the solid surface, leading to an increase in liquid flow velocity as compared to the bulk fluid. Hummer et al. (2011) conducted MD simulations for water in a carbon nanotube. The result shows that the wet-dry transition (i.e. the entry or exist of water to or from the tube) is sensitive to the strength of water-wall interaction. For example, small changes in electrostatic state or pore geometry can drive a transition from a water-full to a total dry state or vice versa. The simulations also show that the number of hydrogen bonds with such nanotubes is reduced with respect to that in bulk water. Interestingly, in narrow carbon nanotubes, water diffusion is about 2 times faster than that in bulk water, in contrast to hydrophilic pores in which water diffusion is generally reduced (Sansom and Biggin, 2011). In a hydrophilic nanosized channel, the movement of polar molecules such as water would be retarded due to the strong interaction between the fluid molecules and the channel wall. Mattia and Calabrò (2012) have shown that the liquid flow enhancement factor ( $\eta$ ) can be approximately estimated

$$\eta \approx \frac{8\mu L D_s}{r^2 [\pi_s + \gamma_{LV} (1 + \cos\theta)]} \tag{2-8}$$

where  $\mu$  is the viscosity of the liquid; L is the length of the nano-channel; r is the radius of the channel;  $D_s$  is the surface diffusion coefficient;  $\pi_s$  is the film pressure of the adsorbed vapor;  $\gamma_{LV}$  is the liquid-vapor surface tension; and  $\theta$  is the contact angle. Mineral surfaces exhibit a full range of hydrophobicity or hydrophilicity. The implication of fluid flow enhancement (or retardation) to geochemical mass transfer yet needs to be clarified.

Size exclusion is an important process that needs to be considered in molecular transport in nanopores. The size-exclusion effect on the diffusion of large organic molecules has been demonstrated by measuring the diffusion rates of polyamidoamine (PAMAM) dendrimers in silica colloidal nanopores (Ignacio-de Leon and Zharov, 2011). The size of PAMAM dendrimers used ranges from 1.9 to 5.7 nm. The nanofrits made up of uniform silica colloid particles contain nanopores of 7.5 and 27.2 nm radii. The diffusion rates of PAMAM dendrimers were found to decrease with the size of the diffusive molecules, a 3-fold decrease from the smallest to the largest molecules. A similar size exclusion effect may be responsible for anomaly CO<sub>2</sub> vs. CH<sub>4</sub> diffusion observed in coal (Wang et al., 2012a). Experimental measurements of CO<sub>2</sub> and CH<sub>4</sub> diffusion in coal show that the diffusion rate of CO<sub>2</sub> is usually 1-2 orders of magnitude higher than that for CH<sub>4</sub>, which seems to violate a fundamental physical law because CH<sub>4</sub> is lighter. This anomaly behavior has been attributed to large energy barriers and directional force fields induced by nanometer-scale pore space (Wang et al., 2012a). CH<sub>4</sub> molecules need to overcome much higher energy barriers than CO<sub>2</sub> in the pore throats with the sizes close to the kinetic diameter of CH<sub>4</sub> molecules. Similar processes are likely to occur in shale oil/gas reservoirs and may control gas/oil migration and extraction in low-permeability unconventional reservoirs.

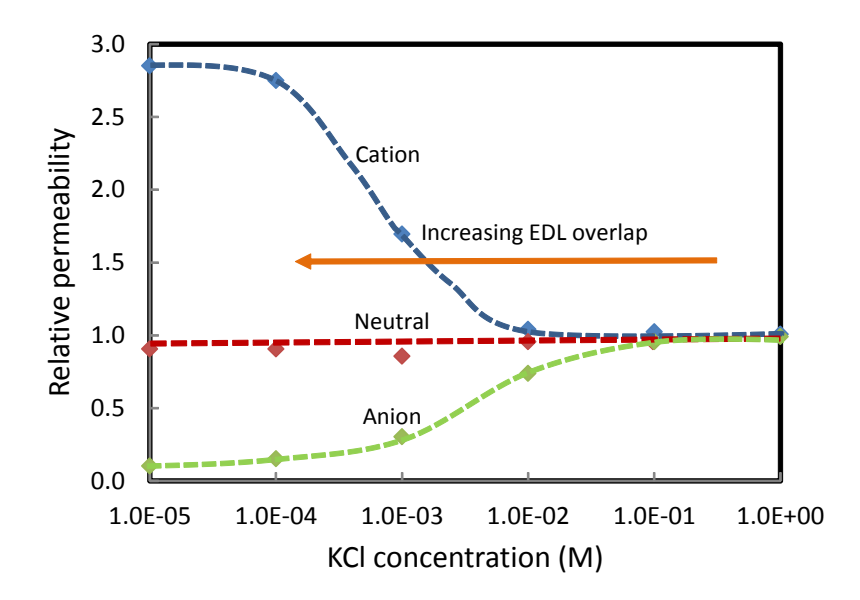


**Figure 2-7.** Relative permeability of cation, anion and neutral species in a 3  $\mu$ m long and 50 nm high slit as a function of background electrolyte (KCl) concentration. Relative permeability is the measured permeability normalized to the value determined at [KCl] = 1.0 M. Data are from Plecis et al. (2005).

The effect of pore size becomes even more complicated for ion transport due to the development of a charged water-solid interface. For a charged surface, as the pore size decreases, the electrical double layer (EDL) eventually becomes overlapped and compressed, which is expected to have a profound effect on ion transport. This effect apparently depends on the ionic strength of solution, which determines the thickness of EDL. The thickness of EDL is roughly characterized by the Debye screening length ( $\lambda_d$ ):

$$\lambda_d = \sqrt{\frac{\epsilon_0 \epsilon_r RT}{2 F^2 I}} \tag{2-9}$$

where F is the Faraday constant;  $\epsilon_0$  is the permittivity of vacuum;  $\epsilon_r$  is the dielectric constant of water; and I is the ionic strength. In a dilute solution, the EDL can extend up to 100 nm. The ion exclusionenrichment in nanofluidic transport was studied for a nanoslit with 50 nm high and 3 µm long (Plecis et al., 2005). The relative permeability of fluorophores with different net charges was measured under different concentrations of background electrolyte (KCl) concentrations. As shown in Figure 2-7, the negatively charged channel surface excludes anions when the overlap of EDL occurs at low KCl concentrations. In contrast, the transport of cations is enhanced. Carrillo-Tripp et al. (2004) have showed that the energy cost of constraining a hydrated potassium ion inside a narrow nanopore is smaller than the energy cost of constraining the smaller hydrated sodium ion. The former allows for a greater distortion of its hydration shell and, therefore, can maintain a better coordination. In this way, the larger ion can go through narrow pores more easily than the smaller ones. This apparent contradiction is directly relevant to the molecular basis of ion selective nanopores. Since it does not depend on the molecular details of the pore, this mechanism could also operate in many different types of nanotubes, from biological to synthetic. Such work may provide additional insight into fluid and ion transport in low-permeability shale formations. Shale or other clay-rich formations may act as semipermeable membranes for geologic fluids (Hanshaw, 1973; Tournassat and Appelo, 2011).

Surface charge density plays an important role in regulating fluid and ion transport in nanopores. Hao et al. (2013) have performed MD simulations for water and ion permeation through a charged carbon nanotube to mimic a hydrophilic surface. It is found that the water flow decreases monotonously with the increase of charge density for both positively and negatively charged channels, indicating that water molecules experience larger friction at higher surface charge densities. Whereas, the ion (Na<sup>+</sup>, Cl<sup>-</sup>) flow reaches a maximum at the surface charge density of 2.05 e/nm<sup>2</sup>. Both water and ion flows increase with the channel size. The flow fluxes for both water and ions diminish when the size of the channel approaches to 1.5 nm.

#### 2.6. Shale as a Nanocomposite Material

Shale is a natural nanocomposite material that is made, in a large proportion, of clay particles, which, by definition, contain a significant fraction of nanoparticles. As mentioned in Section 1.1, shale has its own distinct characteristics: nanometer-scale pore sizes, extremely low permeability, significant amounts of organic carbon, and large spatial heterogeneities (Clarkson et al., 2013; Chalmers and Bustin, 2008). Existing knowledge drawn from conventional gas-oil reservoirs is not applicable to shale formations. A typical pore size distribution in shale is shown in Figure 2-8 (upper panel). Shale samples exhibit multiple scales of pore sizes and are dominated by  $\sim 1$  - 100 nm pores. The pore size distribution in shale seems to exhibit a fractal nature. It is known that a chemical reaction in a fractal medium may lead to a different reaction kinetics (e.g., a different chemical reaction order) from that in a non-fractal medium (Kopelman, 1988). How this fractal pore size distribution affects chemical reactions and mass transfers in shale is an interesting topic for a future study.

Methane in shale exists either as a compressed gas phase or as an adsorbed phase in nanopores, with the latter accounting for 20-85% of total gas-in-place (GIP) (Curtis, 2002; Montgomery et al., 2005). Methane can adsorb to both kerogen and clay minerals (Chalmers and Bustin, 2008; Ji et al., 2012; Gasparik et al., 2012). The thermal maturation of kerogen may enhance methane sorption in shale probably due to an increase in nano-porosity, while the presence of moisture seems to reduce methane sorption (Ross and Bustin, 2008, 2009). Pore characterization of mudstone samples from the Mississippian Barnet Shale of the Fort Worth Basin, Texas, shows that these rocks predominantly contain 5-750 nm pores, mostly occurring in kerogen grains as intraparticle pores (Zhang et al., 2012). The abundance of pores in kerogen is directly related to the thermal maturity of organic matter. The pores of 5-50 nm size developed in high maturity kerogen. At lower pressures methane seems to adsorb more readily on higher maturity kerogen. Using gas sorption, Valenza et al. (2013) measured the surface areas and pore volumes of 30 samples from basins across North America. The measurements show that the specific surface area of the organic component evolves from ~50 m²/g in immature shale to ~500 m²/g in dry-gas reservoirs. The high surface area is attributed to the development of nanometer-scale pores in kerogen.

The predominant nanopores in shale have two important implications. As discussed in previous sections, nanopore confinement can substantially modify the physical and chemical properties of a chemical species (Wang et al., 2003b, 2011). MD simulations indicate that the density and viscosity of methane in a confined environment could deviate significantly from those in the bulk phase (Diaz-Campos et al., 2009; Didar and Akkutlu, 2013), potentially affecting the GIP estimation and overall gas recovery. Methane in a small pore is expected to be structured as a result of fluid-pore wall interactions. Depending on the pore size, a bulk-fluid phase may be present at the center of a small pore. However, as the pore size reduces, no bulk-fluid phase can exist, and all gas in the pore should be treated as an adsorbed phase. The density of the first adsorbed layer can be significantly higher than that of the bulk gaseous phase. The smaller the pore, the higher the adsorbed phased density is (Ambrose et al. 2012). Shale gas can also dissolve into formation water. A MD study shows that methane solubility in water can be enhanced by

nanopore confinement (Diaz-Campos et al., 2009). Methane solubility in nanopores is increased by about one order of magnitude as compared to that in the bulk phase (i.e., in absence of pore walls) (Figure 2-8, middle panel). The solubility is extremely sensitive to wettability; it increases with increasing either hydrophobicity or hydrophilicity of the pore wall surface. This implies that the dissolved methane in formation water may represent a significant component of the total gas reserve in an unconventional reservoir.

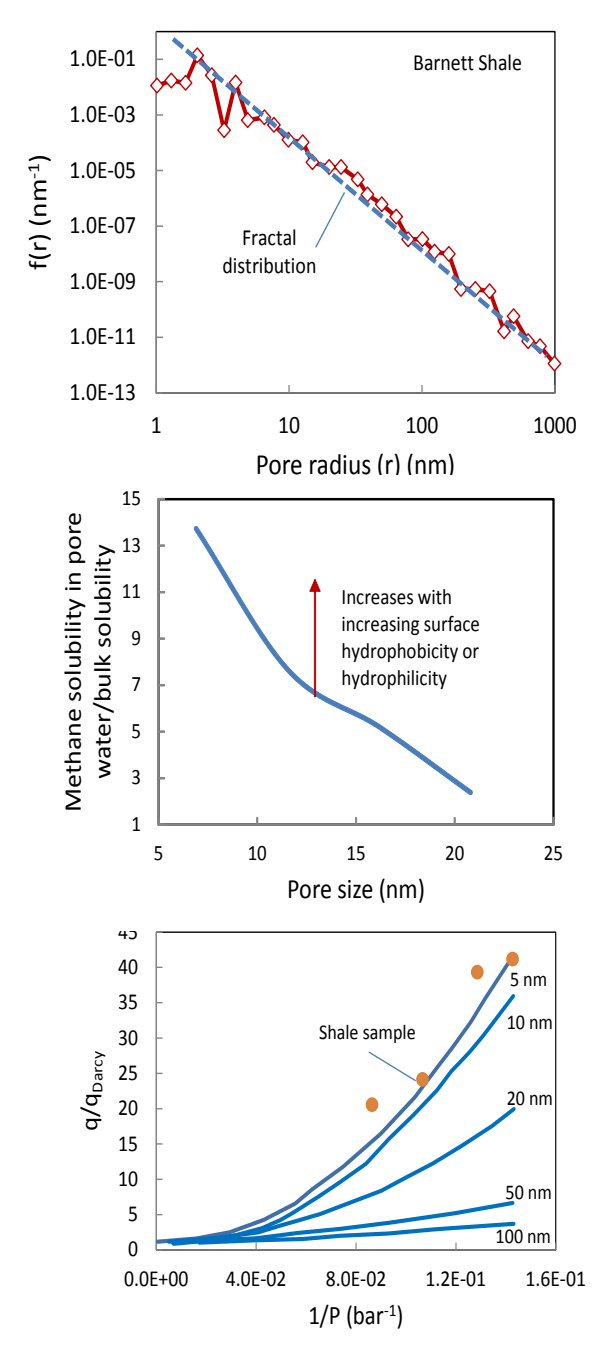


**Figure 2-8.** Pore size distribution, methane solubility, and possible methane flow behavior in shale. f(r) is the pore size distribution in terms of the number of pores. q is the flux.  $q_{Darcy}$  is the flux predicted by Darcy's law. P is the gas pressure. Data from Clarkson et al. (2013), Diaz-Campos et al. (2009), and Fathi et al. (2012).

As discussed in the previous section, nanopore confinement can also modify gas flow behaviors in shale. The traditional assumption of no-slip boundary conditions in the Navier-Stokes equation breaks down at the nanometer scale, as does the commonly used Darcian flow model (Javadpour et al., 2007). Instead, gas flows in shale should be formulated using the Klinkenberg slip or Knudson diffusion theory (Amann-Hildenbrand et al., 2012). The apparent permeability coefficients of a gas are not constant but decreases with increasing mean pressure. Gas permeability can increase dramatically in pores with a diameter < 50 nm due to nano-confinement (Fathi et al., 2012) (Figure 2-8, lower panel). While both the Klinkenberg and Knudsen corrections have been successfully applied to single-phase flow (e.g., for low *Kn* cases), the slip-flow in multiphase-multicomponent system remains largely unexplored (Amann-Hildenbrand et al., 2012). MD simulations of a CO<sub>2</sub>-CH<sub>4</sub> mixture in carbon nanopores indicate complex interactions between the two components. For example, the displacement of CH<sub>4</sub> by CO<sub>2</sub> in the nanopores may be divided into two stages. In the first stage, the co-adsorbed CO<sub>2</sub> may enhance CH<sub>4</sub> adsorption. In the second stage, the stronger affinity of CO<sub>2</sub> to graphitic surfaces may cause the displacement of CH<sub>4</sub> from carbon materials.

In addition, the pore throat size in shale seems to directly control hydrocarbon release from shale matrices. Rylander et al. (2013) have quantified hydrocarbon expelling with a careful comparison between well log and core measured by nuclear magnetic resonance signals. They have found that oil produced in the lower Eagle Ford Shale appears to come from pores that have a diameter of 250 nm or greater. Thus, better understanding of fluid flows in nanopores may help better predict gas/oil mobility in unconventional reservoirs and develop new technologies for enhanced gas/oil recovery.

#### 2.4. References

- Alcoutlabi, M., McKenna, G. B., 2005, Effects of confinement on material behaviour at the nanometer size scale. J. Phy. Condens. Matter 17, R461-R524.
- Alexander, M., 2000, Aging, bioavailability, and overestimation of risk from environmental pollutants. Environ. Sci. Technol. 34, 4259-4265.
- Amann-Hildenbrand, A., Ghanizadeh, A., Krooss, B. M., 2012, Transport properties of unconventional gas systems. Mar. Petrol. Geol. 31, 90-99.
- Ambrose, R. J., Hartman, R. C., Diaz-Campos, M., Akkutlu, I. Y., Sondergeld, C H., 2012, Shale gas-in-place calcualtions part 1: New pore-scale considerations. Soc. Petrol. Eng. 131772, 219-229.
- Aringhieri, R, 2004, Nanoporosity characteristics of some natural clay minerals and soils. Clays and Clay Minerals 52, 700-704.
- Bazylinski, D. A., Moskowitz, B. M., 1997, Microbial biomineralization of magnetic iron minerals: Microbiology, magnetism and environmental significance. Reviews in Mineralogy, 35, 181-223.
- Beckstein, O., Sansom, M. S. P., 2003, Liquid-vapor oscillations of water in hydrophobic nanopores. PNAS 100, 7063-7068.
- Belonoshko, A. B., 1989, The thermodynamics of the aqueous carbon dioxide fluid within thin pores. Geochim. Cosmochim. Acta 53, 2581-2590.
- Bréchignac, C., Houdy, P., Lahmani, M. (eds.), 2006, Nanomaterials and Nanochemistry. Springer, 747p. Bresme, F., Cámara, L. G., 2006, Computer simulation studies of crystallization under confinement conditions, Chemical Geology 230, 197-206.
- Cámara, L. G., Bresme, F., 2004, Liquids confined in wedge shaped pores: nonuniform pressure induced by pore geometry. Journal of Chemical Physics 120, 11355-11358.
- Carrillo-Tripp, M., Saint-Martin, H., Ortega-Blake, I., 2004, Minimalist molecular model for nanopore selectivity. Physical Review Letters 93, 168104/1-4.
- Chalmers, G. R. L., Bustin, R. P., 2008, Lower Cretaceous gas shales in northern British Columbia, part I: Geological controls on methane sorption capacity. Bull. Can. Petrol. Geol. 56, 1-21.

- Cheng, H., Hu, E., Hu, Y., 2012, Impact of mineral micropores on transport and fate of organic contaminants: A review. J. Contaminant Hydrology 129-130, 80-90.
- Clarkson, C. R., Solano, N., Bustin, R. M., Bustin, A. M. M., Chalmers, G. R. L., He, L., Melnichenko, Y. B., Radlinski, A. P., Blach, T. P., 2013, Pore structure characterization of North American shale gas reservoirs using USANS/SANS, gas adsorption, mercury intrusion, Fuel, 103, 606-616.
- Conca, J. L., Wright, J., 1992, Diffusion and flow in gravel, soil, and whole rock. Applied Hydrogeology 1, 5-24.
- Contescu, C., Jagiello, J., Schwarz, J. A., 1993, Heterogeneity of proton binding-sites at the oxide solution interface. Langmuir 9, 1754-1765.
- Curry, K. J., Bennett, R. H., Mayer, L. M., Curry, A., Abril, M., Biesiot, P. M., Hulbert, M. H., 2007, Direct visualization of clay microfabric signatures driving organic matter preservation in finegrained sediment. Geochim. Cosmochim. Acta 71, 1709-1720.
- Curtis, J. B., 2002, Fractured shale-gas systems. Am. Assoc. Petrol. Geol. Bull. 86, 1921-1938.
- de Leeuw, N. H., Parker, S. C., 2001, Surface-water interactions in the dolomite problem. Physical Chemistry and Chemical Physics 3, 3217-3221.
- Diaz-Campos, M., Akkutlu, I. Y., Sigal, R. F., 2009, A molecular dynamics study on natural gas solubility enhancement in water confined to small pore. Soc. Petrol. Eng. 124491, 1-10.
- Didar, B. R., Akkutlu, I. Y., 2013, Can molecules in nanopores influence oil and gas recovery? SPE Workshop, Feb. 27 March 1, 2013, Santa Fe, New Mexico, USA.
- Dysthe, D. K., Wogelius, R. A., 2006, Confined fluids in the Earth's crust Properties and processes. Chemical Geology 230, 175-181.
- Espinosa-Marzal, R. M., Scherer, G. W., 2010, Advances in understanding damage by salt crystallization. Accounts of Chemical Research 43, 897-905.
- Fathi, B., Tinni, A., Akkutlu, I. Y., 2012, Correction to Klinkenberg slip theory for gas flow in nanocapillaries. Inter. J. Coal Geol., 103, 51-59.
- Gasparik M., Ghanizadeh A., Bertier P., Gensterblum Y., Bouw S., Krooss B. M. (2012) High-pressure methane sorption isotherms of black shales from the Netherlands. Energy & Fuel, 26, 4995-5004.
- Görres, J. H., Stolt, M. A., Amador, J. A., Schulthess C. P., Johnson P., 2000, Soil pore manipulations to increase bioaccessible pore volume. In: Sililo, O. (ed.) Groundwater: Past Achievement and Future Challenge, A. A. Balkema, Rotterdam, Park City, pp.755-756.
- Hamilton, B. D., Ha, J.-M., Hillmyer, M. A., Ward, M. D., 2012, Manipulating crystal growth and polymorphism by confinement in nanoscale crystallization chambers. Accounts Chem. Res. 45(3), 414-423.
- Hanshaw, B. B., 1973, Ultrafiltration by a compacted clay membrane II. Sodium ion exclusion at various ionic strengths. Geochim. Cosmochim. Acta 37, 2311-2327.
- Hao, L., Su, J., Guo, H., 2013, Water permeation through a charged channel. J. Phys. Chem. B 117, 7685-7694.
- Hiejima, Y., Kanakubo, M., Aizawa, T., Kurata, Y., Ikushima, Y., 2005, Determination of fluid density confined in nanopore by means of NMR spectroscopy. Chemical Physical Letters 408, 344-347.
- Hu, G., Li, D., 2007, Multiscale phenomena in microfluidics and nanofluidics. Chem. Eng. Sci., 62, 3443-3454.
- Hummer, G., Rasaiah, J. C., Noworyta, J. P., 2011, Water conduction through the hydrophobic channel of a carbon nanotube. Nature 414, 188-190.
- Ignacio-de Leon, P. A. A., Zharov, I., 2011, Size-selective molecular transport through silica colloidal nanopres. Chem. Commun. 47, 553-555.
- Ilton, E. S., Haiduc, A., Moses, C. O., Heald, S. M., Elbert, D. C., Veblen, D. R., 2004, Heterogeneous reduction of uranyl by micas: Crystal chemical and solution controls. Geochim. Cosmochim. Acta 68, 2417-2435.
- Javadpour, F. Fisher, D., Unsworth, M., 2007, Nanoscale gas flow in shale gas sediments. JCPT 46(10), 55-61.

- Ji, L., Zhang T., Milliken, K. L., Qu, J., Zhang, X., 2012, Experimental investigation of main controls to methane adsorption in clay-rich rocks. Appl. Geochem. 27, 2533-2545.
- Jung, B. H., Boyanov, M. I., Konishi, H., Sun, Y., Mishra, B., Kemner, K. M., Roden, E. E., Xu, H., 2012, Redox behavior of uranium at the nanoporous aluminum oxide-water interface: Implications for uranium remediation. Environ. Sci. Technol. 46, 7301-7309.
- Kalluri, R. K., Konatham, D., Striolo, A., 2011, Aqueous NaCl solutions within charged carbon-slit pores: Partition coefficients and density distributions from molecular dynamic simulations. J. Phys. Chem. C 115, 13786-13795.
- Keshavarzi, T., Sohrabi, R., Mansoori, G. A., 2006, Analytic model for nano confined fluids phase transition: Applications for confined fluids in nanotube and nanoslit. J. Computational and Theoretical Nanoscience 3, 134-141.
- Köfinger, J., Hummer, G., Dellago, C., 2008, Macroscopically ordered water in nanopores. PNAS 105, 13218-13222.
- Kopelman, R., 1988, Fractal reaction kinetics, Science 241, 1620-1626.
- Kresge, C. T., Leonowicz, M. E., Roth, W. J., Vartuli, J. C., Beck, J. S., 1992, Ordered mesoporous molecular-sieves synthesized by a liquid-crystal template mechanism. Nature, 359, 710-712.
- Levinger, N. E., 2002, Water in confinement. Science 298, 1722-1723.
- Liu, H.-H., Birkholzer, J., 2012, On the relationship between water flux and hydraulic gradient for unsaturated and saturated clay. J. Hydrology 475, 242-247.
- Liu, X., Lu, X., Wang, R., Meijer, E. J., Zhou, H., 2011b, Acidities of confined water in interlayer space of clay minerals. Geochim. Cosmochim. Acta 75, 4978-4986.
- Lobel, K. D., West, J. K., Hench, L. L., 1996, Computational model for protein-mediated biomineralization of the diatom frustule. Marine Biology 126, 353-360.
- Madden, A. S., Hochella Jr., M. F., Luxton, T. P., 2006, Insights for size-dependent reactivity of hematite nanomineral surface through Cu<sup>2+</sup> sorption. Geochim. Cosmochim. Acta 70, 4095-4104.
- Mattia, D., Calabrò, F., 2012, Explaining high flow rate of water in carbon nanotubes via solid-liquid molecular interactions. Microfluid Nanofluid 13, 125-130.
- Meyra, A. G., Zarragoicoechea, G. J., Kuz, V. A., 2005, Thermodynamic equations for a confined fluid at nanometric scale. Fluid Phase Equilibria 230, 9-14.
- Miller, A., Kruichak, J., Mills, M., Wang, Y., 2013, Iodide interactions with clay minerals batch and diffusion studies, submitted to the 2013 International High-Level Radioactive Waste Management Conference, Albuquerque, 28 April-2 May 2013.
- Miller, A. W., Wang, Y., 2012, Radionuclide interaction with clays in dilute and heavily compacted systems: A critical review. Environ. Sci. Technol. 46, 1981-1994.
- Montgomery, S. L., Jarvie, D. M., Bowker, K. A., Pallastro, R. M., 2005, Mississippian Barnet Shale, Fort Worth basin, north-central Texas: shale gas play with multi-trillion cubic foot potential. Am. Assoc. Petrol. Geol. 89, 155-175.
- Movahed, S., Li, D., 2012, Electrokinetic transport through the nanopores in cell membrane during electroporation. J. Collod. Interface Sci. 369, 442-452.
- Ohba, T., Kanoh, H., Kaneko, K., 2004, Affinity transformation from hydrophilicity to hydrophobicity of water molecules on the basis of adsorption water in graphitic nanopores. J. Am. Chem. Soc. 126(5), 156-1562.
- Ollver, S., Kuperman, A., Coombs, N., Lough, A., Ozln, G. A., 1995, Lamellar aluminophosphates with surface patterns than mimic diatom and radiolarian microskeletons. Nature 378, 47-50.
- Osterkamp, T. E., Burn, C. R., 2002, Permafrost, in: Holton, J. R. Pyle, J., and Curry, J. A., eds., Encyclopedia of Atmospheric Sciences, New York, Academic Press, p.1717-1729.
- Palenik, C. S. Utsunomiya, S., Reich, M., Kesler, S. E., Wang, L. M., Ewing, R. C., 2004, "Invisible" gold revealed: Direct imaging of gold nanoparticles in a Carlin-type deposit. American Mineralogist 89, 1359-1366.
- Pignatello, J. J., 1998, Soil organic matter as nanoporous sorbent of organic pollutants. Adv. Colloid Interface Sci. 76-77, 445-467.

- Plecis, A., Schoch, R. B., Renaud, P., 2005, Ionic transport phenomena in nanofluidics: Experimental and theoretical study of the exclusion-enrichment effect on a chip. Nano Letters 5, 1147-1155.
- Powner, M. W., Gerland, B., Sutherland, J. D., 2009, Synthesis of activated pyrimidine ribonucleotides in prebiotically plausible conditions. Nature 459, 239-242.
- Rengarajan, G. T., Enke, D., Steinhart, M., Beiner, M., 2011, Size-dependent growth of polymorphs in nanopores and Ostwald's step rule of stages. Phys. Chem. Chem. Phys. 13, 21367-21374.
- Rodriguez-Navarro, C., Doehne, E., Sebastian, E., 1999, Origins of honey weathering: The role of salts and wind. Geological Society of American Bulletin 111, 1250-1255.
- Ross, D. J. K., Bustin, R. M., 2008, Characterizing the shale gas resource potential of Devonian–Mississippian strata in the Western Canada sedimentary basin: application of an integrated formation evaluation. Am. Assoc. Petrol. Geol. Bull. 92, 87–125.
- Ross, D. J. K., Bustin, R. M., 2009, The importance of shale composition and pore structure upon gas storage potential of shale gas reservoirs. Mar. Petrol. Geol. 26, 916–927.
- Rylander, E., Singer, P. M., Jiang, T., 2013, NMR T<sub>2</sub> Distributions in the Eagle Ford Shale: Reflections on pore size. SPE International SPE-164554.
- Sansom, M. S. P., Biggin, P. C., 2001, Water at the nanoscale. Nature 414, 156-158.
- Senapati, S., Chandra, A., 2001, Dielectric constant of water confined in a nanocavity. J. Phys. Chem. B 105, 5106-5109.
- Shao, Q., Huang, L., Zhou, J., Lu, L., Zhang, L., Lu, X., Jiang, S., Gubbins, K. E., Shen, W., 2008, Molecular simulation study of temperature effect on ionic hydration in carbon nanotubes. Phys. Chem. Chem. Phys. 10, 1896-1906.
- Simonyan, A. V., Dultz, S., Behrens, H., 2012, Diffusive transport of water in porous fresh to altered mid-ocean ridge basalts. Chemical Geology 306-307, 63-77.
- Skipper, N. T., Lock, P. A., Titiloye, J. O., Swenson, J., Mira, Z. A., Howells, W. S., Fernandez-Alonso, F., 2006, The structure and dynamics of 2-dimensional fluid in swelling clays. Chemical Geology 230, 182-196.
- Sparreboom, W., van den Berg, A., Eijkel, J. C. T., 2010, Transport in nanofluidic systems: a review of theory and applications. New Journal of Physics 12, 015004.
- Suetsugu, A., Imoto, H., Mizoguchi, M., Miyazaki, T., 2004, Effects of nanoscale pores in soils on carbon evolution under extremely dry conditions. Soil Science and Plant Nutrition 50, 891-897.
- Swadling, J. B., Coveney, P. V., Greenwell, H. C., 2012, Stability of free and mineral-protected nucleic acids: Implications for the RNA world. Geochim. Cosmochim. 83, 360-378.
- Takaiwa, D., Hatano, I., Koga, K., Tanaka, H., 2008, Phase diagram of water in carbon nanotubes. PNAS 105, 39-43.
- Takei, T., Mukasa, Kofuji, M., Fuji, M., Watanabe, T., Chikazawa, M., Kanazawa, T., 2000, Changes in density and surface tension of water in silica pores. Colloid Polym. Sci. 278, 475-480.
- Tardy, Y., Nahon, D., 1985, Geochemistry of laterites, stability of al-goethite, al-hematite, and Fe<sup>3+</sup>-kaolinite in bauxites and ferricretes: an approach to the mechanism of concretion formation. American Journal of Science 285, 865-903.
- Teixeira, J., Zanotti, J. M., Bellissent-Funel, M. C., Chen, S. H., 1997, Water in confined geometries. Physica B, 234, 370-374.
- Tornassat, T., Appelo, C. A. J., 2011, Modeling approaches for anion-exclusion in compacted Nabentonite. Geochim. Cosmochim. Acta 75, 3698-3710.
- Valenza II, J. J., Drenzek, N., MarQues, F., Pagels, M., Mastalerz, M., 2013, Geochemical controls on shale microstructure. Geology 41, 611-614.
- Van Loon, L. R., Glaus, M. A., 2008, Mechanical compaction of smectite clays increase ion exchange selectivity for cesium. Environ. Sci. Technol. 42, 1600-1604.
- Veblen, D. R., 1991, Polysomatism and polysomatic series: A review and applications. American Mineralogist 76, 801-826.
- Wander, M. C. F., Shuford, K. L., 2011, Alkali halide interfacial behavior in a sequence of charged slit pores. J. Phys. Chem. C 115, 23610-23619.

- Wang, F. Y., Zhu, Z. H., Massarotto, P., Rudolph, V., 2012a, Kinetic mobility and connectivity in nanopore networks. AIChE Journal 58, 364-376.
- Wang, J., Kalinichev, A. G., Kirkpatrick, R. J., 2004, Molecular modeling of water structure in nano-pore between brucite (001) surfaces. Geochim. Cosmochim. Acta 68, 3351-3365.
- Wang, Y., 2014, Nanogeochemistry: Nanostructures, emergent properties and their control on geochemical reactions and mass transfers, Chemical Geology, 378-379, 1-23.
- Wang, Y., Bryan C., Gao, H., Pohl, P., Brinker, C. J., Yu, K., Xu, H., Yang, Y., Braterman, P. S., Xu, Z., 2003a, Potential Applications of Nanostructured Materials in Nuclear Waste Management. Sandia National Laboratories, Albuquerque, NM, SAND2003-3313.
- Wang, Y., Bryan, C., Xu, H., Pohl, P., Yang, Y., Brinker, C. J., 2002, Interface chemistry of nanostructured materials: Ion adsorption on mesoporous alumina. J. Colloid Interface Sci. 254, 23-30.
- Wang, Y., Bryan, C., Xu H., Gao, H., 2003b, Nanogeochemistry: Geochemical reactions and mass transfers in nanopores. Geology 31, 387-390.
- Wang, Y., Gao, H., Xu, H., Siegel, M., Konishi, H., 2008, Surface chemistry and stability of nanostructured materials in natural aquatic environments. Geochim. Cosmochim. Acta 72, A1002.
- Wang, Y., Gao, H., Xu, H., 2011, Nanogeochemistry: Nanostructures and their reactivity in natural systems. In: A. Parker and H. Russell, eds., Frontiers in Geochemistry, Wiley-Blackwell, p. 200-220.
- Warren, J., 2000, Dolomite: Occurrence, evolution and economically important associations. Earth-Science Reviews 52, 1-81.
- Yang L., Garde, S., 2007, Modeling the selective partitioning of cations into negatively charged nanopores in water. Journal of Chemical Physics 126, 84706-1-8.
- Zarragoicoechea, G. J., Kuz, V. A., 2002, van der Waals equation of state for a fluid in a nanopore, Physical Review E 65, 021110.
- Zarragoicoechea, G. J., Kuz, V. A., 2004, Critical shift of a confined fluid in a nanopore. Fluid Phase Equilibrium 220, 7-9.
- Zhang, T., Ellis, G. S., Ruppel, S. C., Milliken, K., Yang, R., 2012, Effect of organic-matter type and thermal maturity on methane adsorption in shale-gas systems. Organic Geochemistry 47, 120-131.
- Ziarani, A. S., Aguilera, R., 2012, Knudsen's permeability correction for tight porous media. Transp. Porous Med. 91, 239-260.
- Zilberbrand, M., 1997, A nonelectric mechanism of ion exclusion in thin water films in finely dispersed media. Journal of Colloid and Interface Science, 192, 471-474.
- Zimmerman, A. R., Chorover, J., Goyne, K. W., Brantley, S. L., 2004, Protection of mesoporous-adsorbed organic matter from enzymatic degradation. Environ. Sci. Technol. 38, 4542-4548.

### 3. NANOSTRUCTURAL CONTROL OF METHANE RELEASE IN KEROGEN

#### 3.1. Introduction

Sucessful gas production from shales in the United States in the last decade has initiated interest around the world (Boyer et. Al., 2011). Europe, Australia, and Africa are now starting to evaluate and explore their unconventional reservoirs. The reserves and economic feasibility of shale gas as an economic energy source depends on Estimated Ultimate Recoveries (EUR) based on the production history of current plays (Berman and Pittinger, 2011). The current production data generally indicate a steep decline in productivity over the first 3 years (i.e., the output of a typical well drops 80-90%) (King, 2010; Baihly et al., 2010; Hughes, 2013). This raises serious concerns about the long-term sustainability of shale gas production<sup>5</sup>. Maximizing the production rate and extending the wellbore life-time are important to the shale gas industry.

Another major concern of the shale gas revolution is that the use of a few years of production history to predict decades of commercial production may have overestimated productivity (Berman and Pittinger, 2011; Hughes, 2013; Inman, 2014). Among many other methods, a decline curve analysis is the most frequently used method for EUR estimation (Baihly et al., 2010; Lee and Sidle, 2010). Decline curve analysis is performed using the empirical Arps' equation (Arps, 1945):

$$q(t) = \frac{q_0}{[1+bD_0t]^{1/b}} \tag{3-1}$$

where q(t) and  $q_0$  are the gas production rates at time t and t = 0, respectively.  $D_0$  is the decline rate at t = 0 and b is the constant that controls the curvature of the decline trend. The selection of a wrong b value would have a tremendous impact on reserve estimation, particularly when b is too high (Ilk et al., 2008). In equation (3-1), if 0 < b < 1 the cumulative production is finite and if  $b \ge 1$  cumulative production is infinite, which is unreasonable (Lee and Sidle, 2010). However, many have reported that b > 1 yields the best fit to US shale production data (Baihly et al., 2010; Lee and Sidle, 2010; Rushing et al., 2007). For example, Baihly et al. (2010) reported b ranging from 0.637 to 1.694 for multiple shales. Because using b > 1 will tremendously increase EUR, many have warned that the use of a few years of historical production data to forecast the future of shale might be incorrect (Berman and Pittinger, 2011; Hughes, 2013; Mattar, 2008). Indeed, many found that, as more production data become available b tends to decrease (Baihly et al., 2010; Lee and Sidle, 2010; Rushing et al., 2007). Predicting and using the right b constant is therefore important in analyzing the future of shale production.

Shales are characterized with extremely low permeabilities (1–100 nanodarcy) and with the predominant presence of nanometer-sized pores (1 - 200 nm) (Wang, 2014). Whether a shale formation can be targeted for oil and gas exploration depends largely on the amount and type of organic content (King, 2010; Boyer et al., 2006; Passey et al., 2010). Usually, the higher the concentration of organic matter in rock, the better its source potential (Berman and Pittinger, 2011). Organic matter can adsorb gas and store significant amounts of free gas in its pores (e.g., Barnett Shale) (Wang and Reed, 2009). Data in the literature also suggests that clay minerals do not significantly contribute to methane sorption in organic-rich shale (e.g., Barnett, Haynesville) (Gasparik et al., 2014; Heller and Zoback, 2014). Under high pressure and temperature, organic matter is usually transformed into kerogen during sediment diagenesis (Boyer et al., 2006; Vandenbroucke and Largeau, 2007). Based on the atomic H/C and O/C ratios (i.e., van Krevelen diagram), kerogen is usually classified into three types (Vandenbroucke and Largeau, 2007). Type I (e.g., Green River kerogen) is primarily formed in lacustrine and sometimes marine environments. It is highly aliphatic with H/C > 1.5 and O/C from 0.03 to 0.1. Type II (e.g., Barnett kerogen) is typically formed in

deep marine environments. It is rich in hydrogen and low in carbon (H/C $\sim$ 1.3, O/C $\sim$ 0.15). Sulfur is also associated with this type of kerogen. Type III is derived from higher plant debris (e.g., coal). It has H/C < 0.8 and O/C from 0.03 to 0.3.

Horizontal drilling and hydraulic fracturing are two innovative techniques that enable commercial exploration of natural gas from impermeable shale formations (Howarth et al., 2011). The former enhances the extraction volume. The latter enhances shale permeability by creating a fracture network through an injection of a pressurized fluid into a wellbore. After a stimulation, gas is released from the shale matrix and migrates to the created fractures and then to a production wellbore. Because flow rates are usually high in the induced fractures, gas migration from the low permeability shale matrix into the fractures is the time-limiting step that controls production rate (Bailhly et al., 2010). Thus, understanding the gas extraction process from the nanopores is crucial to explaining the field-observed production decline.

In this work we performed molecular dynamics (MD) and Monte Carlo (MC) simulations using LAMMPS (Plimpton, 1995) to investigate methane adsorption to type II post-mature kerogen, methane extraction from nanopores, and the properties of methane in nanoporous kerogen. There are several advantages of our simulations compared to others. First, we used realistic kerogen models. Many used simple carbon porous material as a model for kerogen (Falk et al., 2015a; Firouzi et al., 2014; Falk et al., 2015b; Mosher et al., 2013). These simple models ignore chemical details, and, in some cases, the complexity and heterogeneity of the kerogen (e.g. by using a slit-shape pore). Thus, they cannot accurately capture the physical and chemical properties of complex kerogen (Cao et al., 2013; Klelemen et al., 2007). Second, we conducted extraction simulations under reservoir-relevant conditions. In our simulations, methane was withdrawn from the porous structure by defining an extracting region. When a molecule of gas flows into that region, it is withdrawn from the system by deletion. This allows us to study the flow of methane in porous materials as the gas pressure gradually decreases over time because of extraction. This also eliminates a serious problem encountered in other non-equilibrium MD simulations in which large, unrealistic forces are usually used to create flow (Ho et al., 2011; Lauga et al., 2007; Collell et al., 2015). Our results indicate that the extraction rate decreases rapidly in an early stage of extraction, in some sense, resembling field observations. Our work provides a microscopic view of methane extraction from a heterogeneous nanoporous kerogen matrix and may shed a light on our mechanistic understanding of the overall gas extraction process in the field.

#### 3.2. Methods

Formation of condensed kerogen: To create the condensed kerogen as shown in Figure 1B we conducted a series of MD simulations (Ungerer et al., 2015). Initially, we simulated 24 kerogen molecules in a box of 10x10x10 nm³ using NVT ensemble (1000K) for 100ps. During this simulation we collected one kerogen snapshot every 10ps. The 9 collected configurations were then compressed in NPT simulations in which the pressure was kept at 100 bar and temperature was gradually reduced to 900, 700, 500, and 300 K (100 ps for each temperature). At the last step, we reduced the pressure from 100 bar to 1 bar while keeping the temperature at 300K in the 100 ps NPT simulations. The final kerogen samples (9 samples) under room conditions were collected for characterization.

Adsorption isotherm of methane on kerogen: To calculate total uptake we conducted grand-canonical Monte Carlo simulations (GCMC). The principle of this method is that the gas in the kerogen is in equilibrium with the gas in an imaginary reservoir. One of the inputs for GCMC simulation is the methane chemical potential. The output from the GCMC simulations is the number of gas molecules in the kerogen as a function of the chemical potential. This output cannot be directly compared with experimental data because the chemical potential cannot be measured. Therefore, we performed "empty box" simulations (i.e., a box without kerogen) to establish the gas pressures at specific chemical potentials

(Greathouse et al., 2009). Other than that, one can use an equation of state to calculate the pressure of the gas that corresponds to a given chemical potential and vice versa (FrenKel and Smith, 2002).

Methane molecules were modeled using the united atom TRaPPE force field (Martin and Siepmann, 1998). Interactions between methane and kerogen atoms were described using a L-J potential with the cutoff distance of 12Å. Equilibrium was obtained when the number of methane molecules found in the kerogen sample reached a constant value. This number describes the total uptake. The excess adsorption was estimated using the following equation:  $n_{excess} = n_{total} - \rho_{P,T} V_{free}$ , where  $n_{excess}$  and  $n_{total}$  are the excess adsorption and total uptake, respectively, and  $\rho_{P,T}$  is the density of methane calculated using the Peng-Robinson equation of state (Reid et al., 1987) at a specific temperature and pressure.  $V_{free}$  is the pore volume in kerogen determined by conducting GCMC simulations for non-adsorbed He (Peng et al., 2011) at a low pressure and temperature.

Extraction of methane from micropore in kerogen: To extract the methane from the kerogen we conducted MD simulations in the NVT ensemble (T=338K) starting from the configuration obtained from GCMC simulations at gas pressure of 262 atm, combined with the "fix evaporate" procedure available in the special package MISC of LAMMPS (Cheng et al., 2011). When the "fix evaporate" procedure is used, it is required to calculate the temperature of system using the number of atoms updated after each extraction event. For the evaporate procedure, we defined a spherical region of radius 3Å within a kerogen pore. When methane molecules move into this region, they are deleted or removed from the system. We preset the maximum deletion rate at 5 molecules for every 500 time steps (i.e., 0.5 ps). Our reported extraction rates depend on the number of methane molecules that move into the defined region during a 0.5 ps timeframe and are always smaller than our preset maximum deletion rate. To evaluate the impact of the size of our extraction sphere, we performed an additional simulation using a sphere with a 5Å radius. We found that the difference in the extraction rate profiles for the 3Å and 5Å spheres is insignificant. In addition, because all the molecules moving into the extraction region are withdrawn, the region is effectively a vacuum. Thus, our simulation setup is analogous to the constant pressure (bottom hole pressure) constraint used for field production.

The number of methane molecules remaining in kerogen was recorded as a function of time to calculate the extraction rate and monitor the gas pressure. In general, it is very difficult to calculate the gas pressure in the narrow space. We estimated gas pressure by combining the results obtained from the extraction simulation and GCMC simulation. In particular, in the extraction simulation we recorded the number of gas remaining inside kerogen as a function of time. In the GCMC simulation, we obtained the number of gas inside kerogen as a function of pressure. By combining these data, we infer the pressure as a function of time in the extraction simulation as reported in the section below.

#### 3.3. Results

#### Model construction of kerogen

The kerogen model (Figure 3-1A) used in our work was developed by Ungerer et al. (2015) to reproduce the elemental and functional analysis data of kerogen by Kelemen et al. (2007). It is representative of over-mature kerogen (Type II-D) found in the Duvernay organic-rich marine shale formation and similar to that found in Barnett shale. In the work of Collell et al. (2015), Ungerer et al. (2015) and Collell et al., 2014), the kerogen molecule was modeled by implementing the PCFF+ force field (Ungerer et al., 2014), which describes atomic dispersion-repulsion interactions using the Lennard Jones 6-9 potential. This makes it difficult to simulate kerogen with other constituents (e.g., water, clays, CO<sub>2</sub>, hydrocarbon) which are often simulated using force fields that implement the Lennard Jones 6-12 potential to describe atomic dispersion and repulsion. In our simulations, kerogen was simulated using the CVFF force field (Hagler et

al., 1979). As we show below the condensed kerogen density, pore size distribution, and methane adsorption isotherm are not only comparable with those obtained for kerogen modeled by using the PCFF+ force field but also with experimental results.

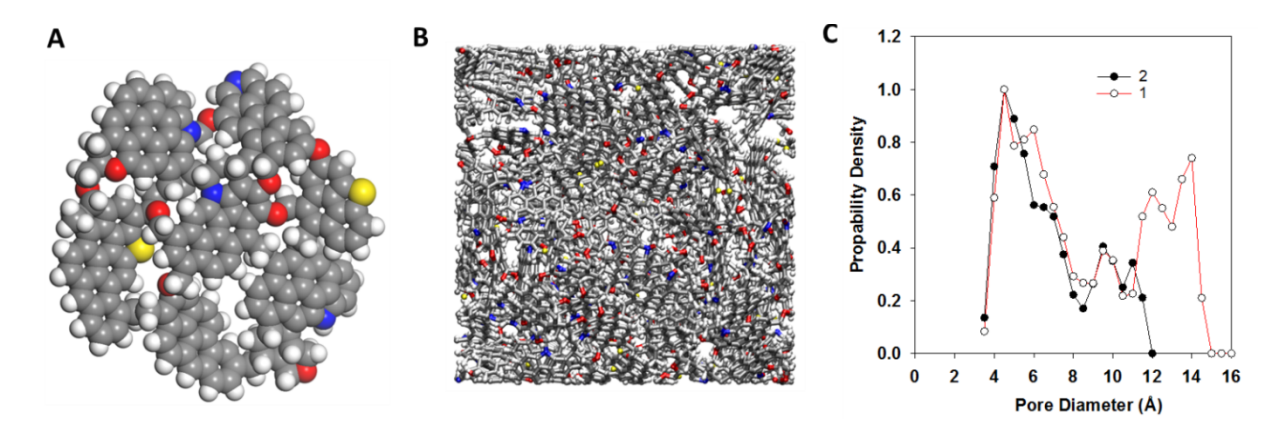


**Figure 3-1.** Post-mature kerogen molecule used in our simulations **(A).** Red, blue, yellow, grey, and white spheres represent oxygen, nitrogen, sulfur, carbon, and hydrogen atoms, respectively. A representative condensed kerogen sample at ambient conditions obtained by conducting a series of MD simulations as described in the Methods section **(B).** Pore size distributions of two extreme kerogen samples collected in MD simulations: 1 (red) and 2 (back) **(C).** 

Condensed kerogen (Figure 3-1B) was created by conducting a series of MD simulations as described in the Methods section. At ambient conditions, the density of our kerogen model ranges from 1.172 g/cm<sup>3</sup> (Sample 1) to 1.287 g/cm<sup>3</sup> (Sample 2). These two samples serve as two bounding cases that we will use to report results in this paper. The other samples we studied fall between these two in terms of density, pore size distributions, and gas adsorption. The average density of kerogen calculated from the 9 collected samples is 1.22±0.04 g/cm<sup>3</sup>. This density is consistent with that determined using the PCFF+ force field (Ungerer et al., 2015). When comparing with experimental data, our calculated density is in good agreement with that reported by Stankiewicz et al. (2015) for the kerogen in the Duvernay shale (1.28±0.3 g/cm<sup>3</sup>).

In Figure 3-1C, we report the pore size distributions (PSD) of the two kerogen samples. The pore size distribution was calculated by applying the method proposed by Bhattacharya and Gubbins (2006) using an argon probe (PSD calculated using He probe is insignificantly different from PSD calculated using argon probe, data not shown for brevity). Pore size varies from 4 to 15Å for Sample 1 and from 4 to 12Å for Sample 2. The differences observed in the density and PSD of the different kerogen samples represent the heterogeneity of shale formations (Gasparik et al., 2014). The PSD indicates that only micropores (< 2 nm) (Sing et al., 1985) are observed in our models. Mesopores (2 – 50 nm) and macropores (> 50 nm) (Sing et al., 1985) are not present in our simulations due to limitations in our system size. Experimentally, PSD is studied using mercury porosimetry and low-pressure gas adsorption analyses. Because mercury porosimetry cannot detect micropores, our results need to be compared with those measured using gas adsorption techniques. Direct comparison between our calculated PSD and experimental data for isolated kerogen cannot be made because to our knowledge, this data is not available. However, comparison with experimental data for shale (i.e., including organic and inorganic matter) indicate that, except for the absence of mesopores and macropores, the PSD for the micropore size fraction is in good agreement with those found for the Barnett (Clarksin et al., 2013), Alum-Denmark (Rexer et al., 2013), and numerous

other shales in the United States such as the Haynesville, Marcellus, and Woodford (Chalmers et al., 2012).

#### Adsorption isotherm of methane on kerogen

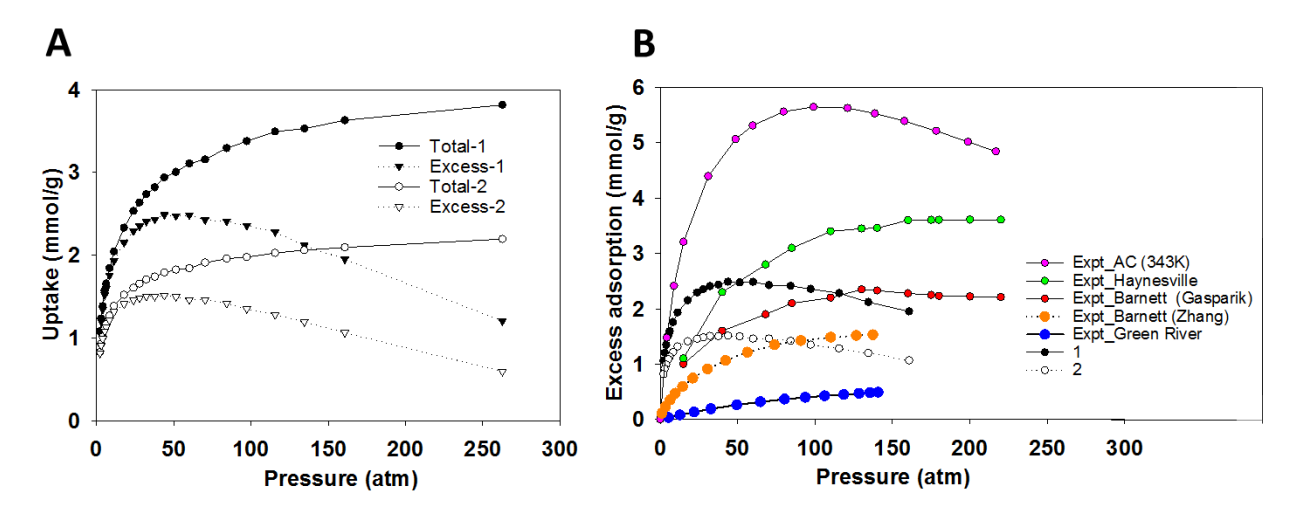


**Figure 3-2.** Total uptake (circles) and excess adsorption (triangles) of methane on kerogen samples 1 (black) and 2 (white) at 338K as a function of pressure **(A)**. Comparison of the excess adsorption for sample 1 (black circles) and 2 (white circles) with experimental results for activated carbon (purple circles), Haynesville shale (green circles), Barnett shale (red circles by Gasparik et al. (2014), and orange circles by Zhang et al. (2012), and Green Griver kerogen (blue circles) **(B)**. Green River kerogen is type I low thermal maturity kerogen. The excess adsorption data for the Barnett and Haynesville shales are measured for the whole shale (i.e., including organic and inorganic matter) and normalized by the total organic carbon. The comparison suggests that excess adsorption calculated for isolated kerogen can provide approximate values for methane adsorption in organic-rich shales.

In Figure 3-2A we present the total uptake and excess adsorption of methane obtained for the two bounding kerogen samples. To calculate total uptake (i.e., total amount of methane in simulation box) we conducted grand-canonical Monte Carlo (GCMC) simulations as described in the Methods. Excess adsorption is the difference between the total uptake and the amount of gas in the free volume in kerogen pores (see Methods). The results indicate that when pressure increases the total uptake increases rapidly at low pressure and slowly at high pressure. Comparison between total uptake and excess adsorption suggests that gas present in kerogen at low pressure is mainly adsorbed gas (i.e., the total uptake and the excess adsorption are the same). At high pressure, more gas fills into the free volume in the center of kerogen nanopores, resulting in a large difference between the total uptake and the excess adsorption. This observation is in good agreement with numerous simulations and experimental results for gas adsorption on metal organic frameworks (Fairen-Jimenez et al., 2012), carbon materials (Mosher et al., 2013), shale and coal (Ottiger et al., 2006; Bae and Bhatia, 2006).

In Figure 2B we compare our excess adsorption with experimental results from the literature such as data for Barnett (total organic carbon TOC=3.5%, VR=2.2%) and Haynesville (TOC=3.3%, VR=2.1%) shales by Gasparik et al. (2014), data for kerogen from Green River (VR=0.56) and organic-rich Barnett shale (TOC=6.6%, VR=2.01) by Zhang et al. (2012) Barnett and Haynesville are the two organic-rich shales that have similar maturity to our kerogen model and are within the dry gas generation window (Chalmers et al., 2012). These experimental data were measured for the whole shale (i.e., including organic and inorganic matter) and normalized by the TOC. Note that the experimental results for Barnett shales (red and orange circles) are from two groups (Gasparik et al., 2014 and Zhang et al., 2012). The fact that two

different samples from Barnett shales or two samples of similar TOC and VR (Barnett and Haynesville) exhibit different excess adsorption data demonstrates the diversity and heterogeneity of shales, consistent with our simulations (sample 1 and 2). Green River kerogen is type I kerogen with the vitrinite reflectance (VR) of 0.56% indicating low thermal maturity. The comparison indicates that the excess adsorption obtained for the simulated kerogen is higher than the measurement for Green River kerogen, probably due to the effect of thermal maturity (i.e., the Green River kerogen is less mature than the model kerogen). The comparisons also suggest that our excess adsorption data is of the same order of magnitude with actual measurements on Barnett and Haynesville shales. Thus, excess adsorption calculated for isolated kerogen can provide approximate values for methane excess adsorption in organic-rich shales. This is in a good agreement with the conclusion that organic matter plays a dominant role in gas adsorption in organic-rich shales. Other shale components such as clay minerals are reported to not contribute significantly to methane sorption in organic-rich shales (Gasparik et al., 2014). Heller and Zoback (2014) investigated methane sorption on pure illite, kaolinite, and activated carbon (a proxy for kerogen) and concluded that the amount of gas adsorbed on carbon is three orders of magnitude higher than that on clay minerals.

However, the comparison also illustrates a difference between our results and those measured on Barnett and Haynesville shales. While our excess adsorption data show a clear maximum at low pressure (0-50 atm), experimental data for shales do not exhibit a clear maximum. This difference could be attributed to several factors. First, the experimental data were measured for the whole shale and normalized by TOC. Inorganic matter might affect the pore size, the pore connectivity, and the interaction of methane with pores. Second, in the GCMC technique used to calculate our adsorption data, methane molecules can be inserted into isolated pores while in experiment methane can access only the connected pores. We also compared our excess adsorption with experimental results for methane onto activated carbon (Herbst and Harting, 2002), which is a proxy for kerogen (Heller and Zoback, 2014). Both our simulated results for kerogen and the experimental data for activated carbon (Herbst and Harting, 2002) exhibit a distinct maximum in excess adsorption, but methane excess adsorption in activated carbon is much higher. This difference raises questions regarding the use of porous carbon materials as surrogates for kerogen.

#### Extraction of methane from nanopores in kerogen

To study the flow of methane in complex kerogen structures we conducted an extraction simulation (Figure 3-3A) mimicking the field production where natural gas is withdrawn from a reservoir. In our simulation, methane is withdrawn from the porous structure by deleting the methane molecules that move into a defined region (large purple sphere) that represents a gas-free fracture tip (see Methods for more details). Because of the pressure gradient from the methane-filled kerogen to the extraction region, methane molecules in the kerogen pores diffuse into the extraction region if they are not trapped in isolated pores. This method allows us to study (i) the flow of methane in porous materials as the system pressure gradually decreases because of methane removal, (ii) the extraction rate as a function of time, (iii) the effect of adsorption, desorption, diffusion and nanoporous structure on the extraction rate. This method also eliminates one of the most serious troubles encountered in other non-equilibrium MD simulations in which large, unrealistic forces are usally used to induce flow (Ho et al., 2011; Lauga et al., 2007; Collell et al., 2015).

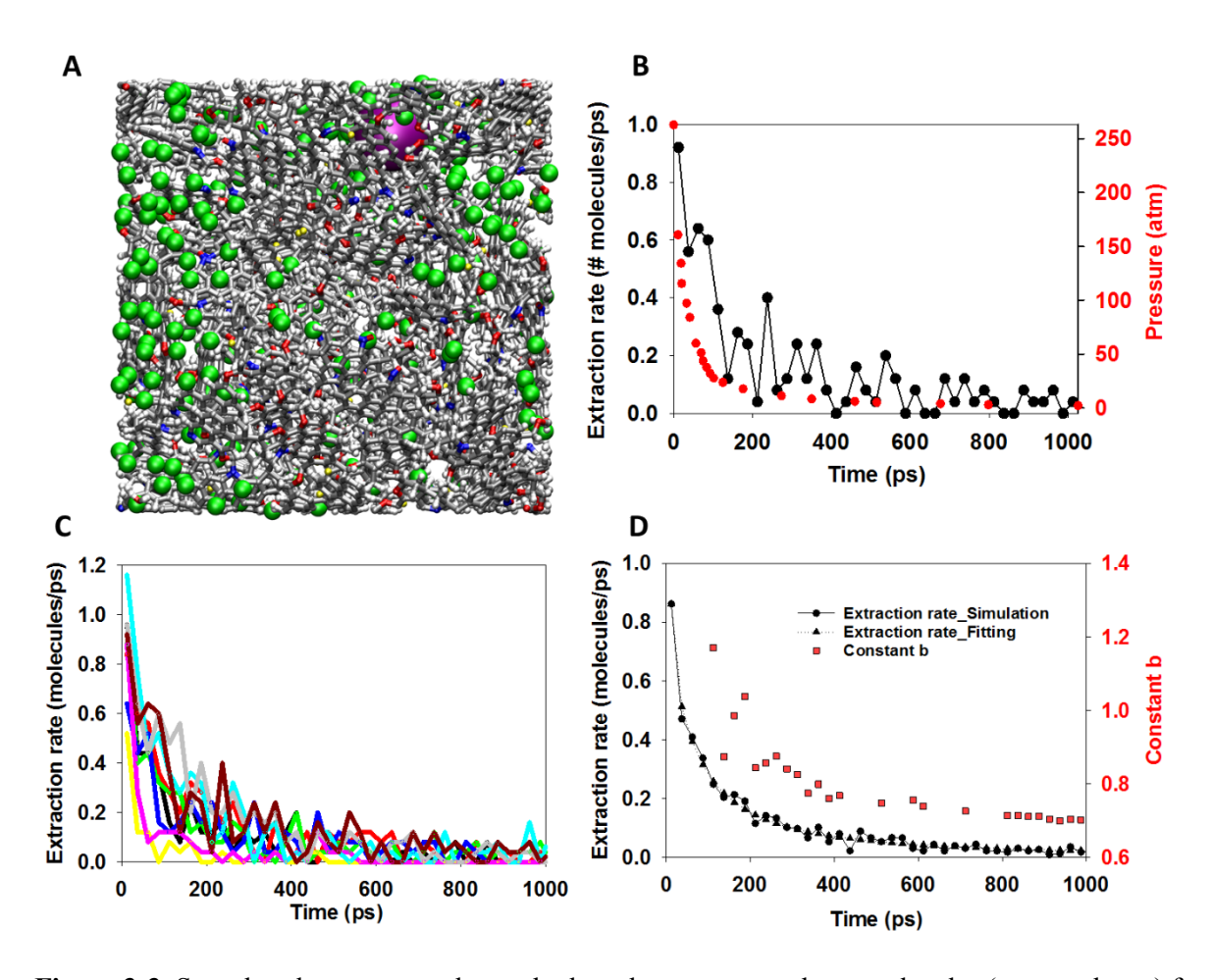


**Figure 3-3.** Snapshot demonstrates the method used to extract methane molecules (green spheres) from kerogen sample 1 **(A).** When methane molecule moves into a defined region (purple sphere) we extract it from the system by deleting that molecule. Extraction rate (black circles-left y axis) and pressure (red circles-right y axis) are plotted as a function of time during the extraction for sample 1 **(B).** Extraction rate calculated for 9 kerogen samples **(C).** Averaged extraction rate calculated from those obtained for 9 samples (black circles-left y axis) and fitted curve calculated using decline curve analysis (black triangles-left y axis) with b=0.7022 **(D).** Constant *b* obtained when fitting equation (3-1) with simulation data at different times (red squares-right y axis) (D).

In Figure 3-3C, we report the methane extraction rates for 9 kerogen samples as a function of time. The results indicate that the rate significantly decreases in a short period of time after initiating extraction. Figures 3B shows that we found a good correlation between the extraction rate and pressure of the system. The pressure also steeply decreases after initiating extraction. Afterwards, the pressure decreases slowly as a function of time. At the turning point (i.e., pressure ~17 atm), where the pressure and extraction rate start to decrease more slowly, 47 and 30% of methane were recovered from kerogen samples 1 and 2, respectively. After this point, both pressure and extraction rate decrease gradually. More methane is extracted until after 16 ns, 50% of the methane is recovered for sample 1 and after 26 ns, 35% of the methane is recovered for samples (1 and 2, respectively) that is trapped in isolated pores. These results indicate that the pores in sample 1 are better connected than those in sample 2 and that the ultimate recovery depends on network connectivity. If we exclude the methane in the isolated pores about 50% of the methane is recovered quickly and 50% is recovered more slowly.

The reason for the rapid decrease in extraction rate is shown in Figure 2A. As shown in the figure, the total uptake and excess adsorption curves (for both samples) start to separate from each other at the pressure of ~17atm, which is the turning point observed in the extraction rate and pressure curves in Figure 3-3B, suggesting that, at the early stage of extraction (i.e., at high pressures), the methane molecules withdrawn from kerogen are mainly present as pressurized free gas in the center of the nanopores. At pressures above ~17atm, where there is a significant difference between total uptake and excess adsorption (Figure 3-2A), the extraction rate and pressure drop significantly (Figures 3-3B and C). The main driving force for methane flow into the extraction region is the pressure gradient created by methane removal. At pressures below ~17atm, when the total uptake and excess adsorption are the same, there is little methane in the free volume. Beyond this point, most of the methane molecules extracted are adsorbed. The pressure gradient is no longer the main factor controlling methane migration. The extraction rate is much slower as it is determined by the desorption and diffusion rates.

#### Properties of methane confined in kerogen nanopores

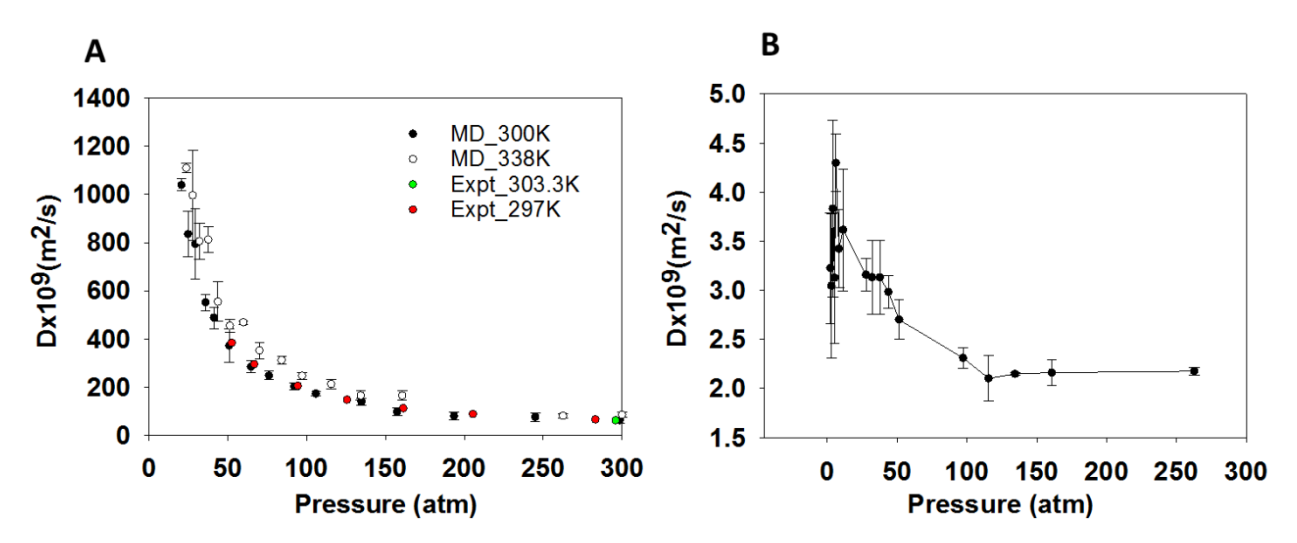


**Figure 3-4.** Self-diffusion coefficient D of bulk methane as a function of pressure **(A).** Self-diffusion coefficient of bulk methane was studied by conducting MD simulations for 300 methane molecules using NPT ensemble at the temperature of 300K (black circles) and 338K (white circles). The pressure ranges from 2 to 300 atm. The results at 300K are compared with experimental data (red and green circles). Self-diffusion coefficient of all methane (i.e., including free gas and adsorbed gas) inside kerogen sample 1 as a function of pressure during the extraction **(B).** This result was obtained by running MD simulations using NVT ensemble (338K) starting from the configurations at different pressures obtained during the extraction process as described in Figure 3A. All simulations were conducted for 40 ns. The last 30 ns trajectory was divided into 3 blocks of 10 ns each to calculate diffusion coefficient and error. Comparing with that of bulk methane, diffusion coefficient of all methane inside kerogen is much smaller (up to 3 orders of magnitude smaller), and furthermore it does not change significantly as a function of pressure.

It is known that chemical species confined in nanopores can behave significantly differently from that in a bulk system (Wang, 2014). In Figure 3-4 we compare the dynamic properties of bulk methane with methane confined in kerogen. In Figure 4A we report the self-diffusion coefficient (D) of bulk methane as a function of pressure at 300K and 338K. The results at 300K are compared with experimental data around 300K (Helbaek et al., 1996; Dawson et al., 1970). The comparison illustrates excellent agreement between computational and experimental results. Our results also indicate that the self-diffusion

coefficient of bulk methane exponentially decreases up to two orders of magnitude when the pressure increases from 20 to 300 atm.

In Figure 3-4B, we show the diffusion coefficient of all methane (i.e., including free gas and adsorbed gas) confined in kerogen sample 1 at different pressures. We observed that the diffusion coefficient of methane in kerogen sample 1 is higher than that of methane in sample 2. This observation agrees with the previous conclusion that pores in sample 1 are better connected than those found in sample 2. Compared with bulk methane reported in Figure 3-4A, the methane inside kerogen diffuses much more slowly (up to 3 and 5 orders of magnitude slower for sample 1 and 2, respectively). Our results also indicate that the diffusion coefficient of methane inside kerogen does not change significantly during extraction (i.e., as pressure decreases), in a striking contrast to bulk methane. This suggests that nano-confinement, adsorption, and pore connectivity play key roles in determining methane extraction rates. As the diffusion of methane in kerogen is always slow, the movement of methane into the extraction region at high pressure as discussed in Figure 3-3 is governed by the pressure drop. The diffusion plays a small role at high pressures at which the number of methane molecules present as free gas is abundant. However, at low pressure there is little free gas, the governing factor is either diffusion or desorption. After the turning point shown in Figure 3B, there is still plenty of methane remaining in the connected pores in the kerogen samples, but the extraction rate is very slow.

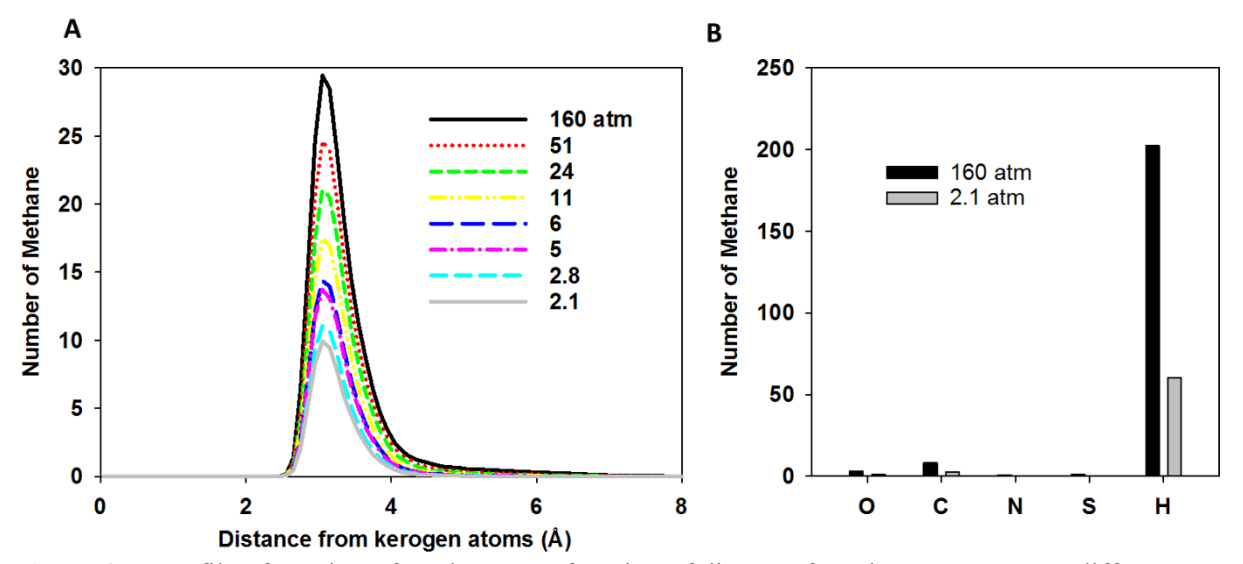


**Figure 3-5**. Profile of number of methane as a function of distance from kerogen atoms at different pressure **(A)**. Number of methane associated with specific kerogen atom at 160 atm (black) and 2.1 atm (grey) **(B)**. These data were calculated for sample 1.

In Figure 3-5A we report the profile of the number of methane molecules for sample 1 as a function of distance from kerogen atoms for a range of pressures. At high pressures, the peak of the profile is high and broad. At low pressures, the peak is low and narrow. The broad peak indicates that methane molecules are located both close to and far from the kerogen atoms, suggesting the existence of both adsorbed and free gas. As more gas is extracted, the number of free methane molecules decreases, and methane is mainly located near the kerogen atoms. At 2.1 atm, methane molecules concentrate only 2.5 to 4Å away from the kerogen atoms. The number of methane molecules associated with specific atom types in kerogen is shown in Figure 3-5B. The majority of methane molecules are located near the hydrogen atoms of kerogen.

#### 3.4. Discussion

In summary, using molecular simulations, we studied methane disposition and release in the nanoporous kerogen matrix. The simulations reveal two stages of methane release from kerogen nanopores, each with a distinct release mechanism. At the early stage of gas extraction, when the gas pressure is high, methane molecules withdrawn from the system are mainly pressurized free gas, and the migration of methane is driven by the gas pressure gradient. At the late stage, when the gas pressure is low, gas molecules extracted from the system are adsorbed gas. Methane desorption coupled with diffusion becomes the time-limiting step of the whole extraction process. At this stage, a significant amount of methane remains inside the nanopores in the kerogen, but the extraction rate is very small. The pore network connectivity can significantly affect the ultimate recovery. It is important to note that the change in gas pressure is the main factor driving the transition from the first stage to the second stage for gas extraction. The transition point of gas pressure is around 20 atm.

Two-stage methane release revealed from MD simulations has important implications to the analysis of long-term shale gas production. Our work indicates that the long-term production is expected to be determined by the second stage of gas release. As discussed above, the dominant mechanism for gas release at this stage is methane desorption and diffusion in kerogen nanopores. The long-term production thus highly depends on the gas adsorption/desorption isotherm (e.g., the adsorption capacity) and the nanopore structures (e.g., pore connectivity) of shale matrix. These properties must be taken into account in a long-term production analysis. Our work also implies that the historical production data from the early stage of gas extraction may not provide sufficient underlying information for the prediction of long-term wellbore production.

Our work may help to understand the b-factor issue related to production decline curve analyses using Equation (1) as discussed at the beginning of this paper. We used Equation (1) to fit the calculated gas extraction rate curve (Figure 3-3D). The averaged extraction rate was calculated over 9 samples as shown in Figure 3-3C. Fitting the averaged extraction rates at different times using equation (1) results in different b-factor values. Increasing the amount of historical data (i.e., increasing the total time interval) in the fitting leads to a decrease in the estimated b value. For instance, the b value deceases from  $\sim 1.2$  to  $\sim$ 0.7 when the fitting time interval increases from  $\sim$  110 ps to 1000 ps. The b value is not time-invariant. It must be made clear that, by no means, in this fitting analysis, we want to directly compare the calculated extraction rate curve with any actual field production decline curve because of their vast differences in both time and spatial scales and because of multiple maco-scale factors (e.g., micro-fracture networks) being excluded in our model. Nevertheless, this analysis raises a question about the validity of applying a single expression such as Equation (1) to a decline curve analysis over the entire time interval, because such a method may fail to capture the two-stage nature of the process. A reliable decline curve analysis calls for new model development based on mechanistic understanding of gas disposition and release in shale matrix. In addition, such mechanistic understanding may guide the development of new stimulation technologies for the extension of life cycle of a production well.

#### 3.5. References

- Arps, J. J. (1945) Analysis of Decline Curves. T Am I Min Met Eng 160, 228-247.
- Bae, J. S. & Bhatia, S. K. (2006) High-pressure adsorption of methane and carbon dioxide on coal. *Energ Fuel* **20**, 2599-2607.
- Baihly, J. D., Altman, R. M., Malpani, R. & Luo, F. (2010) Shale Gas Production Decline Trend Comparison over Time and Basins. *SPE-135555-MS* **135555**.
- Berman, A. & Pittinger, L. F. (2011) US shale gas: less abundance, higher cost. *The Oil Drum* http://nowandfutures.com/large/shale gas depletion(oildrum)8212.html.

- Bhattacharya, S. & Gubbins, K. E. (2006) Fast method for computing pore size distributions of model materials. *Langmuir* **22**, 7726-7731.
- Boyer, C., Clark, B., Jochen, V., Lewis, R. & Miller, C. K. (2011) Shale gas: A global resource *Oilfield Rev* 23, 28-39.
- Boyer, c., Kieschnick, J., Suarez-Rivera, R., Lewis, R. & Water, G. (2006) Producing Gas from Its Source *Oilfield Review* **18**, 36-49.
- Cao, X. Y. *et al.* (2013) Characterization of oil shale, isolated kerogen, and postpyrolysis residues using advanced C-13 solid-state nuclear magnetic resonance spectroscopy. *Aapg Bull* **97**, 421-436.
- Chalmers, G. R., Bustin, R. M. & Power, I. M. (2012) Characterization of gas shale pore systems by porosimetry, pycnometry, surface area, and field emission scanning electron microscopy/transmission electron microscopy image analyses: Examples from the Barnett, Woodford, Haynesville, Marcellus, and Doig units. *Aapg Bull* **96**, 1099-1119.
- Cheng, S. F., Lechman, J. B., Plimpton, S. J. & Grest, G. S. (2011) Evaporation of Lennard-Jones fluids. *Journal of Chemical Physics* **134**, 224704.
- Clarkson, C. R. *et al.* (2013) Pore structure characterization of North American shale gas reservoirs using USANS/SANS, gas adsorption, and mercury intrusion. *Fuel* **103**, 606-616.
- Collell, J. et al. (2015) Transport of Multicomponent Hydrocarbon Mixtures in Shale Organic Matter by Molecular Simulations. J Phys Chem C 119, 22587-22595.
- Collell, J. et al. (2014) Molecular Simulation of Bulk Organic Matter in Type II Shales in the Middle of the Oil Formation Window. Energ Fuel 28, 7457-7466.
- Dawson, R., Khoury, F. & Kobayash.R. (1970) Self-Diffusion Measurements in Methane by Pulsed Nuclear Magnetic Resonance. *Aiche J* **16**, 725-729.
- Fairen-Jimenez, D. *et al.* (2012) Understanding excess uptake maxima for hydrogen adsorption isotherms in frameworks with rht topology. *Chem Commun* **48**, 10496-10498.
- Falk, K., Coasne, B., Pellenq, R., Ulm, F. J. & Bocquet, L. (2015) Subcontinuum mass transport of condensed hydrocarbons in nanoporous media. *Nat Commun* **6**.
- Falk, K., Pellenq, R., Ulm, F. J. & Coasne, B. (2015) Effect of Chain Length and Pore Accessibility on Alkane Adsorption in Kerogen. *Energ Fuel* **29**, 7889-7896.
- Firouzi, M., Rupp, E. C., Liu, C. W. & Wilcox, J. (2014) Molecular simulation and experimental characterization of the nanoporous structures of coal and gas shale. *Int J Coal Geol* **121**, 123-128.
- FrenKel, D. & Smit, B. *Understanding molecular simulation from algorithms to applications*. (Academic Press, 2002).
- Gasparik, M. et al. (2014) Geological controls on the methane storage capacity in organic-rich shales. *Int J Coal Geol* 123, 34-51.
- Greathouse, J. A., Kinnibrugh, T. L. & Allendorf, M. D. (2009) Adsorption and Separation of Noble Gases by IRMOF-1: Grand Canonical Monte Carlo Simulations. *Ind Eng Chem Res* **48**, 3425-3431.
- Hagler, A. T., Lifson, S. & Dauber, P. (1979) Consistent Force-Field Studies of Inter-Molecular Forces in Hydrogen-Bonded Crystals .2. Benchmark for the Objective Comparison of Alternative Force-Fields. *Journal of the American Chemical Society* **101**, 5122-5130.
- Helbaek, M., Hafskjold, B., Dysthe, D. K. & Sorland, G. H. (1996) Self-diffusion coefficients of methane or ethane mixtures with hydrocarbons at high pressure by NMR. *J Chem Eng Data* **41**, 598-603.
- Heller, R. & Zoback, M. (2014) Adsorption of methane and carbon dioxide on gas shale and pure mineral samples. *Journal of Unconventional Oil and Gas Resources* **8**, 14-24.
- Herbst, A. & Harting, P. (2002) Thermodynamic description of excess isotherms in high-pressure adsorption of methane, argon and nitrogen. *Adsorption* **8**, 111-123.
- Ho, T. A., Papavassiliou, D. V., Lee, L. L. & Striolo, A. (2011) Liquid water can slip on a hydrophilic surface. *P Natl Acad Sci USA* **108**, 16170-16175.
- Howarth, R. W., Ingraffea, A. & Engelder, T. (2011) Natural gas: Should fracking stop? *Nature* **477**, 271-275.
- Hughes, J. D. (2013) A reality check on the shale revolution. *Nature* **494**, 307-308.

- Ilk, D., Rushing, J. A., Perego, A. D. & Blasingame, T. A. (2008) Exponential vs. Hyperbolic Decline in Tight Gas Sands: Understanding the Origin and Implications for Reserve Estimates Using Arps' Decline Curves. *SPE-135555-MS* **116731**.
- Inman, M. (2014) The Fracking Fallacy. Nature 516, 28-30.
- Kelemen, S. R. *et al.* (2007) Direct characterization of kerogen by x-ray and solid-state C-13 nuclear magnetic resonance methods. *Energ Fuel* **21**, 1548-1561.
- King, G. E. (2010) Thirty Years of Gas Shale Fracturing: What Have We Learned? *SPE-135555-MS* **133456**.
- Lauga, E., Brenner, M. P. & Stone, H. A. *Handbook of Experimental Fluid Dynamics*. 1219-1240 (Springer, 2007).
- Lee, W. J. & Sidle, R. (2010) Gas-Reserves Estimation in Resource Plays. SPE-135555-MS.
- Martin, M. G. & Siepmann, J. I. (1998) Transferable potentials for phase equilibria. 1. United-atom description of n-alkanes. *Journal of Physical Chemistry B* **102**, 2569-2577.
- Mattar, L. (2008) Production Analysis and Forecasting of Shale Gas Reservoirs: Case History-Based Approach. *SPE-135555-MS* **119897**.
- Mosher, K., He, J. J., Liu, Y. Y., Rupp, E. & Wilcox, J. (2013) Molecular simulation of methane adsorption in micro- and mesoporous carbons with applications to coal and gas shale systems. *Int J Coal Geol* **109**, 36-44.
- Ottiger, S. *et al.* (2006) Adsorption of pure carbon dioxide and methane on dry coal from the sulcis coal province (SW Sardinia, Italy). *Environmental Progress* **25**, 355-364.
- Passey, Q. R., Bohacs, K., Esch, W. L., Klimentidis, R. & Sinha, S. (2010) From Oil-Prone Source Rock to Gas-Producing Shale Reservoir Geologic and Petrophysical Characterization of Unconventional Shale Gas Reservoirs. *SPE-135555-MS* **131350**.
- Peng, X., Cheng, X. & Cao, D. P. (2011) Computer simulations for the adsorption and separation of CO2/CH4/H-2/N-2 gases by UMCM-1 and UMCM-2 metal organic frameworks. *J Mater Chem* **21**, 11259-11270.
- Plimpton, S. (1995) Fast Parallel Algorithms for Short-Range Molecular-Dynamics. *J Comput Phys* **117**, 1-19
- Reid, R. C., Prausnitz, J. M. & Poling, B. E. *The Properties of Gases and Liquids*. 4th edn, (McGraw-Hill, 1987).
- Rexer, T. F. T., Benham, M. J., Aplin, A. C. & Thomas, K. M. (2013) Methane Adsorption on Shale under Simulated Geological Temperature and Pressure Conditions. *Energ Fuel* **27**, 3099-3109.
- Rushing, J. A., Perego, A. D., Sullivan, R. & Blasingame, T. A. (2007) Estimating Reserves in Tight Gas Sands at HP/HT Reservoir Conditions: Use and Misuse of an Arps Decline Curve Methodology. *SPE-135555-MS* **109625**.
- Sing, K. S. W. et al. (1985) IUPAC recommendations. Pure and Applied Chemistry 57, 603-619.
- Stankiewicz, A., Ionkina, N., Motherwell, B., Bennett, B. W., O. & Mastelerz, M. Kerogen density revisited lessons from the Duvernay Shale. Paper presented at the Unconventional Resources Technology Conference, San Antonio, Texas. Society of Petroleum Engineers DOI:10.2118/178647-MS (2015).
- Ungerer, P., Collell, J. & Yiannourakou, M. (2015) Molecular Modeling of the Volumetric and Thermodynamic Properties of Kerogen: Influence of Organic Type and Maturity. *Energ Fuel* **29**, 91-105.
- Ungerer, P., Rigby, D., Leblanc, B. & Yiannourakou, M. (2014) Sensitivity of the aggregation behaviour of asphaltenes to molecular weight and structure using molecular dynamics. *Mol Simulat* **40**, 115-122.
- Vandenbroucke, M. & Largeau, C. (2007) Kerogen origin, evolution and structure. *Org Geochem* 38, 719-833
- Wang, F. P. & Reed, R. M. (2009) Pore Networks and Fluid Flow in Gas Shales. *SPE-135555-MS* **124253**.

- Wang, Y. F. (2014) Nanogeochemistry: Nanostructures, emergent properties and their control on geochemical reactions and mass transfers. *Chem Geol* **378**, 1-23.
- Zhang, T. W., Ellis, G. S., Ruppel, S. C., Milliken, K. & Yang, R. S. (2012) Effect of organic-matter type and thermal maturity on methane adsorption in shale-gas systems. *Org Geochem* 47, 120-131.

# 4. EFFECTS OF SURFACE HETEROGENEITIES ON NATURAL GAS STORAGE

#### 4.1. Introduction

Shale is a fine-grained sedimentary rock with low matrix permeability in the order of nano-darcy (Alexander Tom, et al., 2011). It has recently become an important natural gas resource. Natural gas containing shales are source rocks; namely, they have been responsible for the in-situ generation of the natural gas which has been the product of thermally- and biologically-driven chemical reactions that have taken place in the organic constituents of shale, also known as kerogen. Kerogen is an insoluble and porous organic material. Although pore size of kerogen may vary significantly, the average pore size is small and typically less than 10 nm (Kang, et al., 2011). Because of the nanoscale size of the pores in kerogen, numerous studies have recently been reported to understand the shale gas transport properties (Chen, et al., 2015), hydrocarbons accumulation (Diaz-Campos, 2014), nano-pore size dependence of fluid in phase behavior (Didar Behnaz and Yucel.), and pore size distribution (Adesida, et al., 2011) among others.

Various investigations have also been performed to understand, the chemical structure of kerogen. For the classical treatment of the problem and some insight on the organic matter maturation and kerogen composition, we recommend Chapter 4 from Tissot and Welte (1984). Kerogen is composed mainly of hydrogen and carbon and the amount of these atoms vary depending on the maturity of kerogen and the evolution of the organic matter. Nitrogen, sulfur and oxygen are also found in this hydrocarbon compound and the atomic percentage differs depending on the type of kerogen as well. Physical analysis, such as electron diffraction, show that kerogen is composed of stack of aromatic sheets, similar to a stack of graphene making up graphite (Tissot and Welte, 1984). Hence, investigators analyzing methanekerogen interactions often develop slit-like model pores consisting of two parallel sheets of graphite which is composed of several (typically, three) layers of graphene (Norman and Filinov, 1969; Tissot and Welte, 1984; Diaz-Campos, 2014). Graphene is an atomic sheet made of carbon hexagonal rings, shown in Figure 1a, and holds mysterious mechanical, thermal and electronic qualities which nowadays find many applications in physical sciences and various technologies. In (Norman and Filinov, 1969) the authors have identified in between the graphite layers methane that is confined and segregated into phases: adsorbed molecules right by the walls and free fluid molecules in the central portion of the space in between the layers, i.e., the slit-pores. They have also identified phase transition region in between the adsorbed and free molecules. The authors of the previous works reported that the adsorption of methane on graphite does not really depend on the thickness of the graphite wall, but it is really influenced by the surface area of the wall and the surface properties. However, it is unclear to what extend the surface chemistry influence the fluid-solid interactions.

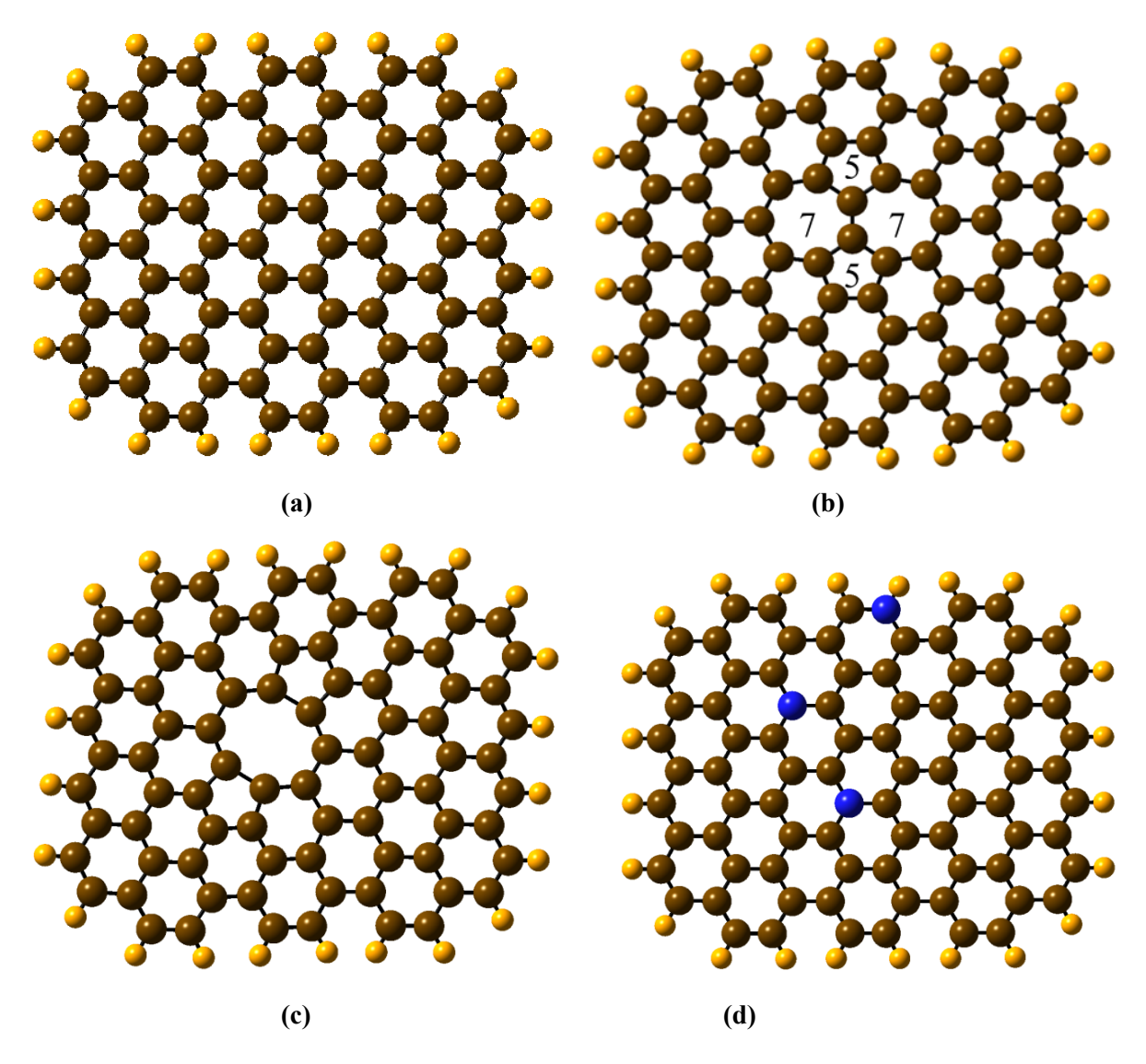


**Figure 4-1.** Organic surface models including pristine graphene and the graphene with heterogeneities. (a) pristine graphene, (b) Stone-Wales defect as two pentagons and two heptagons), (c) di-vacancy and (d) N-doping. These models are used in quantum mechanical simulations to calculate fluid-wall interaction parameters  $\varepsilon$  and  $\sigma$ , which are needed later on as input parameters during the Monte Carlo calculations in predicting the methane storage in model pores. Atom colors: carbon (brown), hydrogen (yellow), and nitrogen (blue).

In this report, we are interested in identifying the effects of various surface properties on methane adsorption. More specifically, the surface of the most inner graphene sheet will be modified by creating vacancies and by chemically doping it, see Figure 4-1. We are interested in quantifying to what extent the created surface heterogeneities and the structural defects play a role in methane storage in the slit-pore to gain insight into the potential impact of these surface effects on natural gas storage in kerogen. Methane interactions with the wall will be studied using quantum mechanics and the storage calculations will be performed using Grand Canonical Monte Carlo simulations.

The literature on the structural defects of graphene includes di-vacancies and Stone Wales defect. The latter has carbon atoms on the graphene sheet re-organized into two pentagons or two heptagons as illustrated in Figure 4-1b. And the former, are point defects in which two atoms are missing in two of the lattice sites of graphene and, in turn, create a small distortion in its structure, as is shown in Figure 4-1c. The most common kinds of defects found in graphene are vacancies that are produced by breaking the strong covalent bonds between carbons at an energy cost of about 7.8 eV. (Kaxiras and Pandey, 1988). Neek-Amal and Shayeganfar (2012) found that Van der Waals interactions between methane and pristine graphene sheet are due to addition of vacancies in the graphene sheet.

Doping is another graphene defect that takes place when a carbon atom is substituted by another atom such as nitrogen (N) (Figure 4-1d). The introduction of nitrogen atom into graphene has been effectively confirmed using X-Ray Photoelectron Microscopy (Shao, et al., 2010). Wang et al. reported that adsorption of methane on the graphene sheet is enhanced by the insertion of vacancies in the sheet and somewhat influenced by nitrogen doping (Wang Yin, et al., 2015).

#### 4.2. Methods

The nature of fluid-wall interactions is investigated using supercritical methane at  $176^{\circ}F$  (or 353.15K) temperature and at pressures above 637 psi (or 4.4 MPa) in a slit-shape model pore with graphite walls under the subsurface conditions. Gas storage in kerogen pores is composed by free gas, adsorbed gas, absorbed gas (the gas dissolved in the liquid hydrocarbon) therefore  $N_{total} = N_{free} + N_{adsorbed}$  (Didar Behnaz and Yucel, 2013). The adsorbed gas amount in the pore is often characterized using adsorption isotherm with the help of Grand Canonical Monte Carlo Calculations (GCMC) (Norman and Filinov, 1969). The first step, however, is to evaluate the interactions between methane and the graphite wall using quantum mechanics. In the evaluation process, we use Lenard-Jones (L-J) potential:

$$V_{LJ} = 4\varepsilon \left[ \left( \frac{\sigma}{r} \right)^{12} - \left( \frac{\sigma}{r} \right)^{6} \right] \tag{4-1}$$

where  $V_{LJ}$  is the potential energy, r is the distance between methane and the wall,  $\varepsilon$  and  $\sigma$  are the L-J parameters.  $\varepsilon$  is the minimum energy at an equilibrium distance where the attractive and repulsive energies are balanced and represents the strength of the interaction between methane and the carbon of the slit-pore wall.  $\sigma$  is the distance at which the potential energy is zero between methane and the wall. Optimum values for these parameters can be estimated using quantum mechanical simulations with the help of the Gaussian 09 program (M. J. Frisch) using the MP2 method which uses 6-31(g) basis-set (Ditchfie.R, et al., 1971). In these simulations methane and organic wall models (e.g., pristine graphene and graphene with structural defects) are geometrically optimized until they reach energy minima. In the geometry optimization Gaussian uses Berny algorithm which calculates the potential energy and the wave function (probability of finding an electron at given space) of an initial geometry. This procedure is repeated until the algorithm finds a stationary point of the energy where the forces (first derivative of the energy with respect to position) of each atom are zero. Next, several self-consistent calculations of the potential energy ( $V_{LJ}$ ) is performed between methane molecule and the organic wall model at varying distance (r) values from 3.8 Å to 10 Å.

The quantum mechanical simulation and potential energy calculations allow us extract L-J parameters that are needed as input information for the GCMC calculations in which the chemical potential, volume and temperature are kept constant (µVT). During GCMC simulations, methane is simulated as a spherical site using TraPPE-UA force field (Martin and Siepmann, 1998), the pore model is simulated as a computational box with two parallel graphite walls that are represented by Steele Wall potential (Steele, 1973) using Towhee software (Martin, 2013). The box is periodic in the x and y directions and fixed to a

desired size in the z direction where walls are placed. The slit-pore space is filled with methane molecules, GCMC models the bulk fluid that is in equilibrium by inserting, deleting and displacing molecules. Temperature is 353.15 K and the volume have dimensions of 7.73 nm×7.73 nm in the x and y directions. The pore dimension is increased in the z-direction from 3 to 5nm.

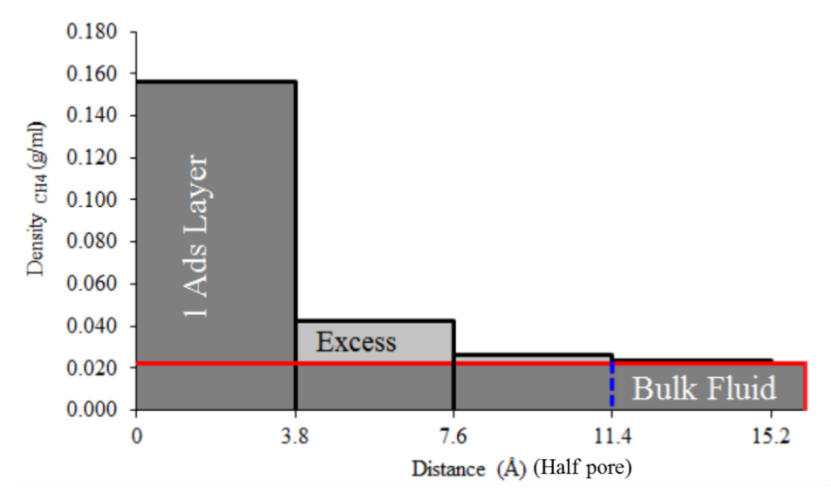


**Figure 4-2.** Isothermal density profile of methane sandwiched in between two graphite walls with a separation distance of 4nm at 580 psi. The estimated density is based on GCMC calculations. The first column is the adsorbed layer, the light gray columns are the excess amount of methane due to wall interactions and the last column on the right is the bulk fluid that represents the free gas. Red line is the methane bulk density predicted using NIST.

The chemical potential necessary for a GCMC simulation is estimated using Isobaric-Isothermal Ensemble (NPT) simulation which involves a computational box that has fixed volume and contains bulk methane, i.e., in the absence of pore walls. During NPT simulation the pressure is fixed to a value in between 500 psi to 12000 psi (McDonald, 2002). The total number of molecules (N) and the pore temperature (T) are maintained constant. The surface structure of the pore considered is modified by inserting the estimated L-J parameters ( $\varepsilon$  and  $\sigma$ ) from the quantum mechanics calculations into the GCMC simulation. At the end of every GCMC simulation, density profiles, Langmuir isotherms and excess of adsorption curves of a slit-shaped pore are calculated. The methane mass density ( $\rho_{calc-CH4}$ ) within the slit-pore for every simulation is calculated using the following equation (Ambrose, et al., 2012):

$$\rho_{calc-CH4} = \frac{\rho_{number} M_{CH_4}}{N_A} \tag{4-2}$$

where  $N_A$  is the Avogadro number,  $M_{CH4}$  is the molecular weight of methane,  $\rho_{number}$  is the number density (number of molecules per volume) of methane. Figure 4-2 displays a typical isothermal density histogram where adsorbed layer and excess of adsorption can be observed.

If the distribution of methane in the pore is characterized using a storage model such as Langmuir, based on the mono-layer assumption, one would take into account the molecules in the first layer as the adsorbed amount. Based on the adsorption theory on flat surface and in pores, the adsorbed methane rises

linearly at low pressure and reaches saturation at high pressure. Hence, a nonlinear methane adsorption isotherm is expected.

Excess amount of adsorption, on the other hand, can be calculated using:

$$n_{excess} = \frac{\left[\sum_{i=2}^{N} (\rho_{calc-CH4} - \rho_{bulk-CH4}) V_{3.8}\right] * N_{A}}{M_{CH_{4}}} \tag{4-3}$$

where  $n_{excess}$  is the mass of excess methane molecules,  $\rho_{bulk}$  is the mass bulk density of methane from NIST, standards and Technology (NIST, 2011),  $V_{3.8}$  is a volume segment within the slit-pore. Each segment has size in the z direction is 3.8 Å which correspond to the diameter of methane molecules.

#### 4.3. Results

#### **Chemical Potential of Bulk Methane**

Figure 4-3 shows the computed chemical potential of pure methane versus pressure. The form of the predicted curve follows the regular shape for simple gases. The chemical potential increases as the pressure increases; at low pressures, the activity (chemical potential) of CH<sub>4</sub> molecules are significantly influenced by the pressure; however, at higher pressures, the dependence is somewhat less influenced making the slope of the curve decline and becomes constant. The chemical potential value at a particular fluid pressure is used as input for the GCMC calculations.

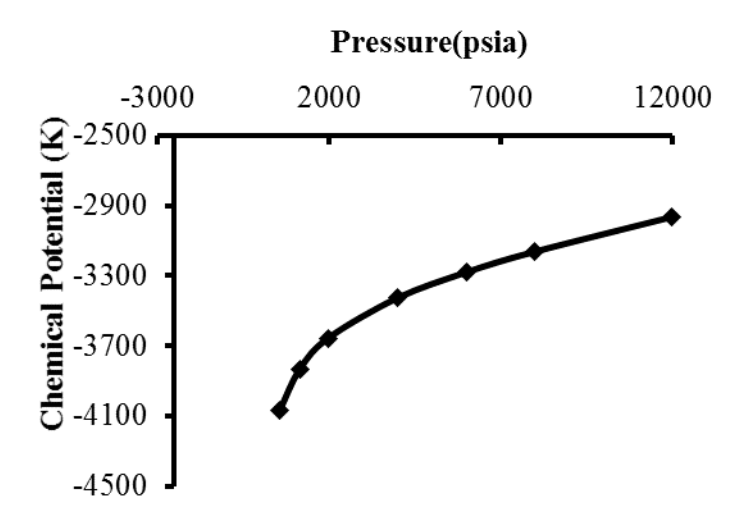


**Figure 4-3.** Chemical potential dependence of methane with varying fluid pressure. The effect of nanopore confinement on the adsorption

In order to understand the effect of nanopore confinement on the methane adsorption, we used model slitpores with pristine walls (in the absence of defects and heterogeneities) and numerically predicted the methane adsorption isotherm and the excess methane amounts. The thicknesses of the pores are varied as 2nm, 4nm, and 5nm. Note that the adsorbed amount is based on the accumulated molecules within the first layer by the wall, whereas the excess amounts are based on the amounts within the inner segments. As shown in Figure 4-4, no variation exists in the adsorbed amount as the size of the pore is reduced from 5 nm to 2 nm. This indicates that the confinement does not influence the packing of the molecules by the walls. In addition, the results implicitly show that the total surface area of the walls available for adsorption are maintain the same for each pore.

The estimated excess amount, on the other hand, is shown in Figure 4-5. The excess amount is significantly influenced by the fluid (or pore) pressure. There exists a range of pressure in between 1,000 psi to 5,000 psi where the excess amount is comparatively quite high. Clearly the confinement plays a significant role in methane storage under the subsurface conditions. At the extreme conditions of pressure, the excess contribution is relatively less. Note that no significant variation due to nano-pore size is observed in the excess amount since the fluid behavior is quite similar in pores with size in between 2-5nm.

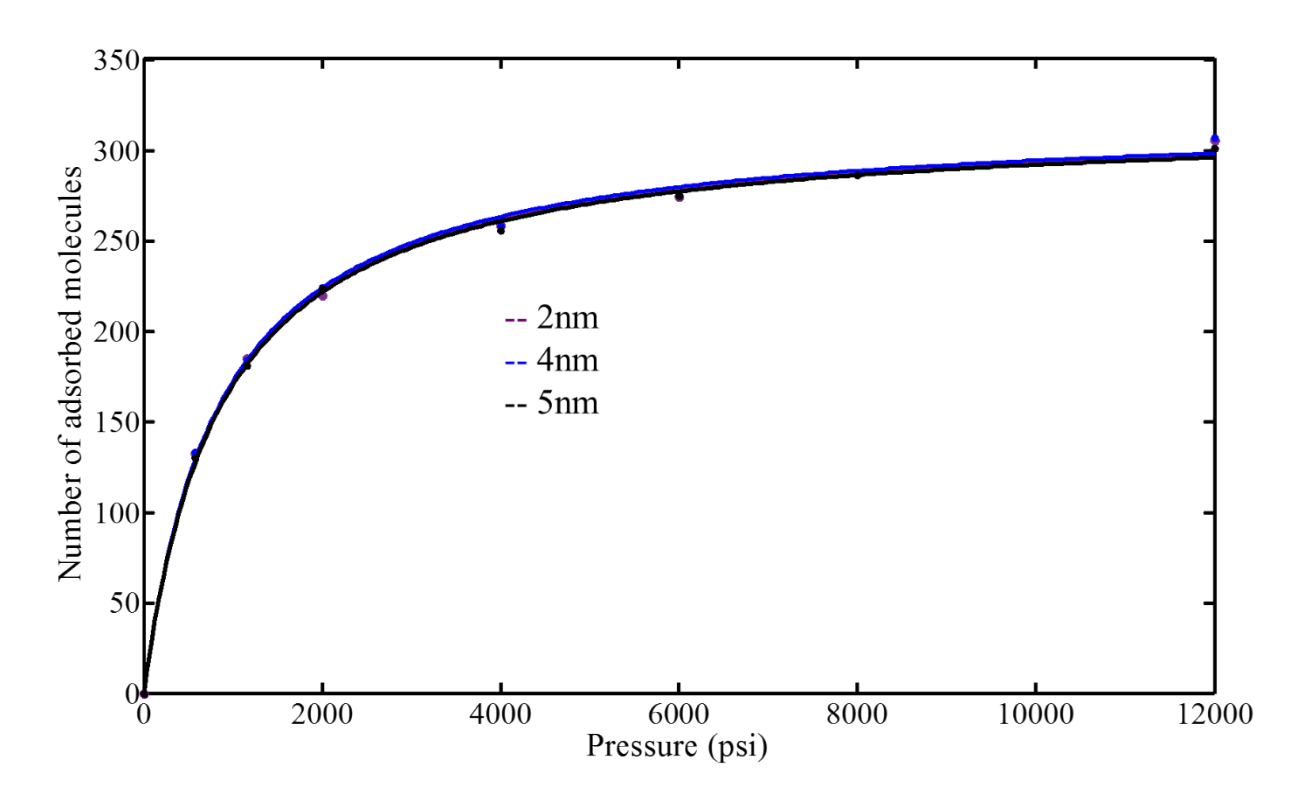


**Figure 4-4.** Langmuir adsorption isotherms for methane in a slit-shape pore with sizes 2, 4 and 5nm. The pore walls are made of pristine graphene, i.e., no surface heterogeneities.

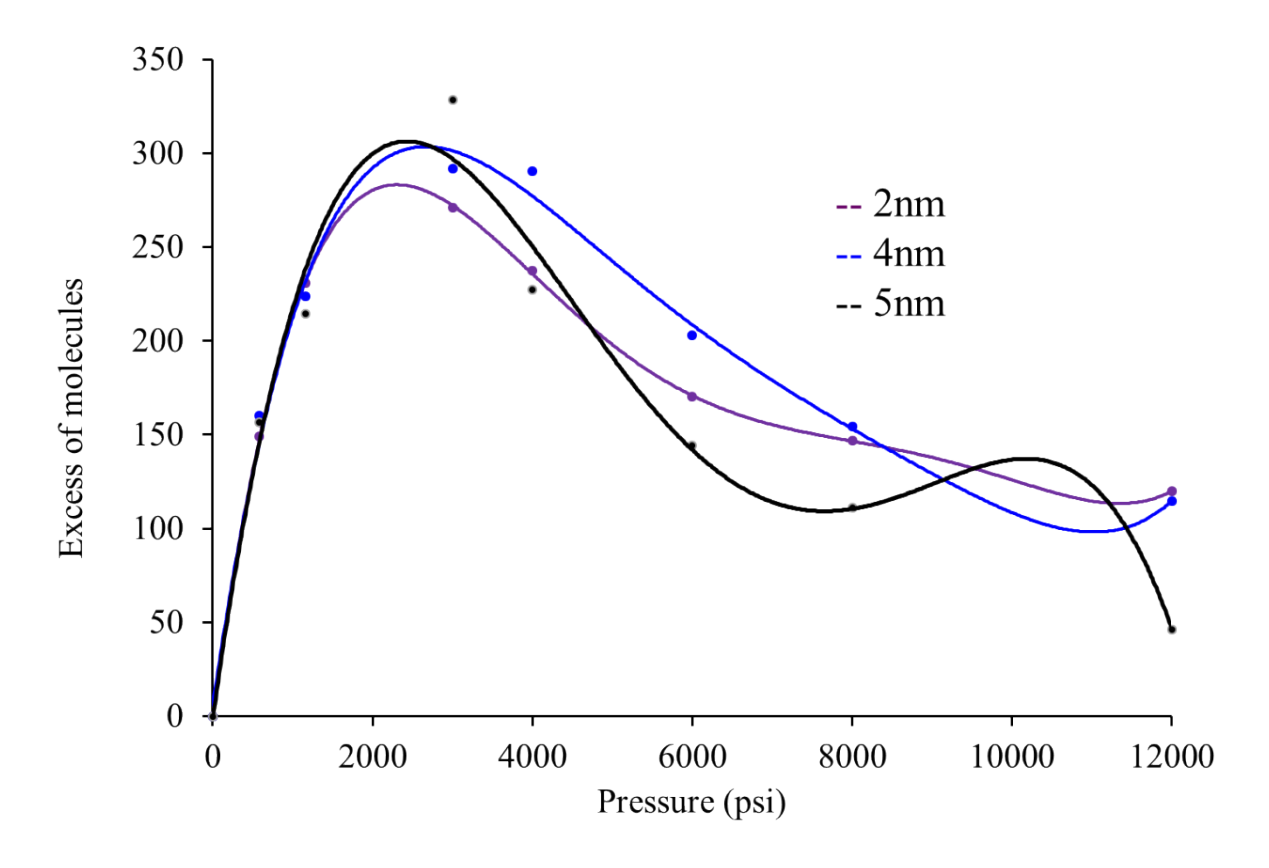


**Figure 4-5.** Excess amount of methane in slit-shape nanopores with varying sizes.

#### **Isothermal Density Histogram**

Figure 4-6 shows the isothermal density profile of methane across the width of a 4nm slit-shape pore with pristine graphene walls. The simulations show that the density of methane is not uniform but has a structure across the pore. Methane molecules are adsorbed on the graphene surface forming an adsorbed layer and then a staircase structure appears involving several layers of methane molecules as the center of the pore is approached. This observation has been reported before in other studies, see for example (Ambrose, et al., 2012). Adsorbed methane on the pore wall is observed from 0 to 3.8 Å, i.e., the first layer of methane, where methane molecules are under the strong influence of the van der Waals forces imposed by the wall and therefore the methane density is the highest in this first layer. The high density near the wall is high because the attractive forces between the wall and methane are much greater in magnitude than the attractive forces between the methane-methane molecules. The attractive forces become less as the methane molecules are located further away from the wall, thereby the methane density decreases as the distance of gas molecules increases with respect to the wall. There are two walls in a slit-shaped pore and thus the density decreases until the pore half-length and then increases symmetrically until it reaches the second wall. This symmetric picture is shown for the methane density profiles at different pore pressures in Figure 4-4. Also note that the density of the first adsorption layer increases linearly at moderate pressures, and is unfluctuating at high pressure due that the surface reaches saturation. In addition, the density matches the bulk value for 4nm in the center of the pore and this is called the free gas in the pore (Didar Behnaz and Yucel, 2013).

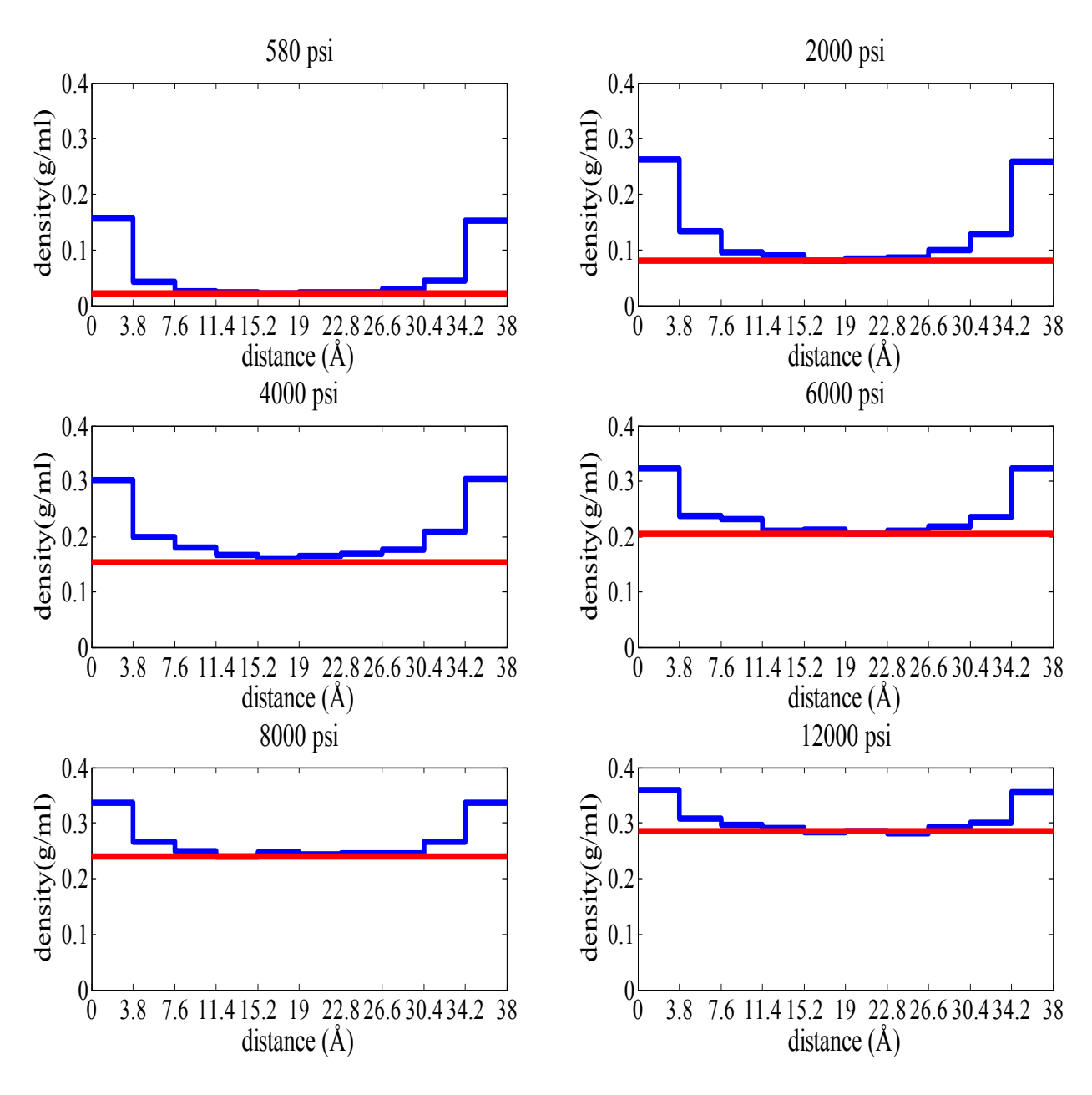


**Figure 4-6.** Density profile of methane across a 4nm slit pore with pristine walls at 353K. The pore pressure is varied at 580 psi, 2,000psi, 4000 psi, 6000 psi, 8000 psi, and 12,000 psi. The density of methane is not constant in the pore and has a distinct profile. Its value is higher near the wall (first layer) and drops to the free fluid density at the center of the pore. The red line is the bulk fluid density value as obtained from NIST (2011). Clearly, the calculated density in the middle of the pore matches the free gas values.

#### Methane- graphene wall interactions in the presence of surface heterogeneities

Interactions between methane and graphene walls with varying surface properties are assessed next through the potential energy functions as displayed in Figure 4-7. These energy functions are based on the quantum calculations and represent the interplay between the repulsive and attractive energies between

methane and the wall molecules. From these curves parameters  $\sigma$  and  $\epsilon$  are calculated for various solid surfaces: pristine graphene, Nitrogen-doped graphene and graphene with vacancies, i.e., di-vacancy and Stone-Wales. The estimated parameter values are given in Table 4-1. The level of variability in the interactions can be seen through the estimated  $\epsilon$  values in Table 1.  $\epsilon$  slightly varies in the range of 44 K to 49.2 K with the heterogeneities. Consequently, it is found that the impact of surface heterogeneities are not significant on the predicted potential energy function.

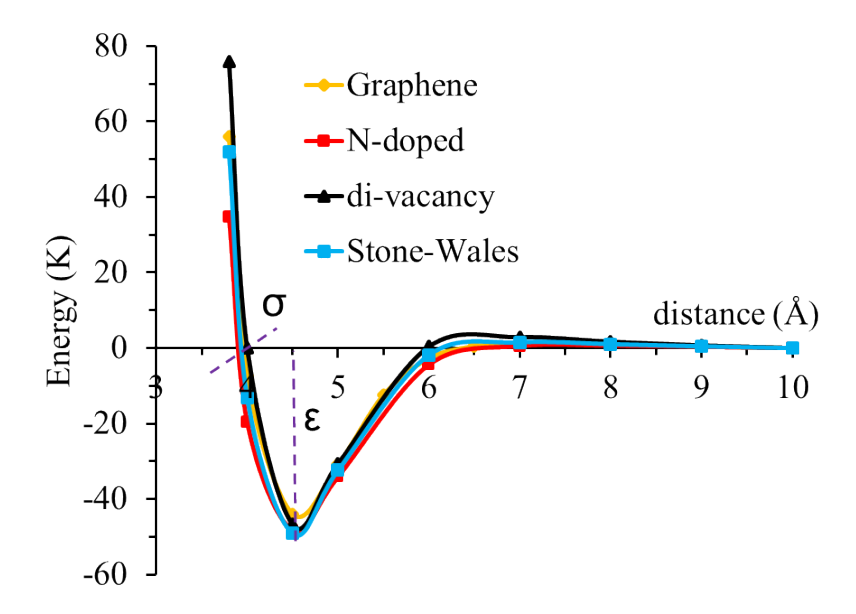


**Figure 4-7.** Lenard-Jones potential energy for the interaction between methane and varying wall properties graphene, N-doped, di-vacancy and Stone-Wales.

**Table 4-1.** Lenard-Jones parameters of methane-organic wall interactions in the presence of the heterogeneities. The epsilon parameter slightly varies with the heterogeneities on the surface.

| Model       | ε(Κ)   | σ(nm) |
|-------------|--------|-------|
| Graphene*   | -44.00 | 0.395 |
| di-vacancy  | -46.78 | 0.400 |
| N-doped     | -48.32 | 0.390 |
| Stone-wales | -49.18 | 0.392 |

In large pores, since the adsorbed amount of methane is independent of the variation of the pore width and primarily dependent on the graphite surface area, in this section of the report we decided to fix the pore width to 4nm and focus on the effects of the surface heterogeneities. The surface area is also fixed. The calculated adsorption isotherms and the excess amounts changing with surface heterogeneities are shown in Figure 4-8 and Figure 4-9, respectively. There is no significant variation in the isotherms and the excess amounts when heterogeneities are present on the surface of graphene. This is due to weak physical interaction of methane and the walls, as described by Lenard-Jones potential.

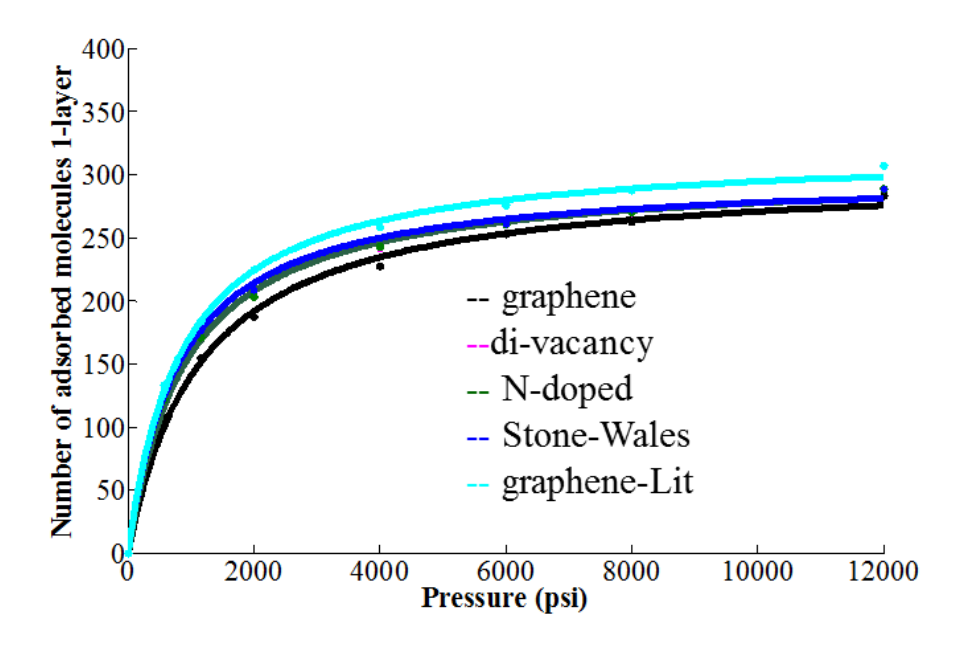
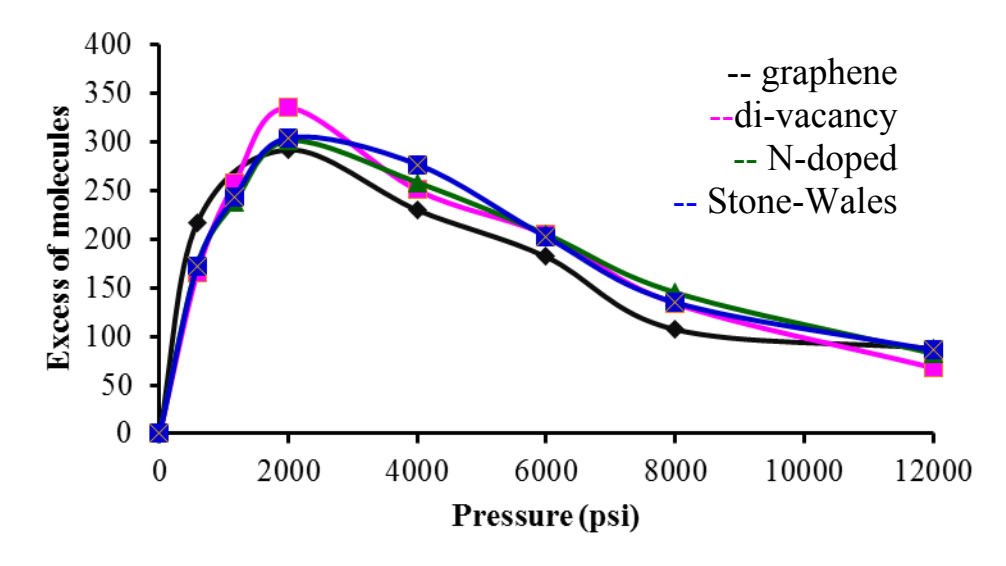
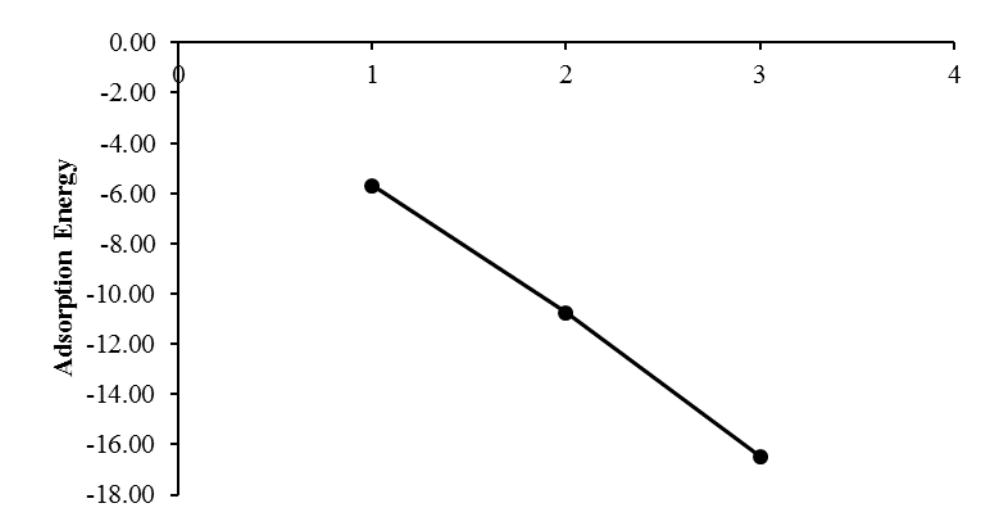


Figure 4-8. Adsorption isotherms for methane in 4nm graphene pore with heterogeneities on the surface.



**Figure 4-9.** Excess adsorption of methane in slit-pore with surface heterogeneities. The excess amount calculations exclude the first layer of adsorption by the walls.



**Figure 4-10.** Calculated adsorption energies for methane-graphene wall interactions with changing number of nitrogen atoms on the surface.

#### N-doping effect on Methane- graphene wall interactions

Among the heterogeneities investigated, Nitrogen-doping is found to be the most influential on the fluid-solid interactions. This effect becomes more pronounced when the number of nitrogen atoms available at the surface is increased. Figure 10 shows that the level of methane-wall interactions is reduced by a factor of 3 when the number of doped Nitrogen is increased from one to three. In essence the effect of increased level of N-doping is found to be significant on methane adsorption. The more nitrogen there is the less adsorption is experienced.

#### 4.4. Conclusion

The adsorption of methane in slit-shaped pores is sensitive to the surface area available for adsorption but independent of the size of the pore. The excess amount to due to confinement effect is most pronounced under the subsurface conditions where the pressure is in the range of 1,000-5,000 psi. The surface heterogeneities have the potential to impact methane adsorption depending on the level of heterogeneities. For example, N-doping influence on the fluid storage is more pronounced when the level of doping is increased. Consequently, the fluid storage is dominantly based on the availability of the free fluid.

#### 4.5. References

Adesida, A., Akkutlu, I. Y., Resasco, D. E. & Rai, C. S. (2011) Kerogen Pore Size Distribution of Barnett Shale using DFT Analysis and Monte Carlo Simulations. *SPE*.

Alexander Tom et al. (2011) Shale Gas Revolution. Oilfield Review Autumn, 40-55.

Ambrose, R. J., Hartman, R. C., Diaz-Campos, M., Akkutlu, I. Y. & Sondergeld, C. H. (2012) Shale Gas-in-Place Calculations Part I: New Pore-Scale Considerations. *Spe Journal* 17, 219-229.

Chen, L. *et al.* (2015) Nanoscale simulation of shale transport properties using the lattice Boltzmann method: permeability and diffusivity. *Scientific Reports* **5**.

Diaz-Campos, M. (2014) A Novel Approach for Reservoir Simulation and Fluid Characterization of Unconventional Fields: Phase 1 Molecular Level Considerations. *SPE*.

- Didar Behnaz & Yucel., A. I. (2013) Pore-size Dependence of Fluid Phase Behavior and Properties in Organic-Rich Shale Reservoirs. *SPE*.
- Ditchfie.R, Hehre, W. J. & Pople, J. A. (1971) Self-Consistent Molecular-Orbital Methods .9. Extended Gaussian-Type Basis for Molecular-Orbital Studies of Organic Molecules. *Journal of Chemical Physics* **54**, 724-&.
- Kang, S. M., Fathi, E., Ambrose, R. J., Akkutlu, I. Y. & Sigal, R. F. (2011) Carbon Dioxide Storage Capacity of Organic-Rich Shales. *Spe Journal* **16**, 842-855.
- Kaxiras, E. & Pandey, K. C. (1988) Energetics of defects and diffusion mechanisms in graphite. *Physical Review Letters* **61**, 2693-2696.
- Martin, M. G. (2013) MCCCS Towhee: a tool for Monte Carlo molecular simulation. *Molecular Simulation* **39**, 1184-1194.
- Martin, M. G. & Siepmann, J. I. (1998) Transferable potentials for phase equilibria. 1. United-atom description of n-alkanes. *Journal of Physical Chemistry B* **102**, 2569-2577.
- McDonald, I. R. (2002) NpT-ensemble Monte Carlo calculations for binary liquid mixtures (Reprinted from Molecular Physics, vol 23, pg 41-58, 1972). *Molecular Physics* **100**, 95-105.
- NIST. http://webbook.nist.gov/chemistry/fluid/ (2011).
- Norman, G. E. & Filinov, V. S. (1969) Investigations of Phase Transitions by a Monte-Carlo Method. *High Temperature* 7, 216-&.
- Shao, Y. *et al.* (2010) Nitrogen-doped graphene and its electrochemical applications. *Journal of Materials Chemistry* **20**, 7491-7496.
- Shayeganfar, F. & Neek-Amal, M. (2012) Methane molecule over the defected and rippled graphene sheet. *Solid State Communications* **152**, 1493-1496.
- Steele., W. (1973) The physical interaction of gases with crystalline solids. *Surface Science* **36**, 317–352.
- Tissot, B.P. & Welte, D.H. (1984) Petroleum Formation and Occurrence (Springer-Verlag, 1984).
- Wang Yin, Feng Yamin, Meng Gaoxiang, Dong Xiaopeng & ., H. X. (2015) Methane adsorption on intrinsic, vacancy and N-doped graphene: A first-principles study. *Physica Status Solidi* **252(B)**, 1757-1766.

# 5. EXPERIMENTAL DETERMINATION OF P-V-T-X PROPERTIES AND ADSORPTION KINETICS IN THE CO2-CH4 SYSTEM UNDER SHALE GAS RESERVOIR CONDITIONS

#### 5.1. Introduction

Shale gas production via hydrofracturing has profoundly changed the energy portfolio in USA and other parts of the world. Under the shale gas reservior conditions,  $CO_2$  and  $H_2O$ , either in situ or being injected during hydrofracturing or both, co-exist with  $CH_4$ . One important feature characteristic with shale gas is the presence of nanometer-scale (1-100 nm) pores in shale or mudstone. The interactions among  $CH_4$ ,  $CO_2$  and  $H_2O$  in those nano-sized pores directly impact shale gas storage and gas release from shale matrix. Therefore, a fundamental understanding of interactions among  $CH_4$ ,  $CO_2$  and  $H_2O$  in nanopore confinement would provide guidance in addressing a number of problems such as rapid decline in production after a few years and low recovery rates. We have systematically investigated the P-V-T-X properties and adsorption kinetics in the  $CH_4$ - $CO_2$ - $H_2O$  system under the reservoir conditions.

We have designed and constructed a unique high temperature and pressure experimental system that can measure both of the P-V-T-X properties and adsorption kinetics sequentially. We measure the P-V-T-X properties of CH<sub>4</sub>-CO<sub>2</sub> mixtures with CH<sub>4</sub> up to 95 vol. %, and adsorption kinetics of various materials, under the conditions relevant to shale gas reservoirs. We use three types of materials: (I) model materials, (II) single solid phases separated from shale samples, and (III) crushed shale samples from both of the known shale gas producing formations. The model materials are well characterized in terms of pore sizes. Therefore, the results from the model materials help to mechanistically understand the effects of mineral structures and nanopore confinement on gas sorption and desorption in shale samples.

The P-V-T-X properties obtained in this study is used to establish a high precision equation of state (EOS) applicable to shale gas recovery in confined nano-pore environments. An equation of state (EOS) that can accurately describe interactions in the CH<sub>4</sub>–CO<sub>2</sub>–H<sub>2</sub>O system for a wide range of ionic strengths in a confined environment is an important and essential tool that enables efficient resource recovery from fewer, and less environmentally impactful wells. However, such an EOS does not exist at present. For the bulk properties, Duan et al. (1992) proposed an EOS for the CH<sub>4</sub>–CO<sub>2</sub>–H<sub>2</sub>O system. Their EOS was based almost solely on experimental data for the following binary systems, i.e., CH<sub>4</sub>–H<sub>2</sub>O, CO<sub>2</sub>–H<sub>2</sub>O, and CH<sub>4</sub>–CO<sub>2</sub>. As they pointed out, "ternary data are almost nonexistent." In their parameterization, there were two experimental investigations addressing the ternary system as described in the following. Price (1981) measured solubility of CH<sub>4</sub> and CO<sub>2</sub> in brine containing 5 wt% NaCl at 150°C and 345 bars. Ramboz et al. (1985) investigated the CH<sub>4</sub>–CO<sub>2</sub>–H<sub>2</sub>O system at temperatures above 370°C, which is not applicable to the conditions for shale gas recovery. After the publication of Duan et al. (1992), a number of studies on the CH<sub>4</sub>–CO<sub>2</sub>–H<sub>2</sub>O system at temperatures below room temperature were initiated. The aim of these studies was to determine the hydrate equilibrium (e.g., Bruusgaard et al., 2010), but again these studies are not relevant to the conditions applicable for shale gas recovery.

Sorption capacities, sorption and desorption kinetics are highly relevant to shale gas recovery. We systematically measure sorption capacities, sorption and desorption kinetics for the aforementioned three types of materials under reservoir relevant conditions. These results can be used for molecular dynamics (MD) modeling of the interactions in a multiple component system.

#### 5.2 Methods

Two sets of gas sorption-desorption experiments were conducted: (1) low pressure experiments and high pressure and high temperature experiments. The low pressure sorption measurements were performed using a thermal gravimetric analyzer (TGA). The TGA analysis was conducted using a Netzsch STA 409 thermal gravimetric analyzer with differential scanning calorimeter (DSC) and Differential temperature analyzer (DTA) that is adapted for measurements of adsorption capacities and kinetics of the three types of materials at reservoir relevant temperatures up to 125°C and constant pressures up to 1 bar. We studied the adsorption kinetics by monitoring the evolution of the weight change as a function of time after a mixture of CO<sub>2</sub> and CH<sub>4</sub> was introduced into the sorption vessel and until sorption saturation equilibrium was reached.



**Figure 5-1.** High-temperature-high pressure system for measuring gas sorption-desorption under reservoir-relevant conditions.

We also measured  $CH_4$ - $CO_2$  sorption capacities and kinetics for the materials at high temperatures and pressures using the instrumentation designed at SNL (Figure 5-1). The system developed at SNL uses digital transducers for data acquisition. Therefore, the digital transducers are calibrated with the high precision Heise gauge (see Figures 5-2 and 5-3). The calibration is currently up to  $\sim$ 1,300 psi. It can be adapted to higher pressures as the experiments are extended to higher pressures.

The general relation between the moles of gas sorbed and the pressure difference owing to sorption can be expressed as:

$$Z = \frac{(\Delta P) \times V}{n_{sorbed} \times R \times T} \tag{5-1}$$

where Z is the compressibility factor, V the volume of the experimental system,  $\Delta P$  the difference between the initial pressure and the final pressure, T the experimental temperature, R ideal gas constant, and  $n_{sorbed}$  the moles of CH<sub>4</sub>-CO<sub>2</sub> mixtures sorbed onto the adsorbent. In our experimental system, V and T are constant. Hence, Z is only a function of pressure. Rearranging Equation (5-1), we have:

$$n_{sorbed} = \frac{(\Delta P) \times V}{Z \times R \times T} \tag{5-2}$$

Therefore, as long as Z at the pressure of  $\Delta P$  is known,  $n_{sorbed}$  can be solved using Equation (5-2).

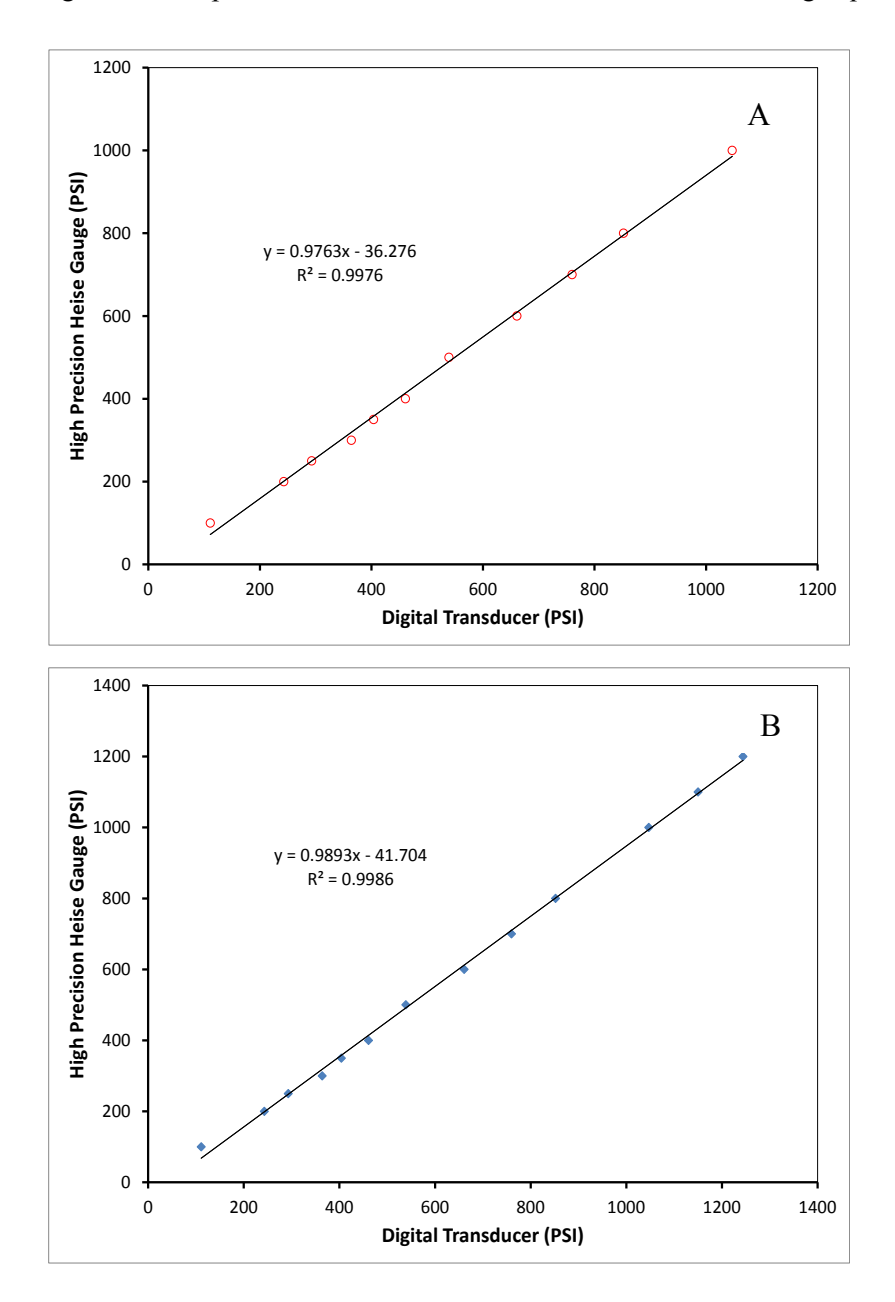


**Figure 5-2.** Calibration of the digital transducers for the measurement of sorption capacities and kinetics under high-temperature and high pressure conditions. (A) Reference cell; (B) sample cell.

McElroy et al. (1989) measured the compressibility factors for CH<sub>4</sub>-CO<sub>2</sub> mixtures at CH<sub>4</sub> percentages of 0, 25, 75 and 100 in the temperature range from 30°C to 60°C. We used their measured compressibility factors at 50°C and at pressures ranging from 120 bars to 8 bars to develop the correlations between

pressures and compressibility factors. Then, the compressibility factor at  $\Delta P$  is computed based on the correlation. Using Equation (5-2), the amounts absorbed are calculated, and the sorption kinetics are also calculated based on the time required for reaching the sorption saturation.

Alternatively, the following algorism can also be used for computing the amounts of CH<sub>4</sub>-CO<sub>2</sub> mixtures sorbed:

$$Z_{initial} = \frac{P_{initial} \times V}{n_{total,initial} \times R \times T}$$
 (5-3)

$$Z_{final} = \frac{P_{final} \times V}{n_{total, final} \times R \times T}$$
 (5-4)

$$n_{sorbed} = n_{total,initial} - n_{total,final}$$
 (5-5)

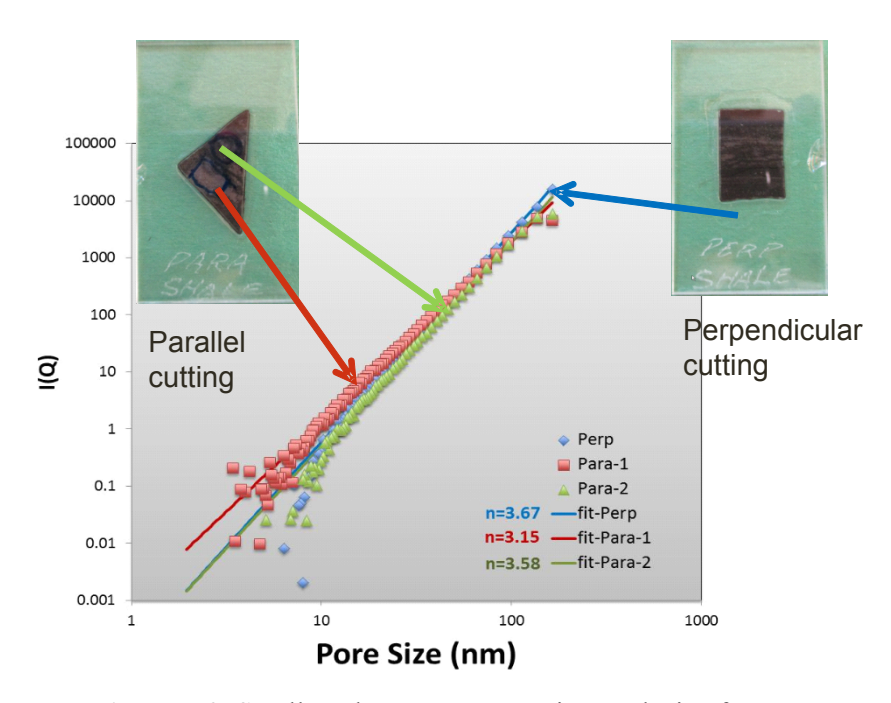
Notice that the amounts of  $CH_4$ - $CO_2$  mixtures sorbed onto the materials are calculated based on the algorism outlined in Equations (5-1) and (5-2).



Figure 5-1. Kerogen isolated from Mancos shale

#### 5.3 Results

**Material Characterization:** We have obtained about 10 shale core samples through purchasing or from the collaboration with Texas A&M University (TAMU) including samples from Mancos, Woodford, and Marcellus formations. We have isolated three kerogen materials from Mancos, Woodford, and Marcellus shale samples (Figure 5-1). The BET surface area of the kerogen isolated from Mancos shale was determined to be ~ 2 m²/g. Mancos shale sample was studied using a neutron scattering technique. The result shows a relatively low organic carbon content in this shale. The pore size of the shale is dominated by 1-100 nm (Figure 5-2). The analysis shows the anisotropic nature of a shale sample related to sample orientations (parallel vs perpendicular to the bedding). We also performed the Fourier Transform Infrared Spectroscopy (FTIR) analysis of three kerogens isolated. The FTIR data show distinct characteristics for three different maturity kerogens (Figure 5-3). The data indicate a distinct FTIR feature around 1600 cm<sup>-1</sup> for the maturity of kerogen.



**Figure 5-2.** Small angle neutron scattering analysis of Mancos shale

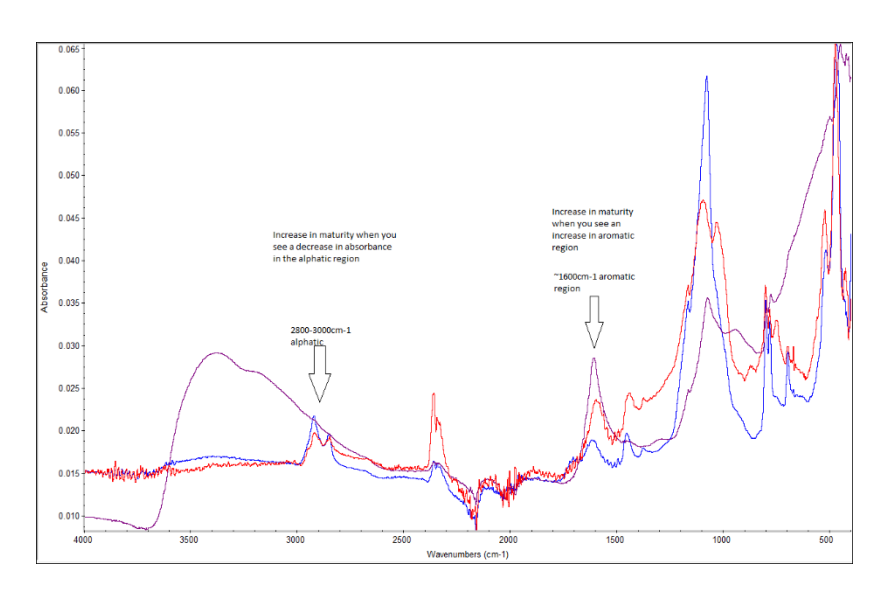
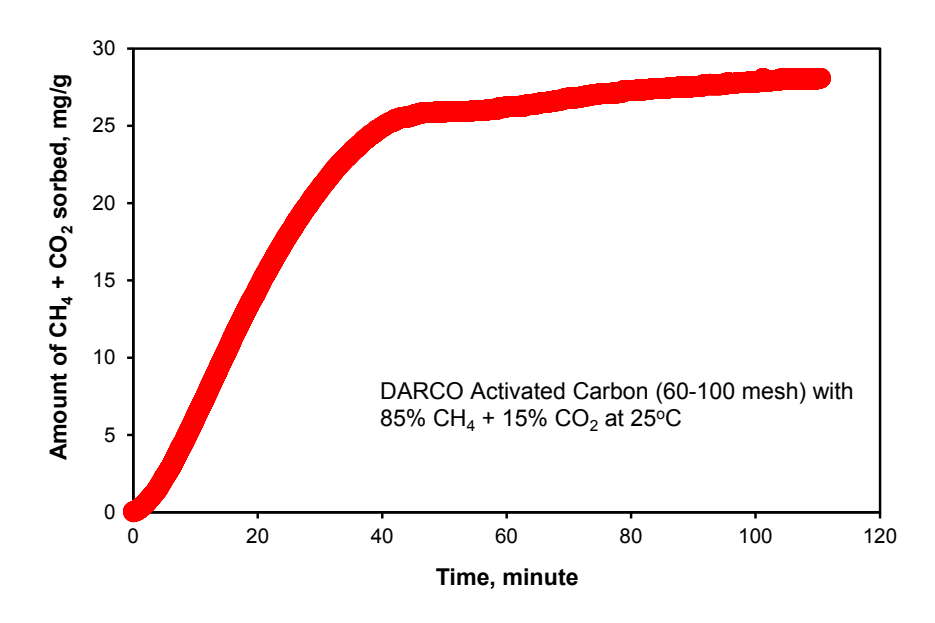
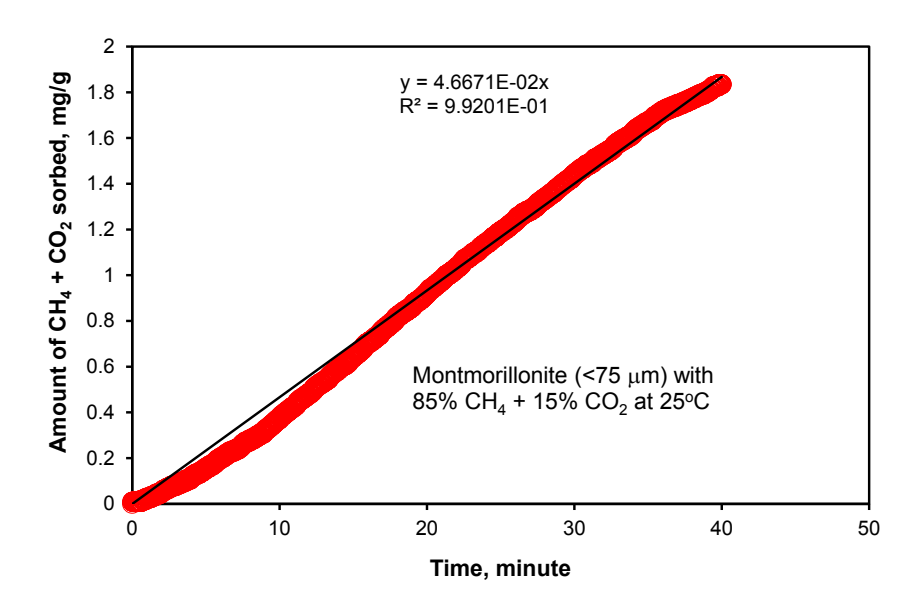


Figure 5-3. FTIR spectra of kerogens isolated from Mancos, Woodford and Marcellus shales.

**Sorption measurements:** A typical sorption curve using TGA is presented in Figure 5-4. The linear portion of the curve is used for determination of sorption kinetics. The portion that indicates the attainment of sorption saturation is used for the determination of sorption capacities. As an example, the sorption rate for montmorillonite is determined from the linear portion of the sorption curve as shown in Figure 5-5. We have used this methodology to measure the sorption capacities and kinetics for activated carbon, crushed shale, mesoporous silica, illite and montmorillonite. We have obtained raw data for these model substances up to 125°C. The sorption capacities and sorption rates that have been processed so far are listed in Table 5-1.



**Figure 5-4.** TGA measurement of CH<sub>4</sub>-CO<sub>2</sub> sorption on activated carbon at 25°C temperature and 1 bar.



**Figure 5-4.** Determination of sorption kinetics with CH<sub>4</sub>-CO<sub>2</sub> for montmorillonite at 25°C temperature and 1 bar.

As shown in Table 5-1, activated carbon (as an analog to kerogen) has a high sorption capacity for CH<sub>4</sub> and CO<sub>2</sub>. Interestingly, our data show that a significant fraction of CH<sub>4</sub> and CO<sub>2</sub> can be adsorbed onto montmorillonite. Although the sorption capacity of montmorillonite is much less than that for activated carbon, our data indicate that methane adsorbed on clay minerals could contribute a significant portion of gas-in-place in an unconventional reservoir, considering that clay minerals constitute a major part of a shale gas reservoir.

**Table 5-1.** Experimental measurements of sorption capacities and sorption rates for the model substances at 1 bar total pressure

| Model Substances | Temp, °C | Gas Mixture, volume                       | Pressure, | Sorption  | Sorption Rate,         |
|------------------|----------|---|-----------|-----------|------------------------|
|                  |          | percent                                   | bar       | Capacity, | mg/g min <sup>-1</sup> |
|                  |          |   |           | mg/g      |                        |
| DARCO activated  | 25       | 85% CH <sub>4</sub> + 15% CO <sub>2</sub> | 1         | 28        | 0.68                   |
| carbon           | 50       | 85% CH <sub>4</sub> + 15% CO <sub>2</sub> | 1         | 11        | 0.59                   |
|                  | 75       | 85% CH <sub>4</sub> + 15% CO <sub>2</sub> | 1         | 9.0       | 0.31                   |
|                  | 100      | 85% CH <sub>4</sub> + 15% CO <sub>2</sub> | 1         | 2.1       | 0.14                   |
|                  | 125      | 85% CH <sub>4</sub> + 15% CO <sub>2</sub> | 1         | 1.8       | 0.10                   |
|                  | 25       | 85% CH <sub>4</sub> + 15% CO <sub>2</sub> | 1         | 2.8       | $4.7 \times 10^{-2}$   |
|                  | 50       | 85% CH <sub>4</sub> + 15% CO <sub>2</sub> | 1         | 0.30      | $9.6 \times 10^{-3}$   |
| Montmorillonite, | 75       | 85% CH <sub>4</sub> + 15% CO <sub>2</sub> | 1         | 0.19      | $6.7 \times 10^{-3}$   |
| <75 μm           | 100      | 85% CH <sub>4</sub> + 15% CO <sub>2</sub> | 1         | 0.18      | $5.1 \times 10^{-3}$   |
|                  | 125      | 85% CH <sub>4</sub> + 15% CO <sub>2</sub> | 1         | 0.12      | $3.3 \times 10^{-3}$   |
|                  | 25       | 85% CH <sub>4</sub> + 15% CO <sub>2</sub> | 1         | 0.29      | $3.3 \times 10^{-3}$   |
| Crushed Shale    | 50       | 85% CH <sub>4</sub> + 15% CO <sub>2</sub> | 1         | 0.21      | $2.7 \times 10^{-3}$   |
|                  | 75       | 85% CH <sub>4</sub> + 15% CO <sub>2</sub> | 1         | 0.16      | $1.7 \times 10^{-3}$   |

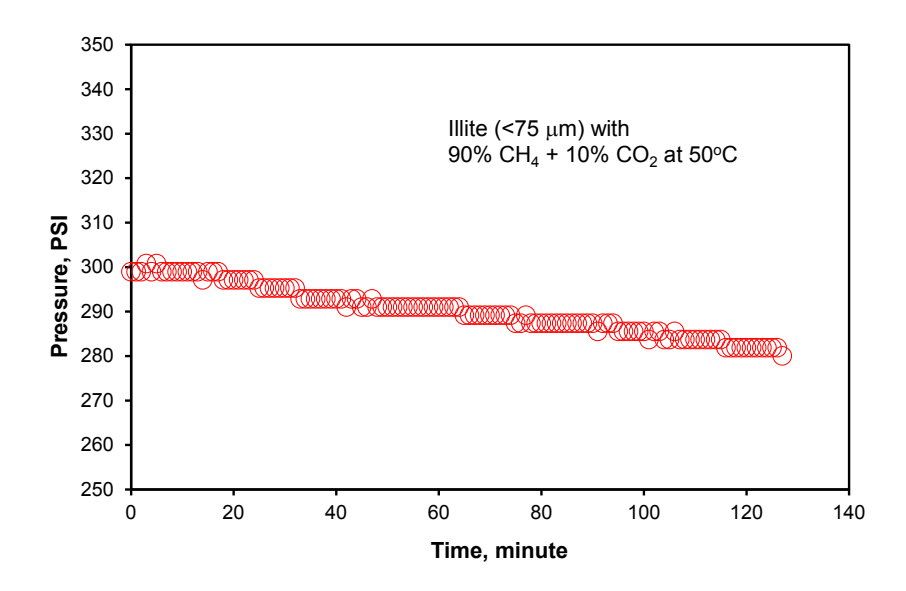


Figure 5-6. Sorption measurements of CH<sub>4</sub>-CO<sub>2</sub> on illite at 50°C temperature and 300 psi.

A typical sorption curve at high temperatures and pressures using the instrumentation designed at SNL is presented in Figure 5-6. Notice that after the initial introduction of CH<sub>4</sub>-CO<sub>2</sub> into the system, the pressure continuously decreased until the sorption saturation was reached. Therefore, the decrease in pressure is interpreted as adsorption to the adsorbing material. Consequently, the amounts of CH<sub>4</sub>-CO<sub>2</sub> absorbed onto the model substance can be computed based on the pressure difference. We have obtained raw data for the model substances up to 125°C and at the total pressures of 1000 psi by using this method (Table 5-2).

**Table 5-2.** Experimental measurements of sorption capacities and sorption rates for a model material at elevated temperatures and pressures

| Model Substances | Temp, °C | Gas Mixture, volume                       | Pressure, | Sorption  | Sorption Rate,         |
|------------------|----------|---|-----------|-----------|------------------------|
|                  |          | percent                                   | PSI       | Capacity  | mg/g min <sup>-1</sup> |
|                  |          |   |           | (mixture) |                        |
|                  |          |   |           | mg/g      |                        |
| Illite, <75 μm   | 50       | 90% CH <sub>4</sub> + 10% CO <sub>2</sub> | 300       | 190       | 1.5                    |

We have also studied the potential impact of the interaction of shale with hydrofracking fluid on gas sorption. Parallel GTA sorption were performed on both reacted and unreacted Mancos shale samples. The reacted sample was obtained by reacting a powdered shale sample with a synthetic hydrofracturing fluid over one month at 90 °C in a reaction Parr vessel. The composition of the synthetic hydrofracturing fluid is: 0.1% polyacrylamide; 0.05% sodium polyacrylate; 0.1% sodium chloride; 0.02% methanol; 0.01% hydrochloric acid; 0.007% tetrakis (hydromethyl) phosphonium sulfate. It is interesting to find that the  $CH_4$ - $CO_2$  sorption capacity for the reacted sample is systematically lower (by a factor of ~2) than that for the unreacted (raw) sample (Figure 5-7). Since there is no significant change in the BET surface area between the reacted and the unreacted samples (Table 5-3), it is postulated that the observed difference in

sorption capacity may result from a mineralogical or surface chemistry change of the shale sample induced by fluid-rock interaction.

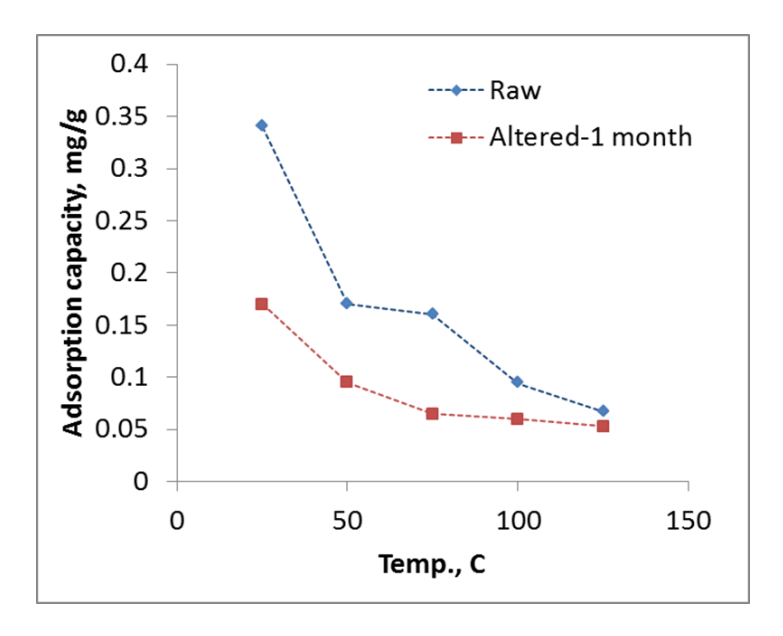


**Figure 5-7.** CH4-CO2 sorption on Mancos shale samples unreacted or reacted with a synthetic fracking fluid.

**Table 5-3.** BET surface area measurements of shale samples

| Sample ID                    | BET surface area (m <sup>2</sup> /g) |
|------------------------------|--------------------------------------|
| Unreacted Mancos shale       | 8.9                                  |
| Mancos shale reacted with    | 10.5                                 |
| fracking fluid for one month |                                      |
| Mancos shale reacted with    | 10.5                                 |
| fracking fluid for two month |                                      |

#### 5.4. Conclusion

We have successfully established experimental capabilities for measuring gas sorption and desorption on shale and model materials under a wide range of physical and chemical conditions including reservoir-relevant high temperature and high pressure conditions. Both low and high pressure measurements show that a significant fraction of CH<sub>4</sub> and CO<sub>2</sub> can be adsorbed onto montmorillonite. Although the sorption capacity of montmorillonite is much less than that for activated carbon, our data indicate that methane adsorbed on clay minerals could contribute a significant portion of gas-in-place in an unconventional reservoir, considering that clay minerals constitute a major part of a shale gas reservoir. We have also studied the potential impact of the interaction of shale with hydrofracking fluid on gas sorption. We have found that the CH<sub>4</sub>-CO<sub>2</sub> sorption capacity for the reacted sample is systematically lower (by a factor of ~2) than that for the unreacted (raw) sample. This difference in sorption capacity may result from a mineralogical or surface chemistry change of the shale sample induced by fluid-rock interaction.

#### 5.4. References

- Bruusgaard, H., Beltrán J.G., Servio, P., 2010. Solubility measurements for the CH<sub>4</sub> + CO<sub>2</sub> + H<sub>2</sub>O system under hydrate–liquid–vapor equilibrium. Fluid Phase Equilibria 296, 106-109.
- Duan, Z.-H., Moller, N., Weare, J.H., 1992. An equation of state for the CO<sub>2</sub>—CH<sub>4</sub>—H<sub>2</sub>O system: II. Mixtures from 50 to 1000°C and 0 to 1000 bar. Geochimica et Cosmochimica Acta 56, 26 19-2631.
- McElroy, P.J., Battino, R., and Dowd, M.K., 1989. Compression-factor measurements on methane, carbon dioxide, and (methane + carbon dioxide) using a weighing method. Journal of Chemical Thermodynamics, 21:1287-1300.
- Price, L. C., 1981. Methane solubility in brines with application to the geopressured resource. Proceedings of the 5th Geopressured and Geothermal Energy Conference 5, 205-214.
- Ramboz, C., Schnapperd, D., and Dubessy, J., 1985. The *P-V-T-X- fO*<sub>2</sub> evolution of CO<sub>2</sub>—CH<sub>4</sub>—H<sub>2</sub>O-bearing fluid in a wolframite vein: Reconstruction from fluid inclusion studies. Geochimica et Cosmochimica Acta 49, 205-219.

## 6. SUMMARY

Shale is a natural nanocomposite material with distinct characteristics of nanometer-scale pore sizes, extremely low permeability, high clay contents, significant amounts of organic carbon, and large spatial heterogeneities. Nanopore confinement can substantially modify the physical and chemical properties of a chemical species. Our work has shown that nano-confinement plays an important role in methane disposition and release in unconventional reservoirs. Using molecular simulations, we show that methane release in nanoporous kerogen matrix is characterized by fast release of pressurized free gas (accounting for ~ 30 - 47% recovery) followed by slow release of adsorbed gas as the gas pressure decreases. The first stage is driven by the gas pressure gradient while the second stage is controlled by gas desorption and diffusion. The long-term production decline appears controlled by the second stage of gas release. We further show that diffusion of all methane in nanoporous kerogen behaves differently from the bulk phase, with much smaller diffusion coefficients. The MD simulations also indicate that a significant fraction (3 -35%) of methane deposited in kerogen can potentially become trapped in isolated nanopores and thus not recoverable. We have successfully established experimental capabilities for measuring gas sorption and desorption on shale and model materials under a wide range of physical and chemical conditions. Both low and high pressure measurements show significant sorption of CH<sub>4</sub> and CO<sub>2</sub> onto clays, implying that methane adsorbed on clay minerals could contribute a significant portion of gas-in-place in an unconventional reservoir. We have also studied the potential impact of the interaction of shale with hydrofracking fluid on gas sorption. We have found that the CH<sub>4</sub>-CO<sub>2</sub> sorption capacity for the reacted sample is systematically lower (by a factor of ~2) than that for the unreacted (raw) sample. This difference in sorption capacity may result from a mineralogical or surface chemistry change of the shale sample induced by fluid-rock interaction. Our results shed a new light on mechanistic understanding gas release and production decline in unconventional reservoirs.

## **DISTRIBUTION**

Lawrence Livermore National Laboratory
 Attn: N. Dunipace (1)
 P.O. Box 808, MS L-795

Livermore, CA 94551-0808

1 MS0899 Technical Library 9536 (electronic copy)

1 MS0359 D. Chavez, LDRD Office 1911

For CRADA reports add:

1 MS0115 OFA/NFE Agreements 10012

For Patent Caution reports, add:

MS0161 Legal Technology Transfer Center 11500

